Politecnico di Torino

Danmarks Tekniske Universitet

Design and fabrication of a microfluidic trap for full spectrum impedance scans of single bacteria

Author

Sara Di Paolo s319894

Supervisors

Matteo Cocuzza
Maria Dimaki
Christian Vinther Bertelsen
Winnie Edith Svendsen
Rahul Singh

July 3, 2025

Preface

This thesis was written at DTU Bioengineering department as part of the Erasmus+ Learning Agreement, in fulfillment of the requirements for acquiring the M. Sc. Eng. degree in Nanotechnology for Smart and Integrated Systems. The project was carried out in the facilities of the Technical University of Denmark campus in Kongens Lyngby, initiated in February 2025 and lasted over a period of five months.

The work was executed in NanoBio Integrated Systems (NaBIS) group and in the cleanroom facilities of DTU Nanolab, with supervision from Senior Researcher Maria Dimaki, Postdoc Christian Vinther Bertelsen, PhD student Rahul Singh and Professor Winnie Edith Svendsen.

Part of the work described in this report was done in collaboration with fellow student Sara Pittelli.

Kongens Lyngby, July 3, 2025 Sara Di Paolo (s319894)

Abstract

The study and characterization of bacteria is nowdays drawing increasing interest among the scientific community. With the use of Impedance Flow Cytometry and Electrical Impedance Spectroscopy is possible to perform detailed analysis on shape, size and compositional properties of bacteria.
In the present project, these techniques are intended to be employed in a biosensing device in combination with a customized microfluidic channel, designed with the ambition of trapping single bacteria by exploiting its own geometry.
The trap mechanism is first developed and simulated by the means of the finite element method software COMSOL, highlighting the challenges associated with the single bacterium immobilization.
The fabrication of the device components is performed in the cleanroom facility of DTU Nanolab, where, after undergoing several process optimizations, electrodes sets and a silicon mold for the creation of the microfluidic channel are successfully obtained, with the trap width having an average dimension of ~ 650 nm.
The biosensor is then assembled and tested in an experimental setup at DTU Bioengineering, to inspect the trapping capability and perform electrical impedance spectroscopy characterizations. The former analysis is proven to produce some events, although the quality and repeatability of the results is challenged by the laboratory equipment, while the latter is prevented by difficulties associated to the alignment of the device components, which were overcomed only after the scheduled experimental period.
Although further testing and optimizations are necessary, the device implements promising functionalities and may represent a foundation for the development of an innovative biosensor.

Contents

Chapter 1

Introduction

1.1 Motivations

Bacterial research and classification are gaining increasing popularity in the scientific field. Bacteria are among the earliest known organisms and represent a fundamental presence in our everyday life: they contribute to essential processes such as digestion, fermentation and the preservation the ecosystem functioning [1]. In particular, *Escherichia Coli* (*E.coli*) are widely investigated and represent a model for microbiological research. Among the several *E.coli* strains, many are non-pathogenic and are commonly found in the intestines of humans and warm-blooded animals, where they contribute to maintaining gut health. However, pathogenic strains can cause serious diseases, that may be transmitted through consumption of contaminated foods, such as raw or undercooked meat, or water.[2] For this reason, their identification is a fundamental aspect in ensuring public health. To this purpose, several techniques have been developed and explored in recent years. Among these, Impedance Flow Cytometry (IFC) and Electrical Impedance Spectroscopy (EIS) have been investigated and optimized, drawing growing attention because of their promising advantages, such as cost reduction, the possibility of having a real time analysis and the effectiveness of the results without the use of labeling agents. The implementation of those techniques in Lab-on-a-Chip (LOC) systems can enable a fast and cost effective analysis, allowing for rapid diagnostics even in limited equipment situations.

1.2 Lab on a Chip systems

Lab-on-a-chip devices are miniaturized systems that integrate one or more laboratory functions into a single chip, typically a few millimeters or square centimeters in size. Their goal is to replicate, on a reduced scale, operations that would normally be performed in a traditional laboratory environment, enabling faster analysis and enhancing the portability.

A key concept often associated with Lab-on-a-chip (LOC) systems is microfluidics. Employing microfluidics in LOCs is fundamental because it allows the manipulation of liquids on an extremely small scale, typically in the order of microliters or nanoliters, by exploiting the physical properties that arise from scaling down dimensions. This capability is the foundation of many of the advantages of LOCs, including portability, miniaturization and reduction in reagent volumes, which leads to cost savings, reduced environmental impact, less invasive sample collection and greater control over operating parameters, facilitating the reproducibility of the analyses. [3]

Because of their unique ability to replicate laboratory functions in small and relatively simple devices in terms of components and often materials, these systems are suited for point-of-care applications. This means that they are ideal for emergency situations where immediate and user-friendly diagnostic tools are needed, making them accessible to anyone, even without specialised training.[4]

1.3 Applications of IFC and EIS techniques

Impedance flow cytometry (IFC) and Electrical Impedance spectroscopy (EIS) techniques allow for the possibility of having a fast, non-invasive, cost effective, real time analysis without the use of labeling agents [5]. These advantages make them highly promising characterization methods that can constitute a valid alternative to traditional techniques [6].

The described impedance characterization methods, whice detection principle relies on electric field variations induced by an analyte suspended in a conductive medium and recorded by a set of electrodes, can be applied to cells, various types of bacteria, clusters of particles and beads.

Bacteria and cells are generally constituted of an inner gel-like substance known as cytoplasm, where the nucleus, ribosomes and the other organelles are contained and a membrane, made by a double layer of phospholipids [7]. Cells usually only have a single membrane while gram negative bacteria can present an inner and an outer membrane. [8]. Beads are inorganic and typically constituted by polystyrene, presenting no shell structures. A sketch showing a simplified shell model is provided in Figure1.1.

IFC technique is used to measure the electrical impedance of particles as they flow through a microchannel. By analyzing changes in impedance at specific frequencies, IFC can provide information about particles size, morphology and membrane properties.

Electrical Impedance Spectroscopy (EIS) involves the application of an alternating electrical signal over a range of frequencies to a particle and measure its impedance response. The resulting frequency-dependent data contain information about parameters such as composition and structure.

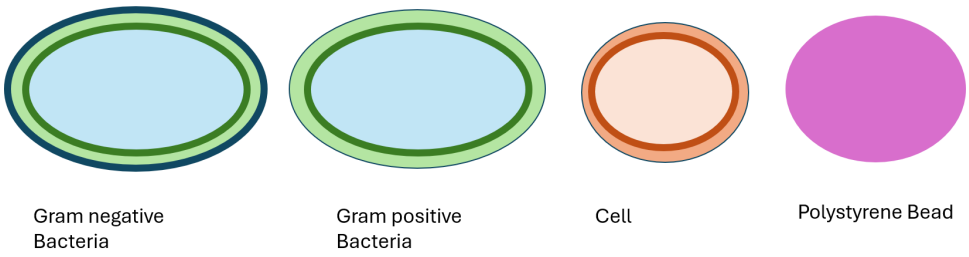

Figure 1.1: Sketch of types of particles commonly analyzed in IFC and EIS. Bacteria can come in different shapes, among which the elliptical is just a simplified one.

Performing together these techniques in microfluidic conditions can allow for an accurate screening of particles properties.

1.4 Device idea

The considerations discussed above, established the basis for the conceptualization of a lab-on-a-chip device designed for the analysis of *E. coli* bacteria. This biosensor integrates the advantages of both Impedance Flow Cytometry, which enables a rapid and high throughput analysis of entire particles population, and Electrical Impedance Spectroscopy, which provides detailed informations at the single-particle level.

In addition, the system features a microfluidic trapping site aimed at immobilizing single bacteria, in order to facilitate EIS characterization, which requires the analyzed particle to be held still while a wide range of frequencies is applied to extract electrical parameters.

The development of this device was divided into two distinct projects: the first, conducted by a fellow master student Sara Pittelli, focused on optimizing the IFC characterization; the second -the present work- is dedicated to the design and fabrication of the microfluidic trap for the improvement of EIS analysis. An overview of the device idea is given in Figure 1.2. The combined use of these techniques has been documented in several cases, including, for example, the trapping and characterization of tumoral cells of type HeLa, A549 and HepG2 [9]. However, this study differs from the applications proposed the current project due to the size of the particles under analysis. Tumoral cells characterized in the article can present diameters of 10-16 µm, whereas for bacterial characterization dimensions are usually in the order of 1µm.

1.5 State of the art

In recent years, Impedance Flow Cytometry and Electrical Impedance Spectroscopy have been employed in a wide range of applications.Also, particle entrapment has been subject of scientific interest, as it can be used for isolation of target particles and enhances detection

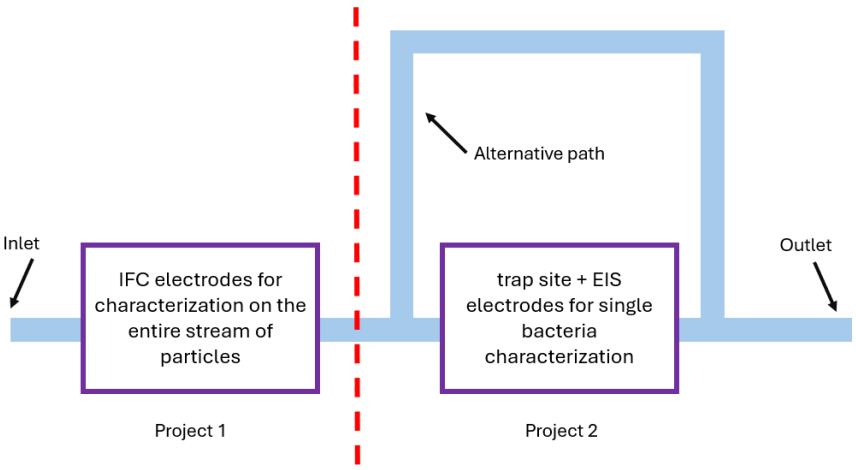

Figure 1.2: Sketch describing the general operation of the device. The different parts are developed separately in two projects and then combined together for the development of the final biosensor

sensitivity in low-concentration samples. Before presenting our work, it is worth to examine how researchers have approached the study of bacteria using these technologies.

Impedance flow cytometry

One of the latest publication that sees the Impedance Flow Cytometry directly applied on bacteria as the main characterization method is the article "*Using Impedance Flow Cytometry for Rapid Viability Classification of Heat-Treated Bacteria.*" by Bertelsen et al. , 2023 [10] where the impedance response of bacterial cells after heat inactivation was investigated. In this work, impedance flow cytometry was used repeating the analysis at two frequencies and extracting the differential argument of the bacteria and medium impedances. In order to conduct analyses, an Impedance flow Cytometer from SBT Instruments A/S was used. This device integrated front facing electrodes and a SU-8 microfluidic channel. The results of this study allowed to classify heat treated bacteria from non-treated ones, understanding that the success of the analysis was strongly influenced by the heat exposure time and conductivity of the medium.

Another recent publication by Spencer et al., "*A fast impedance-based antimicrobial susceptibility test*", 2020 [11] presented an Impedance Flow Cytometry method for Antibiotic Susceptibility Testing (AST). The operative setup was composed of microfluidic chips, where 30 µm wide front facing Platinum multielectrodes were fabricated using photo-lithography. Microfluidic channels 20 µm×40 µm were made by patterning SU8 onto one wafer (Figure 1.3).

IFC measurements were performed on bacteria before and after exposure to antibiotics and by the analysis of changes in the impedance response the effectiveness of the antibiotic could

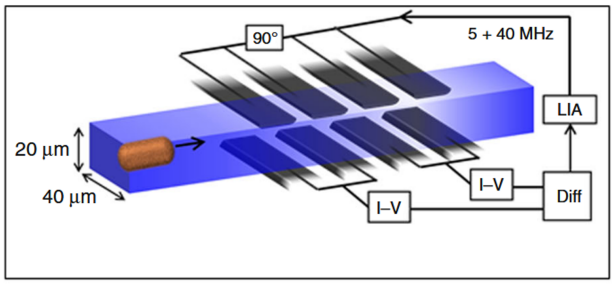

Figure 1.3: IFC set up for antibiotic susceptibility testing presented by Spencer et al.

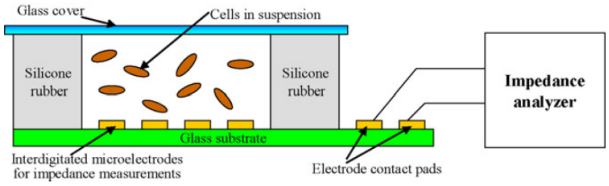

Figure 1.4: EIS setup featuring interdigitated microelectrodes by Liju Yang

be understood. Moreover, results showed compliancy of IFC outcomes with classical methods involving broth microdilution assays.

Full-scan electrical impedance spectroscopy

One interesting application of this technique has been used in "*Electrical impedance spectroscopy for detection of bacterial cells in suspensions using interdigitated microelectrodes*" by Liju Yang, 2007 [12]. EIS is performed to characterize *Salmonella Typhimurium*, a pathogenic bacteria commonly found in humans. The device presented by Yang was composed of an array of 50 interdigitated microelectrodes where a frequency range of 1 Hz to 100 Hz was applied. Results demonstrated that the detection limit of this method is comparable with many label-free immunosensors for detection of pathogenic bacteria reported in literature. The setup is showed in Figure 1.4.

Bacteria traps

Dealing with bacteria can be challenging due to their size. There are several studies concerning the behavior of bacteria immersed in fluids and how they interact with microfluidic structures designed to trap them. Two relevant publications in this regard are those by Kim et al. and Kwon et al. In the first article: *Programmed trapping of individual bacteria using micrometer-size sieves*, 2011 [13], the trapping mechanism relies on multiple hydrodynamic traps featuring a narrow region, smaller than bacteria size, placed along a circular chamber to ensure their entrapment as they flow from the system's inlet to its outlet. In combination with a study on the correct sample concentration the trapping of single bacterium was achieved (Fig 1.5).

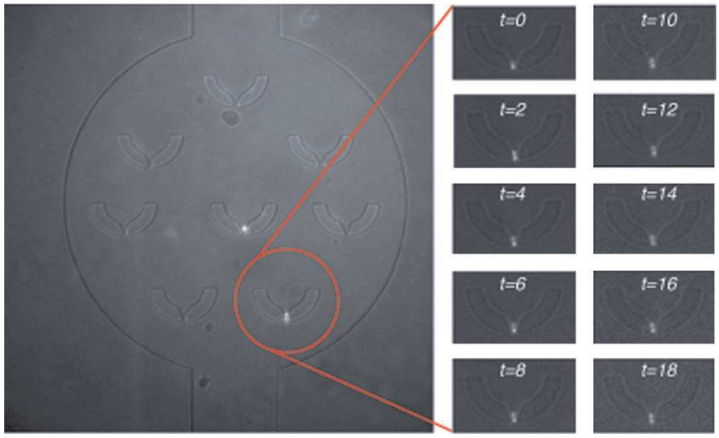

Figure 1.5: Picture of experiment results of single bacteria capture presented by Kim et al.

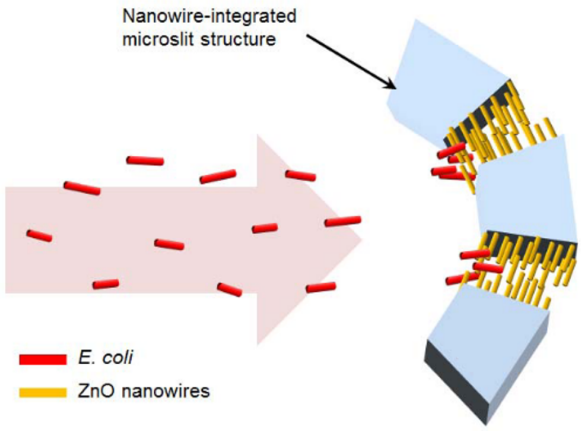

Figure 1.6: Nanowire integrated structure for bacteria trapping developed by Kwon et al.

In the second study, "*A nanowire-integrated microfluidic device for Hydrodynamic trapping and anchoring of bacterial cells*", 2014 [14], trapping is facilitated by the presence of a nanowire array with a fishnet-like structure. Here, ZnO nanowires wire synthesized directly onto the sidewalls of micro-slit structures by hydrothermal method, to form mesh-like cage structures (Figure 1.6). The device was proven to be effective in the trapping and anchoring of *E. Coli*, but showed a certain damage to bacteria and an overall complexity of the technique.

After a thorough investigation of the state of the art, it was interesting to note that a device simultaneously integrating Impedance Flow Cytometry (IFC), Electrical Impedance Spectroscopy (EIS) and a trapping mechanism applied to bacteria is not yet present in current literature. Indeed, several aspects make its construction and the effectiveness of the results challenging, including fabrication techniques and the low signal-to-noise ratio that bacteria inherently produce, due to their size.

1.6 Goal of the project

The main goal of this project is to design and develop a microfluidic trap to allow full spectrum impedance scans of a single bacterium, gaining insights on its functionality and focusing on overcoming the challenges related to its fabrication. In order to obtain this, the project will go through the following steps:

- Ideate a design of a trap that can stop bacteria without obstructing the channel.
- Simulate microfluidic trap behaviour, as a proof of concept and inspect possible outcomes of the full spectrum impedance scan.
- Create, run and optimize cleanroom processes to fabricate device components.
- Build the final device prototype, connecting it to an experimental setup in DTU Bioengineering laboratory and test its functions.

Chapter 2

Theoretical Background

In this chapter, the theoretical aspects useful to have a fundamental understanding of the project will be discussed. First of the IFC and EIS techniques will be presented, to clarify the choice of this method for the project, along with a discussion about the electrical configuration of the system. Then, relevant microfluidics concepts will be explained, to understand the fluid flow properties involved in the device. Finally, several trapping methods will be analyzed in order to highlight the possible options for the implementation of the trap mechanism.

2.1 Electrical impedance characterization methods

2.1.1 Impedance Flow Cytometry

Impedance Flow Cytometry is a technique that can provide cost effective, simple and label free solution for the characterization of micro-organisms. Using impedance measurements, at fixed frequencies, it can be used to understand electrical and structural properties of particles in order to allow for differentiation of biological population [15],[16].

Compared to techniques that require labeling, IFC avoids costs and preparation times of antibodies samples or fluorescent dyes, accounting for the risk of potential alterations of cellular properties and chemical interference commonly caused by markers, leading to a better reliability of the results [17].

2.1.2 IFC Principle of operation

The main aim of this technique is to probe the dielectric properties of particles in real time. In order to function, it requires the presence of a conductive fluid, where the analytes are suspended and electrodes, which can generate an alternating electric field.

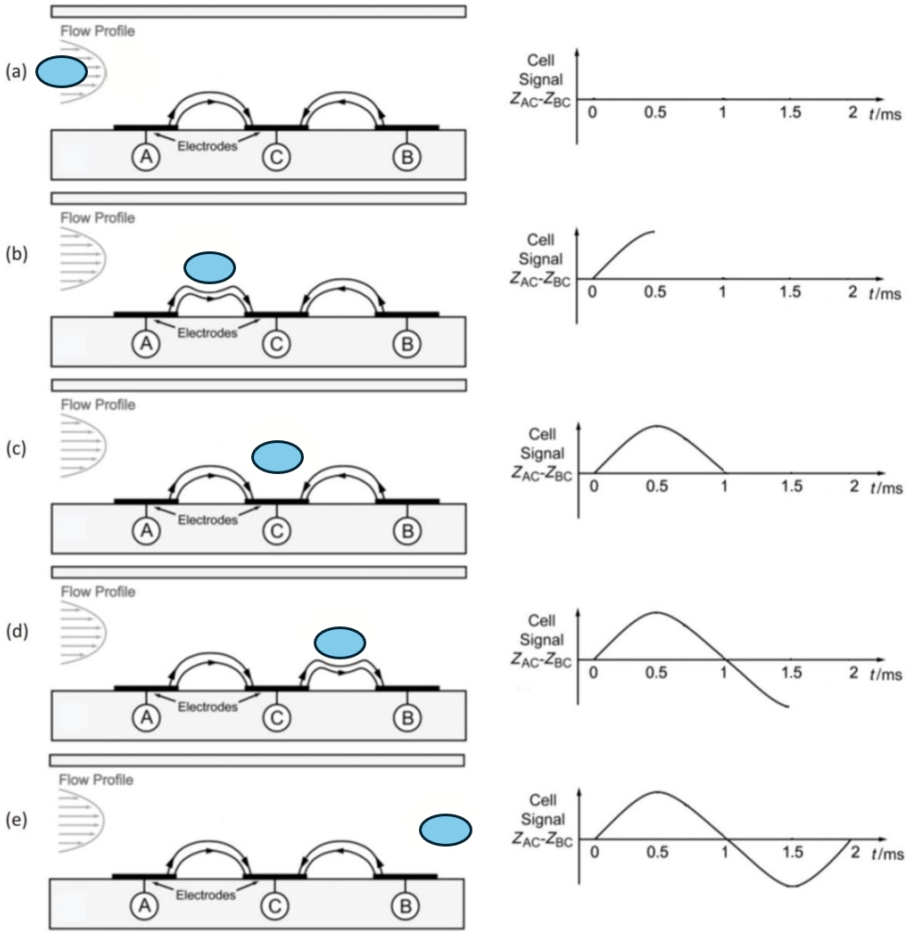

Figure 2.1: Sketch describing the working principle of IFC characterization. The signal is generated by a differential readout of the current measured at the electrodes and converted to impedance.

To describe the steps of the analysis, we start assuming a set of three microelectrodes on top of which an AC voltage is applied (Figure 2.1). In this setup, electrodes A and B are held at 0 V, while electrode C is biased. The readout is given by the differential current signal recorded at electrodes A and B, that is then converted to impedance.

In the initial situation the particle is away from the electrodes where no current is measured, recording zero signal. As the particle moves towards the first electrode, the electric field created in the corresponding region of the microchannel is perturbed, while the other electrodes keep receiving no signal. The differential signal reaches eventually its maximum when the particle approaches the point in the middle of the space between the electrode A and C, registering a peak.

Moving further along the channel, the particle shifts away from the region where the electric field is the strongest, thereby reducing the induced perturbation. As a result, the output

signal will decrease until it reaches the center of the middle electrode, where the influence of the electric field is minimum and the signal is zero again. This behaviour is repeated when the analyte moves toward the next electrode, where the electric field has an opposite polarity, leading to the repetition of the signal with an opposite sign.

The complete signal therefore presents shape of a *double Gaussian* in a zero background signal[18].

The features of the full curve depicting a transition, e.g. peak amplitudes and duration, can be associated to the dielectric properties and size of a certain biological population [19], allowing recognition.

The electrodes setup just discussed describes the general functioning of the IFC analysis, however two possible configuration can be employed, each associated with advantages and disadvantages.

Front facing electrodes

Two electrodes are placed on the top and bottom surfaces of the channel, creating an homogeneous electric field along the height of the channel. The advantage of this set up, is that the change in the electric field produced by particles approaching the electrodes will be the same regardless of the position along the height of the channel. Despite this, front-facing electrodes present the issue of crosstalk due to fringing effects and their fabrication process is relatively complex, as it doubles the production steps and necessitates a precise alignment procedure. [20]

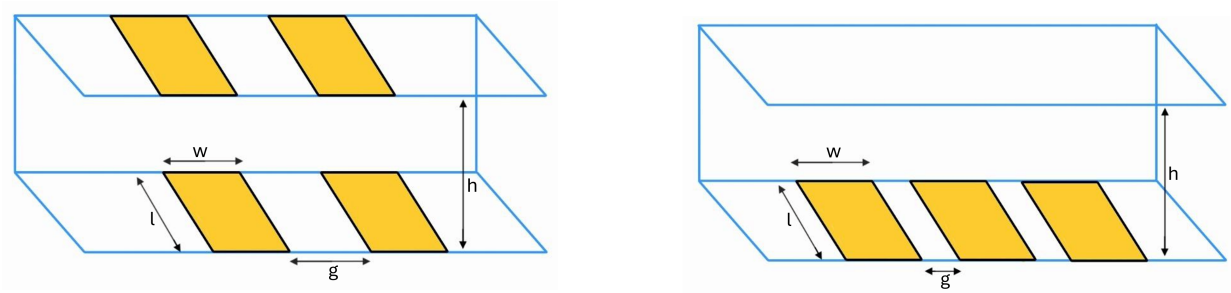

(a) Front facing electrodes (b) Three coplanar electrodes

Figure 2.2: Drawing of front facing and coplanar electrodes setup. l represents the electrodes length, w the width, g the gap in between and h the height. It is also possible to create an asymmetry in the signal by tuning the width and the gap

Coplanar electrodes

In this set up the electrodes lie on the same surface. Depending on the specific type of analysis, it is possible to place a variable number of coplanar electrodes, which will consequently

change the number of peaks recorded.

As opposed to the front facing electrodes, the electric field is stronger closer to the surface of the channel where the electrodes are placed and gradually weaker along the height, which means that the position is a relevant parameter to the analysis, because a particle that travels close to the electrodes will have a stronger signal than one that is far from them. This makes more difficult the interpretation of the results, since a stronger perturbation of the electric field could be given by the particle property or by its proximity to the electrodes [21].

The advantage of having coplanar electrodes consist in the reduced cross talk and in the simpler fabrication process, which is the main reason why in this project the Impedance Flow citometry and the Electrical Impedance Spectroscopy will be carried on using coplanar electrodes.

2.1.3 Electrical impedance spectroscopy

Electrical Impedance spectroscopy (EIS) technique is a topic of large interest in literature. This analysis can be associated to an impedance flow cytometry system and, while keeping the same operational elements, e.g. the microfluidic channel and the electrodes, it allows to further investigate on single particle electronic characteristics by sweeping the frequency used for characterization on a wide range. This constitutes one of the main difference with IFC cytometry.

It is possible, in principle, to perform IFC analysis at more than one frequency, however, the same experiment must be repeated multiple times to obtain differential signals, as particles need to flow through the electrodes for each measurement. This either requires repositioning the particles at the channel's inlet or introducing a new analyte solution for each frequency change. In the latter case, although the biological population can be kept the same, the analysis may lack accuracy due to differences among individual particles.

On the contrary, during EIS the particle remains stationary between the electrodes, ensuring a thorough and specific characterization of the individual particle.

2.1.4 EIS Characterization principle

To perform impedance spectroscopy, the electronic setup is typically composed of two electrodes, as shown in Figure 2.3.
Similarly to IFC, an external potential difference is applied between the two electrodes. Under the influence of the electric field the current travels through a complete circuit, which includes the conductive fluid and the particle under analysis. As explained previously, the signal is maximum when the particle is placed in the center of the gap between the electrodes: since the particle remains stationary, its precise position becomes even more critical to the analysis.

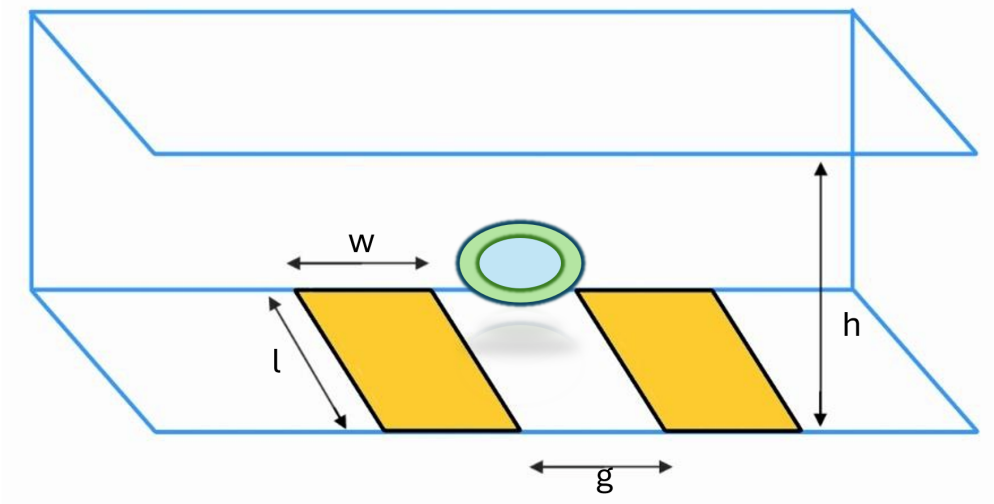

Figure 2.3: Drawing of coplanar electrodes setup for an Electrical Impedance Spectroscopy characterization

2.1.5 Particles electric properties

As introduced in the previous chapter, biological microorganisms are typically composed of an internal cytoplasmic matrix surrounded by an external membrane. From an electrical perspective, the cytoplasm is conductive, whereas the membrane is highly insulating. Consequently, the behavior of these microorganisms in an electric field is influenced by the frequency of the applied signal.

At low frequencies, the insulating membrane prevents the electric field from penetrating the particle, causing the field lines to bypass it. [22] (Figure 2.4). This means that a low frequency signal can carry information about the shape and size of the particle. On the other hand, when the electric field is generated by a high-frequency signal, the field lines can enter the insulating membrane and interact with the conductive cytoplasm within the microorganism. This implies that a high frequency signal can give information about the intracellular biomass of the particle [23]. Combining the impedance information gained at low and high frequency allows differentiation analysis of biological particles.

Regarding beads, the biological membrane is absent, however they exhibit insulating behaviour, enabling the induction of a measurable impedance signal when crossed by an electric field. This characteristic makes them highly suitable for use in calibration and testing procedures of systems based on impedance flow cytometry.

2.1.6 Electrical description of the system

Building upon the considerations discussed, it can be inferred that biological particles are composed of a conductive inner region and an insulating outer layer. These characteristics are described by specific values of permittivity ϵ and conductivity σ.

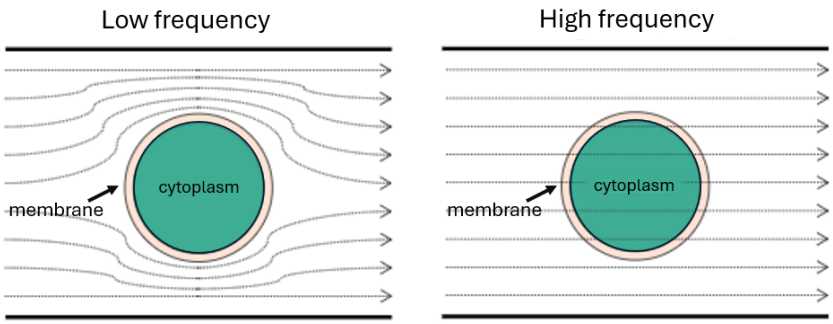

Figure 2.4: Electric field behaviour interacting with a biological particle at different frequencies

It is furthermore important to recall that these particles are travelling in a medium that also possesses a defined conductivity. In order to create a model that will allow to gain electrical information from the system, it is necessary to rely on three concepts: the Maxwell Mixture theory, the formation of an electrical double layer and the presence of parasitic capacitances.

Maxwell Mixture Theory

The Maxwell Mixture Theory aims to explain the dielectric properties of particles suspended in a medium. In particular it affirms that the *equivalent complex permittivity* ϵ_{mix} of a mixture, that includes the particle and the suspending medium is given by:

$$\tilde{\epsilon}_{mix} = \tilde{\epsilon}_m \frac{1 + 2\Phi\tilde{f}_{CM}}{1 - \Phi\tilde{f}_{CM}} \tag{2.1}$$

where $\tilde{\epsilon}_m$ is the complex permittivity of the medium, Φ is the fraction volume, namely the ratio of the particle volume to the detection volume, and $\tilde{f}_{CM}$ the complex Clausis-Mossotti factor, given by:

$$\tilde{f}_{CM} = \frac{\tilde{\epsilon}_p - \tilde{\epsilon}_m}{\tilde{\epsilon}_p + 2\tilde{\epsilon}_m} \tag{2.2}$$

$\tilde{\epsilon}_p$ being the complex permittivity of the particle [24]. To better describe the application of our interest, this equation can be further applied to particles with a shell, introducing an *effective particle permittivity*, explicited in the following equation:

$$\tilde{\epsilon}_{p,eff} = \tilde{\epsilon}_{mem} \frac{(\frac{R}{R-d_0})^3 + 2(\frac{\epsilon_i - \epsilon_{mem}}{\epsilon_i + 2\epsilon_{mem}})}{(\frac{R}{R-d_0})^3 - (\frac{\epsilon_i - \epsilon_{mem}}{\epsilon_i + 2\epsilon_{mem}})} \tag{2.3}$$

with $\tilde{\epsilon}_{mem}$ and d_0 representing respectively the complex permittivity and the thickness of the shell, followed by ϵ_i and R describing the complex permittivity associated to the internal material and the radius of the particle.[25]

Summarizing, it possible to associate to the mixture a complex capacitance and a complex impedance response, described as:

$$\tilde{C}_{mix} = \epsilon_0 \tilde{\epsilon}_{mix} \frac{A}{d} \tag{2.4}$$

$$\tilde{Z}_{mix} = \frac{1}{j\omega \tilde{C}_{mix}} \tag{2.5}$$

Electrical double layer

When a voltage is applied across electrodes immersed in an electrolyte, oppositely charged ions from the electrolyte gather at the boundary of the electrodes' surfaces, forming what is known as *electrical double layer* [26].

The consequent effect is that a linear potential drop will be confined within this region, which is known as Outer Helmoltz Plane (OHP): this phenomenon represent the fundamental principle of working of a parallel plate capacitor.

Next to the OHP lies the *diffused layer* (Stern model), where ions show a certain amount of mobility. In this region, the prevalence of a specific ion population is still noticeable: the electrostatic effects are present, but mitigated by the brownian motion.
The characteristic thickness of this interaction area is referred to as the Debye length, which decreases with increasing electrolyte concentration and increases with the temperature of the solution [27]. A sketch depicting the discussed elements is shown in Figure 2.5. In addition to that, this layer impedes the formation of the electric field inside the channel, thereby it can be modelled as a capacitance in series with a resistance [28].

Parasitic capacitance

Parasitic capacitance, also referred to as stray capacitance, commonly appears to be present in electrical systems with probes and/or wires. It is a generally unwanted phenomenon, generated when two electrical conductors at different voltages are placed in proximity to each other. The electric field established between the two surfaces induces the storage of electric charge, thus creating a capacitance.[29]

2.1.7 Equivalent circuit model

As evidenced by the previously presented electronic analysis of the system components, some of the elements can be represented using electrical equivalents. The assumption that the complex permittivity and conductivity of a physical system can be replaced by equivalent electrical components forms the foundation of the Equivalent Circuit Model (ECM).
This model purpose is to describe every component of the system in terms of capacitances and resistances. The use the ECM is crucial, becuase t leads to the same results obtainable by the Maxwell Mixture theory in a more practical and less complex way [24]. The overall

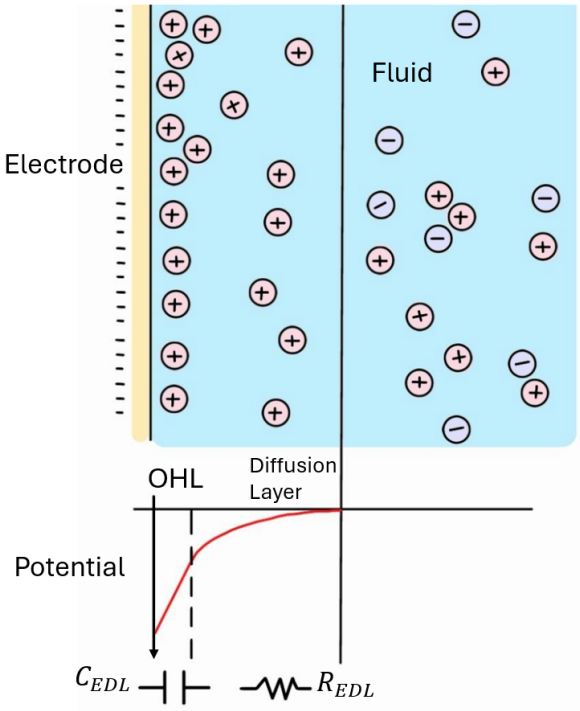

Figure 2.5: Representation of the formation of the Electrical Double layer. The two opposite charged regions give rise to a capacitive behaviour, while the diffusion layer act as a resistance

circuit is presented in figure 2.6.

2.1.8 Frequency range

In the equivalent circuit, multiple elements can give an impedance response: the medium, the parasitic effects, the electrical double layer and the particle under analysis, that can be organic e.g. a bacteria, or inorganic e.g. a bead. For this reason, frequency plays a fundamental role for the impedance characterization, and a meaningful range must be chosen.

To emphasise the presence of the analyte, the frequency range must be selected such that all contributions to the overall impedance, other than that of the medium through which the particles travel, are negligible. The circuital equivalents of the parasitic effects and the EDL are given by:

$$\tilde{Z}_{par} = \frac{1}{j\omega C_{par}} \tag{2.6}$$

$$\tilde{Z}_{EDL} = R_{EDL} + \frac{1}{j\omega C_{EDL}} \tag{2.7}$$

At low frequencies the prevailing contribute is given by the double layer impedance, which

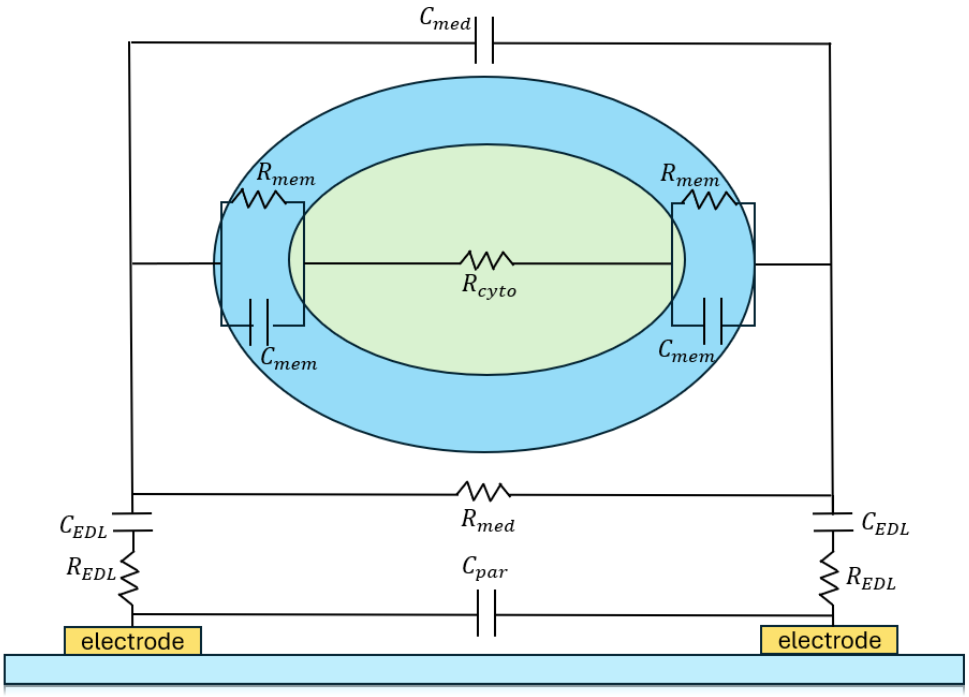

Figure 2.6: Schematization of the ECM comprehending the electrical equivalents of all the elements present in the system: the electrical double layer, the parasitic capacitance, the medium and the particle.

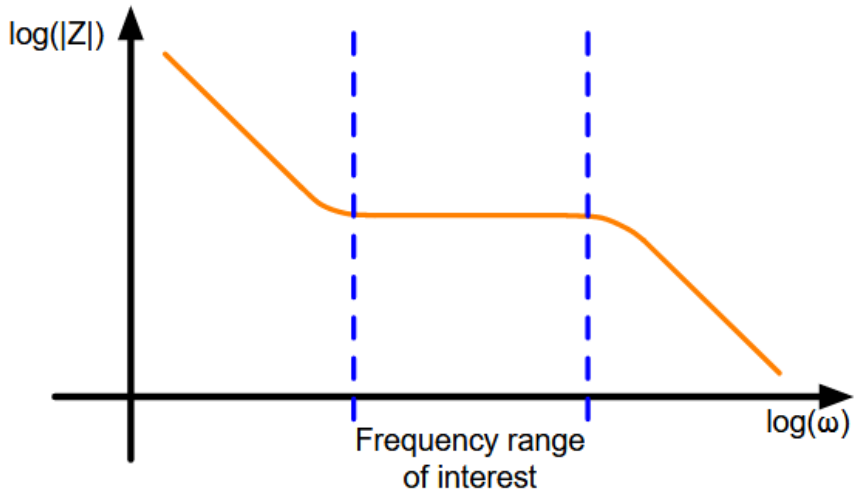

Figure 2.7: Behaviour of the impedance modulus of the whole system as a function of the angular frequency ω, defined as $\omega = 2\pi f$. This picture is taken from [30].

reaches high values and prevents the liquid from receiving current.

At very high frequencies, the parasitic impedance becomes the dominant factor. Due to its very low value, the signal can bypass the fluid under analysis and be dispersed into electrical connection, thus hindering accurate characterization.

With intermediate values of frequencies, the impedance of the system is only influenced by the resistance contribute of the medium, which is also frequency independent. Because of that, the only changes in impedance will arise from particles in the channel, making this range the optimal working condition. This behaviour is described in Figure 2.7.

Simplified ECM

The choice of the optimal frequency range leads to the possibility of having a simplified ECM. Considering the presence of the particle in the medium, the resulting ECM is modified to include the properties of the particle translated into electrical equivalents as Figure 2.8 shows.

The electrical elements remaining in the circuit are summarized in equations 2.8 and 2.9.

$$\tilde{Z}_{med} = \frac{R_{med}}{1 + R_{med} j\omega C_{med}} \tag{2.8}$$

$$\tilde{Z}_{particle} = \left(\frac{1}{R_{mem} + j\omega C_{mem}}\right)^{-1} + R_{cyto} \tag{2.9}$$

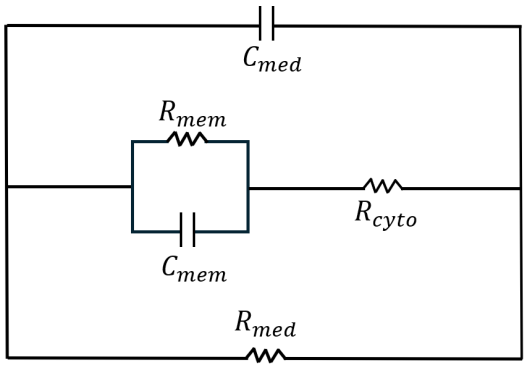

Figure 2.8: Sketch describing the simplified equivalent circuit model.

The impedance of the total simplified circuit is given by the parallel of the impedance of the medium and the particle:

$$\tilde{Z}_{tot} = \frac{\tilde{Z}_{med}\tilde{Z}_{particle}}{\tilde{Z}_{med} + \tilde{Z}_{particle}} \tag{2.10}$$

Substituting equation 2.9 and 2.8 inside 2.10 the total impedance response is finally described by equation 2.11

$$\tilde{Z}_{tot} = \frac{R_{med}[(\frac{1}{R_{mem}+j\omega C_{mem}}) + R_{cyto}]}{R_{med} + (R_{med}j\omega C_{med} + 1)\left(\frac{1}{R_{mem}+j\omega C_{mem}}\right)^{-1} + (R_{med}j\omega C_{med} + 1)R_{cyto}} \tag{2.11}$$

2.1.9 Examples of results of impedance characterization techniques

After discussing the principles of IFC and EIS it is worth to examine the possible outcomes of these characterization methods.
One of the most common analysis in EIS, involves computing the impedance modulus as a function of increasing frequency. In the specific case of a microorganism possessing a membrane, as bacteria, the expected behaviour observed is shown in Figure 2.9. This graph can be explained considering that the membrane resistivity of biological organisms like bacteria and cells, has a very high value, meaning that at lower frequencies there is an high impedance signal. When the frequency increases, the membrane capacitance gets short circuited and a frequency region where the contribute of the cytoplasm resistance is noticeable, as supported again by Figure 2.4.
In addition to the impedance magnitude, it is also possible to analyse the phase, which provides insights into the capacitive behaviour of the impedance in the selected frequency range.

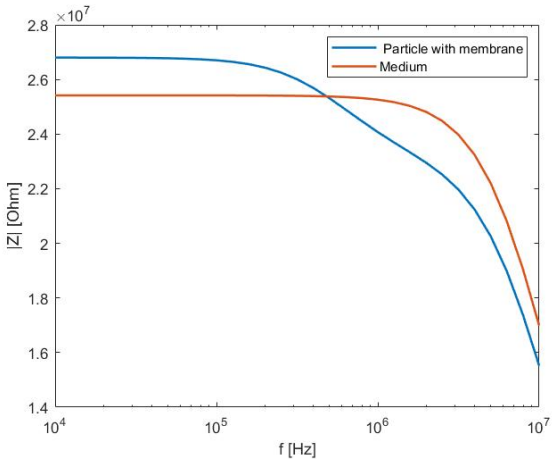

Figure 2.9: Impedance magnitude as a function of increasing frequency. Graph shows the difference in the signal recorded from the channel with and without a particle with a membrane.

Finally, we recall IFC and EIS are extremely useful to differentiate particles. Among the several approaches available for this analysis, one commonly used method is the computation of opacity. Opacity is defined as the ratio of the impedance obtained at an high frequency to the impedance calculated at a low frequency (Equation 2.12). Particles with different composition or internal structures will exhibit different opacity values [31].

$$\text{Opacity} = \frac{|Z(\omega_{\text{high}})|}{|Z(\omega_{\text{low}})|} \tag{2.12}$$

This parameter is computed in analyses such as those conducted by Kirkegaard et al. [32] and Holmes et al. [33], demonstrating the ability to differentiate between biological populations and beads, as shown in Figure 2.10.

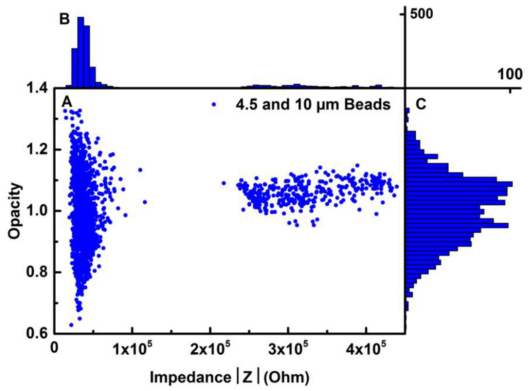

(a) Kirkegaard et al. [32]

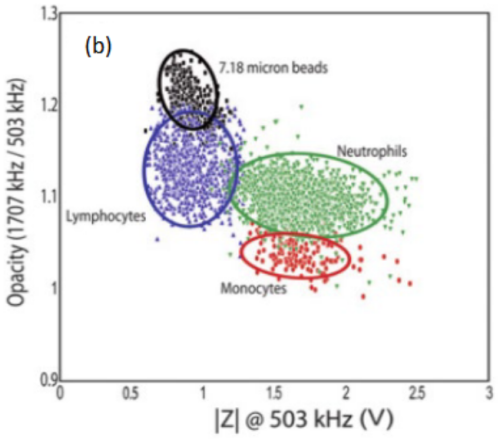

(b) Holmes et al. [33]

Figure 2.10: Two examples of the use of the Opacity to differentiate between different analytes. a) Uses opacity to distinguish beads of different dimensions, b) exploit this parameter to recognize population of three categories of white blood cells: Lymphocytes, Monocytes and Neutrophils. Beads are also present because they are useful in system calibration.

2.2 Microfluidics

As outlined in the introduction of this thesis, one of the aspects that can enhance the functionality of the biosensor developed in this project, is microfluidics. In microfluidic systems, the physical laws that govern macroscopic phenomena manifest differently as a consequence of scaling effects. In the specific case of the present device, the dimension of the fluidic channels widths were selected in a range of 10 µm up to 20 µm and the height was fixed at 10 µm This section will present the microfluidic concepts most relevant to its functioning.

2.2.1 Reynolds Number

In fluid dynamics, the Reynolds number Re is a dimensionless quantity, used to estimate the fluid flow patterns by measuring the ratio between inertial and viscous forces.

It is demonstrated that at low Reynolds numbers, generally below 2000, flows tend to be laminar: the fluid travels smoothly and can be depicted as consisting of thin layers, "laminae", all parallel to each other.
At high Reynolds numbers, flows tend instead to be turbulent. The turbulences are the outcomes of differences in the fluid's speed and direction, which means that the flow profile is rather irregular and can give rise to eddies. The transition from laminar to turbulent flow is not sharp, but appears gradually, depending on the specific conditions between $Re = 1500$ and $Re = 5000$. [34]

Reynolds number is described by Equation 2.13.

$$Re = \frac{\rho \overline{U}_m D_h}{\eta} \tag{2.13}$$

Where:

- ρ is the density of the medium.
- U_m is the maximum fluid velocity in the channel.
- η is the viscosity of the medium.
- D_h is the hydraulic diameter, which takes into account the physical dimensions of the channel and it is defined as:

$$D_h = \frac{2wh}{w+h} \tag{2.14}$$

When particles are suspended in a fluid, they are carried along with the flow and are subjected to drag and lift forces. The movement profile of the particle is inspected by the particle's Reynolds number.

$$Re_{particle} = \frac{\rho \overline{U}_{particle} \alpha^2}{\eta D_h} = \frac{Re_{channel} \alpha^2}{D_h^2} \tag{2.15}$$

Where α is the diameter of the particle. If the particle Reynold's number is equal or lower than 1, the particles will follow the streamlines, meanwhile, for higher values, inertial forces will act and the particle will undergo an effect known as inertial focusing [35].

The inertial forces which commonly act on the particles are the wall induced lift force and the shear gradient induced lift force. Because they can move the particles in the channel, even in laminar flow conditions, they are relevant for the device, since the position in the channel determines how easily the particle gets to the trap and is a crucial parameter when working with coplanar electrodes.

Considering a channel of cross section (10×10) μm^2, a density of $\rho = 1000$ kg/m^3 and a viscosity of $\eta = 0.001$Pa·s, the Reynold's number for a set of flow rates can be computed. The most used values during our experiments are reported in Tab 2.1.
Based on these results, it can be concluded that the fluid is moving in a fully laminar regime and no inertial forces affect the particles.

Table 2.1: Channel Reynolds number and Particles' Reynolds number in different sets of flow rate. The parameters used are: $\rho = 1000$ kg/m^3 , $\eta = 0.001$ Pa $\cdot$ s, $\alpha = 1$ µm $D_h = \frac{2 \cdot 10 \cdot 10}{10+10}$ µm.

Flow Rate Q	Re_{ch}	Re_p
0.01 µl/min	0.017	0.0007
0.05 µl/min	0.083	0.0033
0.10 µl/min	0.167	0.0066
1 µl/min	1.667	0.0667

2.2.2 Hydraulic Resistance

Hydraulic resistance represents the opposition of a fluid to flow within a certain path, and could be thought as analogous to electrical resistance in an electrical circuit. It is defined by the channel design and material properties such as density and viscosity. [36] The cross section of the elements composing the present device are shaped mostly as rectangles or squares and the hydraulic resistance in these cases is defined by equations 2.16, 2.17.

$$R_{hyd,square} = 28.4 \eta L \frac{1}{h^4} \tag{2.16}$$

$$R_{hyd,rectangle} = \frac{12 \eta L}{1 - 0.63 h/w} \frac{1}{h^3 w} \tag{2.17}$$

These formulas indicate that the smaller is the channel cross section or the longer is its length, the higher the resulting hydraulic resistance will be. As a consequence, the fluid will encounter greater difficulty in flowing through the channel.
The biosensor developed in this project needs to use small cross section elements, such as the trap. For this reason, the hydraulic resistance plays a fundamental role in determining the ease with which the fluid is reaching the trap bringing at least one particle to carry on the impedance spectroscopy analysis.

Moreover, the hydraulic resistance of a system is related to the pressure difference and the flow rate by the Hagen Poiseuille law [37]:

$$\Delta p = Q R_{hyd} \tag{2.18}$$

This equation implies that when a system presents high hydraulic resistances, the generation of high pressures inside the channel is to be expected. This has to be taken into account by tuning carefully the flow rate, in order to ensure the functionality of the device.

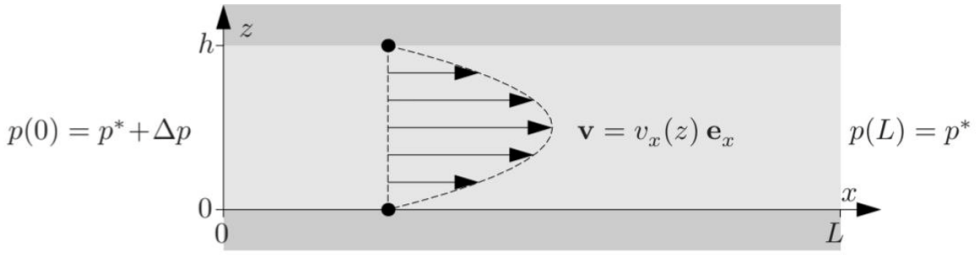

Figure 2.11: Illustration of the velocity profile along an infinite parallel-plate geometry. This figure is taken from [37].

2.2.3 Poiseuille Flow

When a pressure difference is established at the inlet and outlet of a channel, the injected fluid's motion will be described by the Poiseuille flow. These types of flows are generally found in straight long and rigid channels, therefore they are of major importance in the study of liquids in LOC systems. As most LOC systems, this project's device integrates a long microfluidic channel that can be approximated by an infinite parallel-plate configuration, as sketched in Figure 2.11. This approximation is demonstrated to be particularly accurate in low aspect ratio structures.

The governing equation of the fluid motions is represented by the Navier-Stokes equation. The complete Navier-Stokes is a non-linear partial differential equation, that in the case of an incompressible fluid is given by:

$$\rho\left[\partial_t \overline{v} + (\overline{v}\cdot\overline{\nabla})\overline{v}\right] = -\overline{\nabla}p + \eta\nabla^2\overline{v} + \rho\overline{g} \tag{2.19}$$

Where ρ is the fluid density, $\overline{v}$ is the fluid velocity, p is the pressure and $\overline{v}$ is the gravitational acceleration. The use of the infinite parallel-plate geometry allows for certain considerations that can simplify the Navier–Stokes equation:

- The fluid motion can be considered in steady state condition, leading to $\partial_t\overline{v} = 0$
- The channel geometry develops in the horizontal direction, thus the effect of gravity on the fluid can be neglected: $\rho\overline{g} \simeq 0$. This is also a scaling effect of the microfluidics regime.
- The flow, directed in the x-axis shows dependence only on the z-coordinate. This reduces the velocity term to $\overline{v} = v_x(z)\overline{e}_z$ and combined with the laminar flow regime, leads to the approximation of the non-linear term: $(\overline{v}\cdot\nabla)\overline{v} \simeq 0$

The resulting equation is therefore given by:

$$\partial_x^2 v_x(z) = -\frac{\Delta p}{\eta L} \tag{2.20}$$

This can be solved by the application of no-slip boundary conditions, according to which $v_x(0) = v_x(h) = 0$. The obtained velocity describes a parabolic profile [37]:

$$v_x(z) = \frac{\Delta p}{2\eta L}(h - z)z \tag{2.21}$$

This means that the fluid velocity reaches its maximum at the center of the channel and gradually decreases when approaches the channel walls. Knowing the velocity behaviour along the channel is relevant in our project as the performance of the characterization techniques such as IFC and EIS combined with coplanar electrodes are dependent on the particle position.

2.3 Hydrodynamic trapping for single particle analysis

Single particle analysis leads to a more accurate representation of particle properties, reducing biological noise from the target microorganism population, as opposed of methods where bulk measurement can only reflect average values summed over the responses of many cells [38].

In order to trap a single particle, different techniques have been inspected in literature, such as: hydrodynamic trapping, dielectrophoresis trapping, chemical trapping, gel trapping, magnetic trapping, acoustic trapping and laser trapping. Each with its own benefits and demerits.

Many of these processes necessitate the use of supplementary components, such as external pumps, specialized electronic systems or optical instrumentation, which are often not available in standard medical or biological laboratories, in particular when the aim is to develop a portable device. For this reason, the use of a system that can trap particles by its own geometry and without the need of many external components, makes the hydrodynamic trapping a suitable candidate for such applications.

Hydrodynamic trapping relies on built-in mechanical barriers or obstructions to isolate the target particle from the main flow. Once separated, the target particles are held inside designated trapping regions [39].

Methods used in hydrodynamic trapping mechanism are categorized in cross-stream migration, vortices based trapping and the externally controlled signal approach.

Cross-stream migration is a mechanism which allows particle to move in directions across

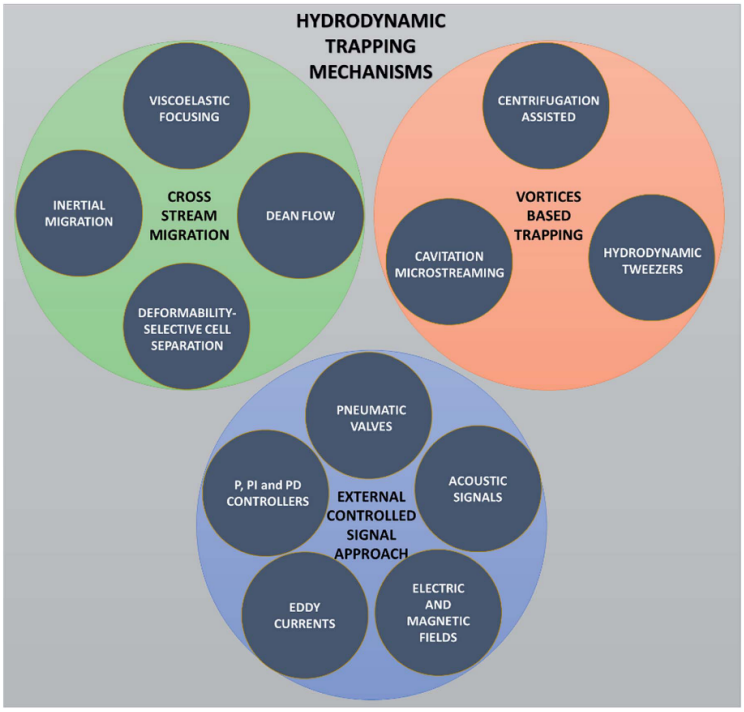

Figure 2.12: Schematic of the different groups of hydrodynamic trapping system with examples of specific techniques. [39]

streamlines of the flow to be directed towards specific locations within a channel, where they are trapped [40]. Vortices based trapping includes techniques which exploits the swirling natures of vortices to confine particles [41]. Externally controlled signal approaches refer to methods where particle trapping is achieved through the application of a control signal that is generated and modulated outside the system.

Among these three categories there are many specific applications that can be used, depicted in Figure 2.12

Furthermore, hydrodynamic trapping can be classified into two broader approaches: contact-based and contactless.

Contact based approach:

- *Lateral traps*: Traps are located along the path and particles get stuck in them while being dragged by the flow. They can be built by shaping the geometry of the channel or inserting elements such as jail bars or obstacles.

- *Vertical traps*: Trapping sites are placed underneath the streamlines and particles are moved inside them by gravity or other sedimentation effects. One example of vertical trapping are microwells [42].

Contactless based approach:

- *Trapping at stagnation point*: The trap site originates because flows coming from different directions intersect, creating a point where the fluid is stationary. As a result, the particle gets immobilized at this equilibrium point.

- *Eddy currents*: make use of the principle of the vortices based trapping.

- *Electric or magnetic fields*: The effectiveness of the traps is obtained by the application of electric and/or magnetic signals.

Some examples of the application of these techniques in literature are shown in Figure 2.13. After having summarized some of the most important hydrodynamic trapping methods, the choice of the trapping mechanisms applied to this project's device will be discussed in the following chapter, in order to give context to the associated design challenges and advantages.

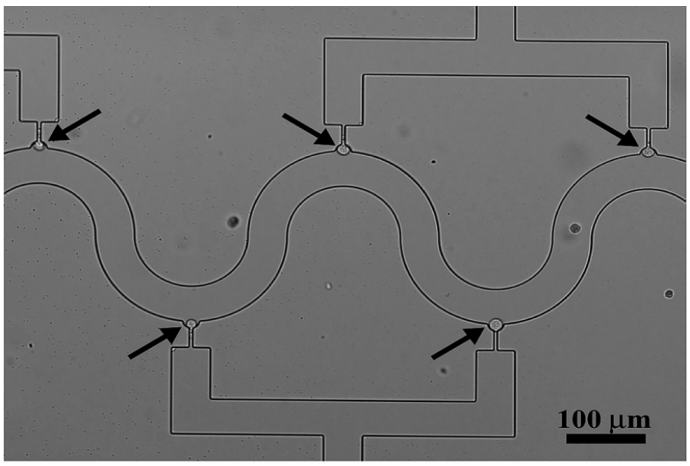

(a) Lateral trapping

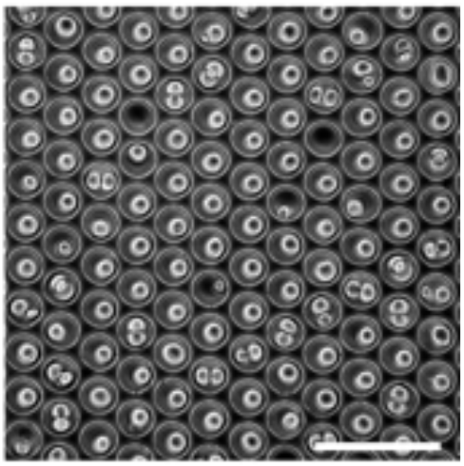

(b) Vertical trapping

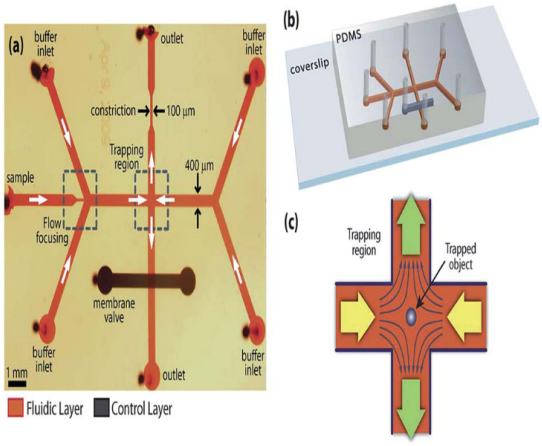

(c) Stagnation point trapping

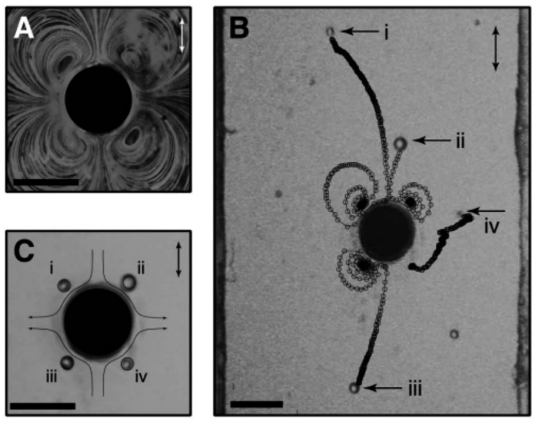

(d) Induced microeddies trapping

Figure 2.13: Examples of hydrodynamic trapping methods. a) Lateral trapping employed to isolate cell line of African green monkey kidney and rat primary brown preadipocytes [43]. b) Microwell array based trapping optimized for fibroblasts and rat basophilic leukemia cells[44]. c) Contactless technique of stagnation point trapping with a drawing that shows the functioning mechanism [45]. d) Three phases of the contactless technique based of steady streming microeddies, able to trap phytoplankton cells (*Prorocentrum micans*)[46].

Chapter 3

Microfluidic channel design and testing

In this chapter the design and testing of the microchannel will be discussed. First, the study that led to the model of the traps used in the final device will be discussed, analyzing the features that each idea brought. Subsequently, with the use of COMSOL Multiphysics, a software based on the finite element method (FEM), the designs will be simulated to prove their functionality. Finally, the effect of full-scan electrical impedance spectroscopy with a standard set of electrodes will be inspected to gain an overview of the challenges of integrating EIS in the chosen device.

3.1 Designs starting ideas

The first step towards the creation of the device was the ideation of the trap shape alongside with the design of the microfluidic channel where it is contained. The trap is the most crucial part of the device because it is aimed to capture particles comparable in size to *E. coli*, while at the same time meeting several critical requirements, such as:

- **Simplicity of fabrication technique**, as using the machinery at DTU Nanolab's cleanroom facility requires specific training and certain techniques could lead to excessively long production times, not suitable for a dynamic prototyping process (which will be discussed in more detail later on).

- **Adaptability for the integration of IFC and EIS system**, ensuring that there is enough space to have electrodes of a certain width and gap.

- **Stability of the final product** meaning that the trap has to show a decent robustness for the final replication process without collapsing or breaking.

After selecting the trapping method that relied only on geometry, a literature review was

conducted, leading to the identification of two articles with interesting concepts that inspired the design of the device:

- *Programmed trapping of individual bacteria using micrometer-size sieves*, by Kim Min-Cheol et al. [13]: This article, already presented in the state of the art section, presents an innovative and effective way to trap bacteria. In their project the traps are constituted by sieves of round shape that terminate with a channel restriction of 800 nm.

  The trapping capability relies on the creation of a stagnation point, caused by the very high hydraulic resistance around the trapping region, that leads the bacterium to move only by Brownian motion until it reaches the restriction and gets immobilized, achieving the single bacterium trapping. In the article, three alternatives for the shape of the sieves are analysed, employing, before the channel restriction, a triangular region with the vertex angle of 30°, 15° or 0°. The researchers were able to trap a single bacterium also by tuning the Colony Forming Unit (CFU), proving the effectiveness of this design. The shape of the device can be seen in Figure 3.1.

  However, two main issues can rise with the implementation of this system in the present project. First, employing a large number of traps could represent a problem during the fabrication of the device. As it will be explained later in details, the microchannels will be fabricated in the device using a type of silicone polymer, Polydimethylsiloxane (PDMS), which is poured, solidified and then detached from a stamp. Having these many extremely small structures increases the possibility of breaking and is a form of uncertainty of the correct replication of the device.
  On the other hand, the region of the circular chamber surrounding the traps may produce a detectable signal of other particles, as electrodes cross the structure in order to be connected with the other electronic components of the device, as depicted in figure 3.2. That could give a very low Signal to Noise Ratio (SNR) when it comes to read the signal from the single bacterium in the trap. It could, in principle, be adjusted with a post process correction, but in an optimal configuration it would rather be avoided.

- *A Microfluidic Device Integrating Impedance Flow Cytometry and Electric Impedance Spectroscopy for High-Efficiency Single-Cell Electrical Property Measurement* by Feng et al. [9]: In this publication, already mentioned in the introduction, the device presented implements the same functionalities of IFC and EIS characterization of the present project. For this reason, from the integration of the electrodes point of view, the article design is already efficient. However, since the device was designed to operate with cells -significantly larger than bacteria-, scaling down the trap dimensions to accommodate smaller particles may considerably increase the hydraulic resistance. This, in turn, could make the capture of a single particle a rare event, potentially resulting in no trapping occurrences within the expected duration of the experiment.

After all the considerations just discussed, six possible trap shapes were created and are shown in figure 3.4.

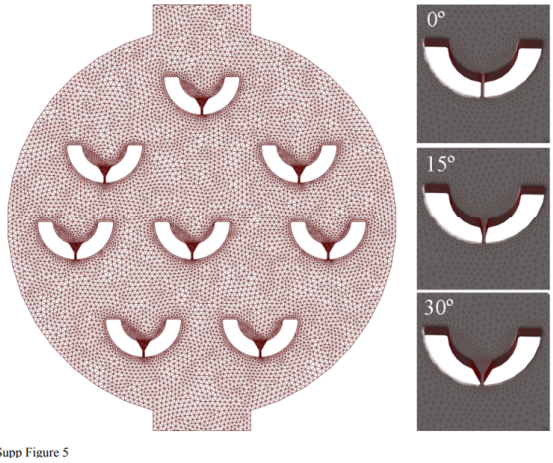

(a) Model of the sieves trap design with different angles used

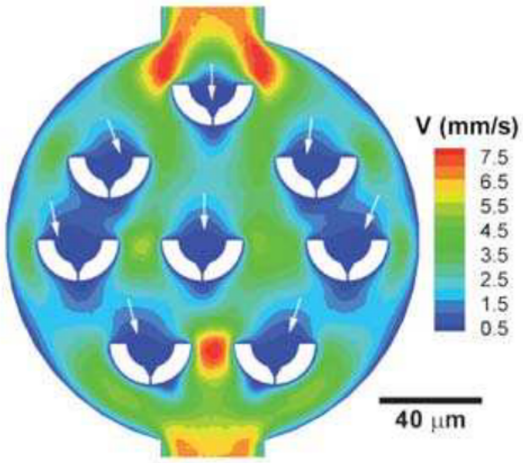

(b) Velocity simulation of the design

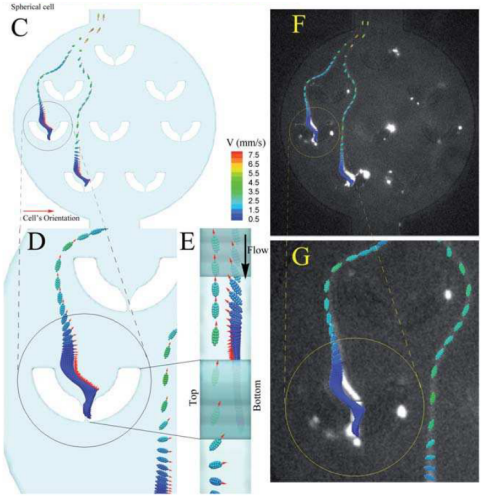

(c) Bacteria movement simulation and experimental result

Figure 3.1: Pictures describing the working of the Kim et al. design both in simulation and in real experiments. [13]

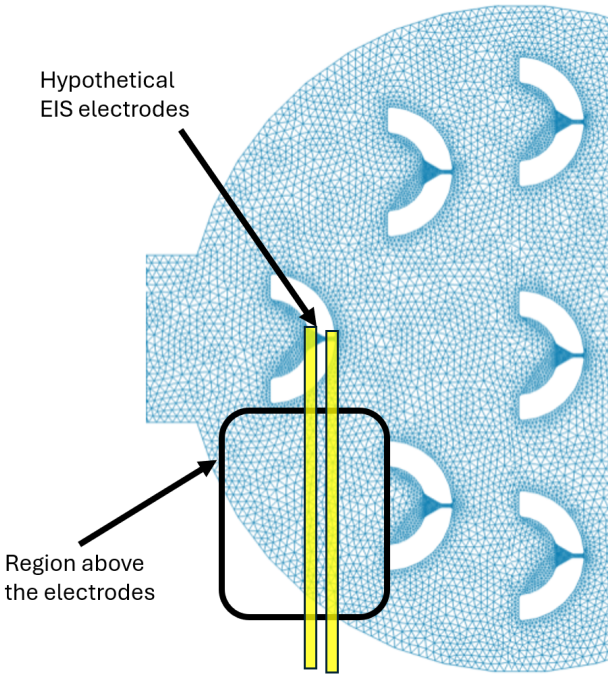

Figure 3.2: Graphical illustration of the additional region above EIS electrodes that could give signal, disturbing the characterization of the single bacteria in one of the traps. The original picture is taken from Supplementary Material of [13] and edited.

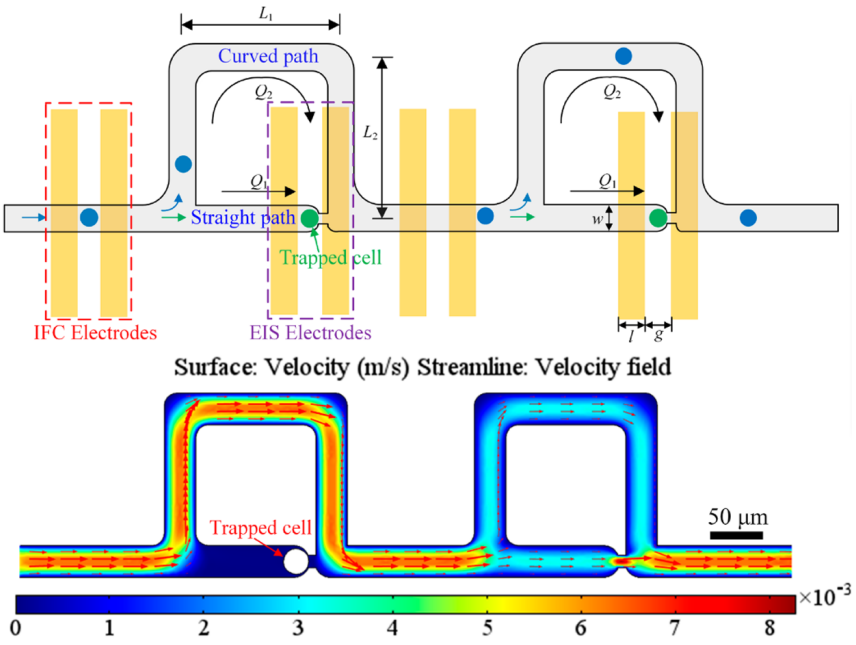

Figure 3.3: Structure and velocity simulation of Feng et al. design.[9]

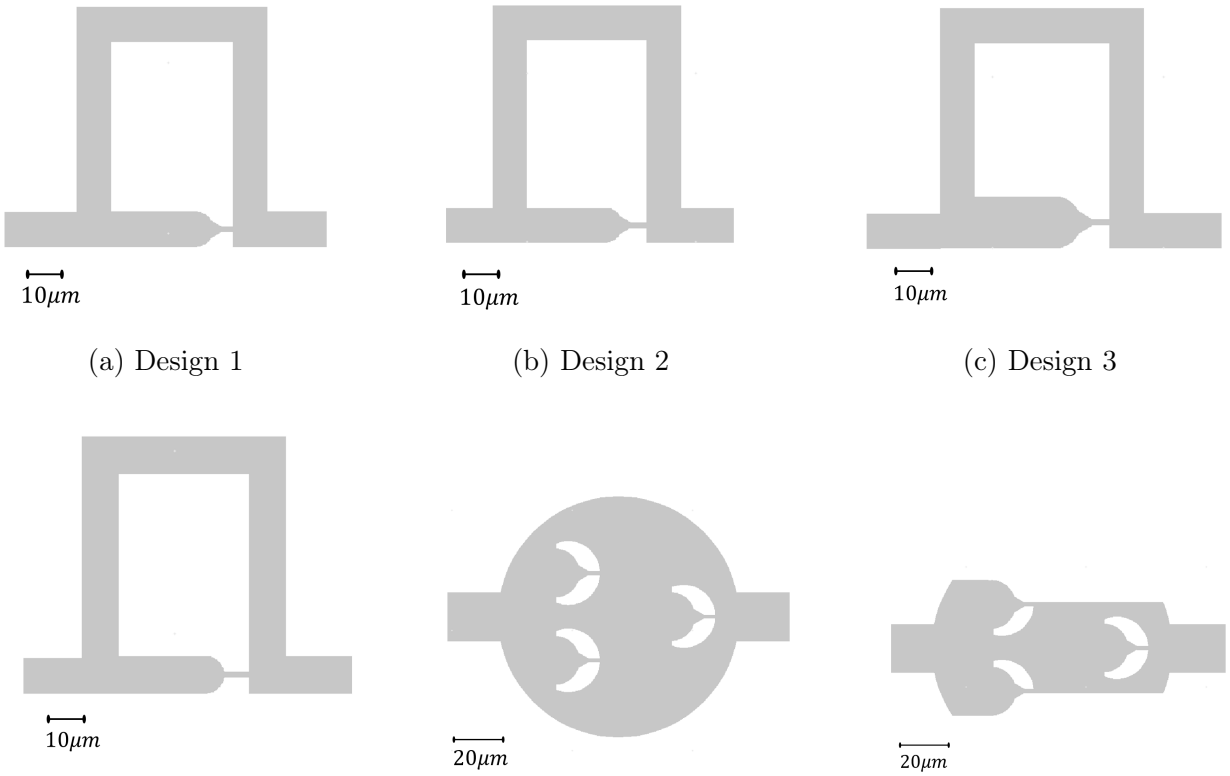

(a) Design 1 (b) Design 2 (c) Design 3

(d) Design 4 (e) Design 5 (f) Design 6

Figure 3.4: All trap designs used in this project.In each of the designs the total channel height was set to be 10 µm

As can be noticed by inspeting Figure 3.4, *Desings 1,2,3* and *4* are mainly inspired by Feng et al. design (Figures 3.4a-3.4c-3.4b-3.4d) yet they present some differences: *Design 1* shows a triangular region before the channel restriction. The vertex angle of the triangle restriction is 30°, as used by Kim et al. in their work. This feature was chosen among the other options, because it was proven in the article to have a lower hydraulic resistance. Here the length of terminal narrow channel of the trap site is 3 µm. A detailed description of this design is presented in Figure 3.5. Other structures details are instead contained in Appendix B.

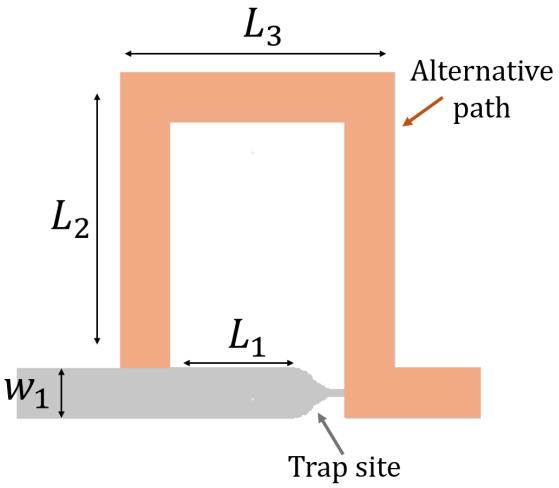

Figure 3.5: Design 1 details

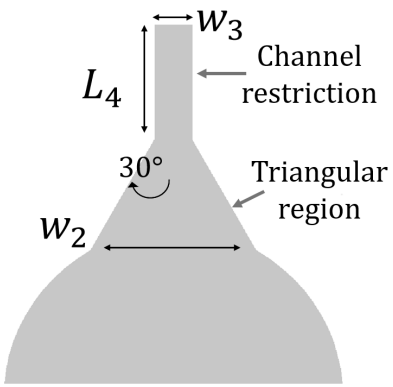

Figure 3.6: Trap 1 details

Table 3.1: Lengths and widths of Design 1

L_1	L_2	L_3	L_4	w_1	w_2	w_3
25 µm	60 µm	55 µm	3 µm	10 µm	5 µm	1 µm

Design 2 has the same structure as *Design 1*, but the length of the restricted channel is 5 µm. This was chosen to test the impact of an higher hydraulic resistance on the trapping events and to allow more room for wider EIS electrodes.

Design 3 presents a wider channel containing the trapping site. This was decided in order to inspect the impact of other channel's features on the total hydraulic resistance.

Design 4 is reproducing the trap shape originally presented in the Feng et al. article, in association with an higher length of the trap channel, which in this design is 7 µm, consequently allowing greater space for EIS electrodes.

The geometries *Design 5* and *Design 6* are mainly inspired by Kim et al. work, implementing further modifications.

Design 5 is a simplified version of the original structure described in the article, where the number of trap sites was decreased and the dimensions reduced. This design was selected, despite the explained limitations, in order to evaluate their impact and assess its functionality for the present project device.

Design 6 partially eliminates the issue of having other parts of the microfluidic channel crossing the EIS electrodes, by cutting the regions surrounding the traps, while retaining one structure on the original configuration for a simultaneous comparison between signals. Both *Design 5* and *Design 6* have a trap's channel length of 5 µm.

Since it was possible to integrate multiple chips on the same wafer during the fabrication process, all designs were phisycally produced.

3.1.1 Hydraulic resistance considerations

The first meaningful evaluation was the computation of the hydraulic resistance of the channel path that contains the microfluidic trap, in order to study the effect of the cross section's variation of the various elements.

For easier calculations, only the first four designs were analysed. The geometrical details can be consulted in Appendix B.
The total hydraulic resistance is described by:

$$R_{Hyd_{TOT}} = R_{Hyd_{ch}} + R_{Hyd_{trap}} \tag{3.1}$$

Where $R_{Hyd_{ch}}$ and $R_{Hyd_{trap}}$ are described by equations 2.16 and 2.17 since the cross section can be a square or a rectangle depending on the specific feature under analysis.

Table 3.2: Comparison of hydraulic resistances computed in the first four designs.

Design 1	
$R_{Hyd_{ch}}$	$7.38 \cdot 10^{13}$ Pa · s / m^3
$R_{Hyd_{trap}}$	$3.84 \cdot 10^{15}$ Pa · s / m^3
$R_{Hyd_{TOT}}$	$3.92 \cdot 10^{15}$ Pa · s / m^3

(a) Design 1

Design 2	
$R_{Hyd_{ch}}$	$7.38 \cdot 10^{13}$ Pa · s / m^3
$R_{Hyd_{trap}}$	$6.40 \cdot 10^{15}$ Pa · s / m^3
$R_{Hyd_{TOT}}$	$6.48 \cdot 10^{15}$ Pa · s / m^3

(b) Design 2

Design 3	
$R_{Hyd_{ch}}$	$2.28 \cdot 10^{13}$ Pa · s / m^3
$R_{Hyd_{trap}}$	$6.40 \cdot 10^{15}$ Pa · s / m^3
$R_{Hyd_{TOT}}$	$6.43 \cdot 10^{15}$ Pa · s / m^3

(c) Design 3

Design 4	
$R_{Hyd_{ch}}$	$7.38 \cdot 10^{13}$ Pa · s / m^3
$R_{Hyd_{trap}}$	$8.96 \cdot 10^{15}$ Pa · s / m^3
$R_{Hyd_{TOT}}$	$9.04 \cdot 10^{15}$ Pa · s / m^3

(d) Design 4

From the results depicted in tabs 3.2 it is possible to conclude that the trap channel is the

most influent component on the total hydraulic resistance. A slight change of the length of this feature provokes a noticeable increase of the hydraulic resistance, while a modification of a geometrical parameter in another part of the channel has almost no effect on the total result.

3.2 COMSOL simulations

COMSOL was used as a simulation tool to gain insights of the device's behaviour before having a physical device ready for testing.

The initial analyses aimed to estimate the extent to which the flow would be directed into the trap, both prior to and after the capture of a bacterium. Subsequently, particle trajectories approaching the trap were modeled to investigate the dynamics, and finally, the results of the EIS characterization were simulated for one of the proposed trap designs.

3.2.1 Flow distribution inside the trap

Following the calculations of the hydraulic resistance of the system, it became clear that this value could be considerably high. One possible consequence of this is the reduction of the flow reaching the trap to bring analytes.

In principle, this is not necessarily a negative outcome, since a low percentage of flow from the inlet reaching the trap also implies that fewer bacteria are likely to approach it. This, in other words, increases the likelihood that enough time will pass between the trapping of a bacterium and the possible arrival of a second one, allowing the full scan of the selected frequency range to be completed on a single particle. Nevertheless, it was of interest to quantitatively evaluate the flow rate entering the trap across the different design configurations.

Channel without trapped bacteria

The first COMSOL simulation performed regarded the channel filled only with the liquid. To carry on the simulation, a 2D geometry was and the trap designs where imported on COMSOL geometry panel. Laminar flow physics was chosen, which allowed to calculate the velocity and pressure fields for the flow of a single-phase fluid, associated with a stationary study.

Although the simulation was implemented in 2D, it was necessary to provide COMSOL with information reflecting the three-dimensionality of the structure. This was achieved selecting the 'Shallow Channel Approximation' mode and specifying the height parameter of the device, which is 10 µm. The information about the flow profile along the channel's height is included by adding a term to the Navier-Stokes equation that COMSOL uses to

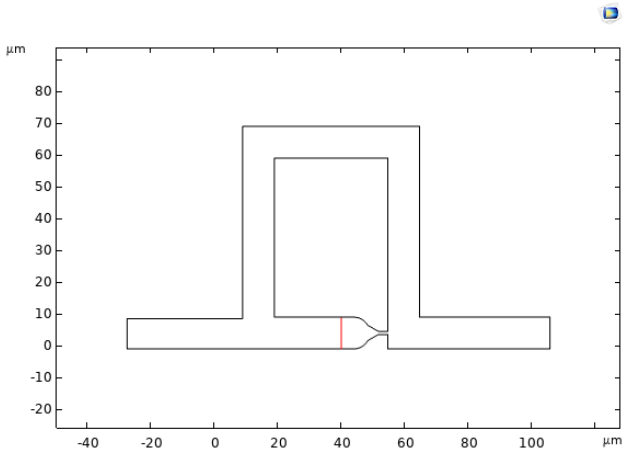

Figure 3.7: Cut line location on the 2D simulation

solve the microfluidics simulation. This term is given by equation 3.2

$$\overline{F}_{\mu} = -12\eta\frac{\overline{u}}{h^2} \tag{3.2}$$

After that, the flow rate was set to an initial value of 10 µl/min. In COMSOL, the laminar flow physics module allows other parameters to be specified as initial conditions, such as pressure or velocity. In this study, the flow rate was chosen as it corresponds to the parameter controlled during the actual experiment.

The mesh was configured as a fine, physics-controlled mesh, meaning that COMSOL generates a standard mesh that automatically adapts to the laminar flow physics settings.

After the simulation was completed, the flow rate was computed in the channel containing the trap.
The Hagen-Poiseuille law, (Equation 2.18), that describes the relation between the flow rate, the pressure difference and the hydraulic resistance, can be seen as an equivalent of the Ohm law, where the pressure difference corresponds to voltage, the flow rate to current and hydraulic resistance to electrical resistance. Consequently, it is reasonable to assume that the flow rate will remain constant in all sections of the channel connected in series.

A cut line was placed in the channel as can be seen in Figure 3.7 to compute the average flow velocity. In order to have easier calculations in *Design 5* and *Design 6* the cutline was placed right inside the trap. Finally, the total flow rate was computed by:

$$Q = \overline{v}wh \tag{3.3}$$

Where $\overline{v}$ is the average flow velocity extracted from COMSOL and w and h are the geometrical parameters of the cross section.

Results

Following data collection, the percentage of flow entering the path containing the trap was calculated. This provides an overview of the impact of hydraulic resistance on the fluid motion.

The numerical results are shown in Tables 3.3 and 3.4

Table 3.3: Comparison of percentage flow rates ($\%Q_{in}$) for four different designs.

	Design 1	**Design 2**	**Design 3**	**Design 4**
$\%Q_{in}$	7.6%	5.70%	5.71%	4.2%

Table 3.4: Flow rate distribution ($\%Q_{in}$) for selected traps across two designs.

	Design 5	**Design 6**
$\%Q_{in}$ **right trap**	0.31%	1.68%
$\%Q_{in}$ **upper left trap**	0.24%	1.06%
$\%Q_{in}$ **lower left trap**	0.24%	1.06%

In figure 3.8 the velocity magnitude and the streamlines of the flow are illustrated. As can be noticed, in *Design 5* and *Design 6* the velocity around the trap region is very low in accordance to the reference article's design in Figure 3.1b.

Channel with trapped bacteria

Once the simulation without the particle was completed, it became interesting to observe the changes introduced by the presence of a bacterium inside the trap. Due to the high aspect ratio of this project's designs (channel's height fixed to 10 μm to prevent structures collapsing) it was taken into account that a single bacterium could not be expected to significantly increase the hydraulic resistance of the trap, drastically reducing the percentage of flow passing through and preventing other bacteria to reach the trap. This simulation aimed to prove this assumption.

In order to get reliable outcomes, a full 3D model was needed in this simulation, as the SCA used in 2D does not consider the height at which the bacterium is placed, although it has an influence on the flow velocity profile on the z-axis.

The bacterium was modeled on COMSOL s a three-dimensional ellipsoid with one axis measuring 2 µm and the other two measuring 1 µm.

To replicate the computation on the 3D geometry a y-z parametric was positioned at the

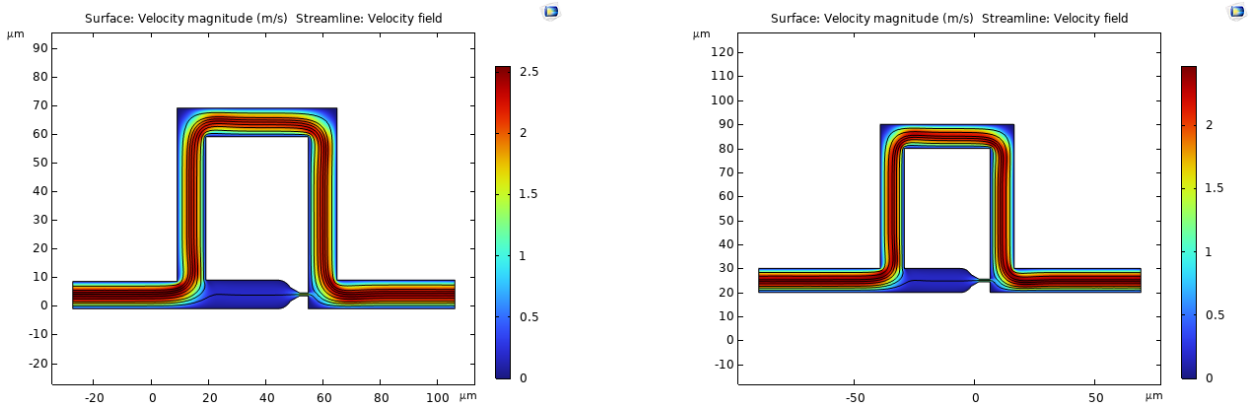

(a) Design 1

(b) Design 2

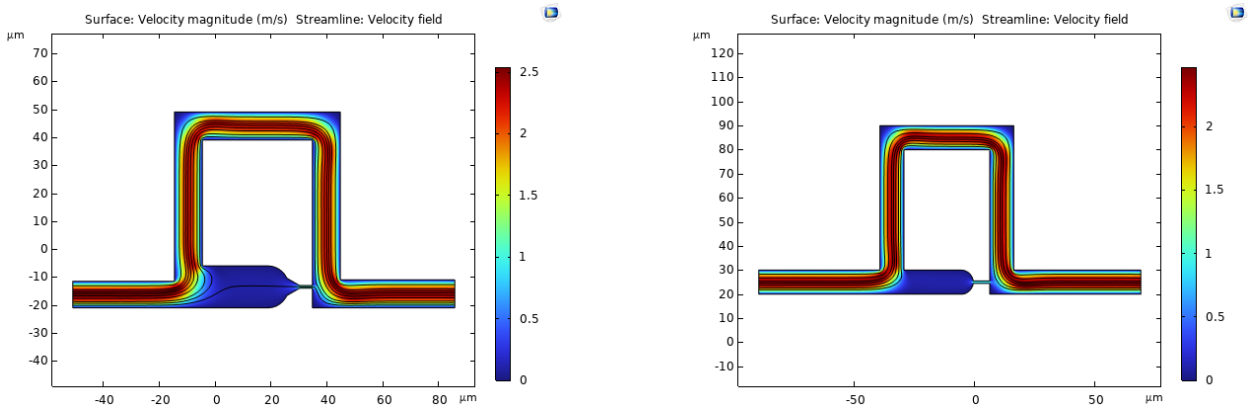

(c) Design 3

(d) Design 4

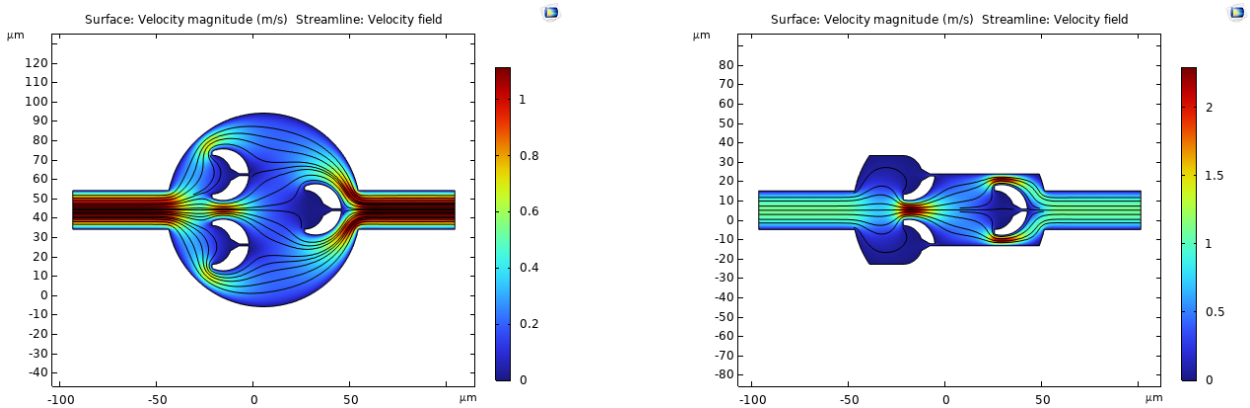

(e) Design 5

(f) Design 6

Figure 3.8: COMSOL velocity simulation on different trap designs.

location corresponding to the previous cut line.The flow rate was finally obtained by integrating the velocity over this surface.

Results

In the first computation, one and successively more bacteria were added in the trap. The bacterium orientation was chosen as parallel to the x axis, as it is shown in Figure 3.9a

The simulation was conducted only on *Design 2*, as the conclusions can be extended to all other geometries.

Table 3.5: Results showing the percentage of inlet flow rate reaching the channel containing the trap site and the corresponding total hydraulic resistance, evaluated for different numbers of bacteria and compared to the case with no bacteria. The reference geometry is *Design 2*

	$\%Q_{in}$	$R_{Hyd_{TOT}}$
No bacteria	5.70%	$6.48 \cdot 10^{15}$ Pa · s / m^3
1 bacterium	5.48%	$8.39 \cdot 10^{15}$ Pa · s / m^3
2 bacteria	5.04%	$9.13 \cdot 10^{15}$ Pa · s / m^3
4 bacteria	3.9%	$1.18 \cdot 10^{16}$ Pa · s / m^3
6 bacteria	2.4%	$1.85 \cdot 10^{16}$ Pa · s / m^3

By looking at Table 3.5, it can be observed that when the first bacterium approaches the trap the hydraulic resistance of the total path does increase, lowering as a consequence the percentage of the inlet flow rate found the in the channel containing the trap. However, this increase is minimal and for this reason, the presence of a single bacterium itself does not constitute a sufficient condition to prevent other bacteria to approach the trap.

A more significative change is seen when four bacteria are located inside the trap, as the hydraulic resistance increases of approximately one order of magnitude and the percentage of the inlet flow rate in the trap channel is halved. It is to however to be recalled that the aim of these simulation is to identify trends and predictable changes, as in real experiments bacteria may vary in size even if they belong to the same species. Therefore, it would be inaccurate to quantify the exact number of bacteria based purely on these results.

To have further insights, the orientation of the bacteria within the trap was varied (Figure 3.9) to evaluate the effects when all bacteria were aligned vertically or in a random position.

As can be observed from the results reported in Table 3.6, the position of the bacteria signif-

Table 3.6: Flow rate distribution ($\%Q_{in}$) for selected traps across two designs.

	Horizontal	**Vertical**	**Randomized**
$\%Q_{in}$ **with 3 bacteria**	4.56%	3.75%	4.23%

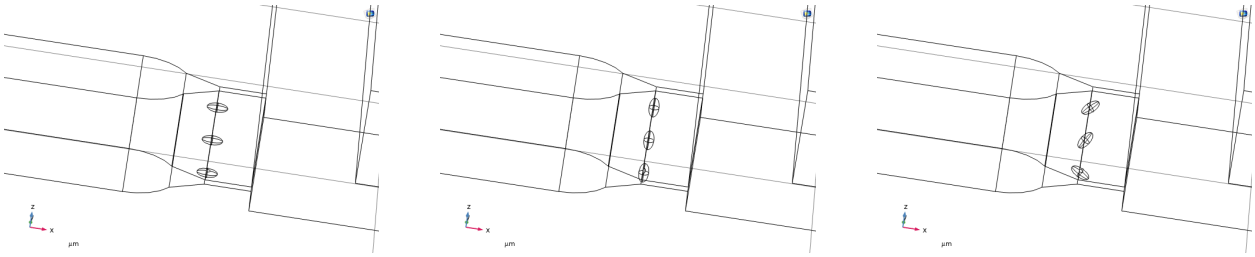

(a) Bacteria oriented parallel to x-axis

(b) Bacteria oriented parallel to z-axis

(c) Bacteria with random orientation

Figure 3.9: Three bacteria placed inside the traps with different positions. In this picture we can also clearly see the high aspect ratio of the trap and how the orientation of the bacteria change the way the trap appears obstructed.

icantly influences the amount of flow received by the trap. This is because vertically aligned bacteria occupy a larger portion of the channel's cross-section, thereby having a stronger impact on the hydraulic resistance. In fact, the behaviour observed with three vertically aligned bacteria produces a similar effect to that of four horizontally aligned bacteria.

3.2.2 Movement of the bacterium

The considerations regarding the effects of the bacterium's orientation led to an investigation on its movement within the channel. To do this, a 2D simulation was set, where the bacterium is treated by the software as an object carried along by the laminar flow, thus re-creating its actual motion. This was achieved using a feature called 'moving mesh' by the means of which the mesh can change shape adapting to physical phenomena and allowing the bacteria to realistically interact with the boundaries of the geometry. Two scenarios were simulated: first, the bacterium was placed at the inlet of the channel; subsequently, it was positioned directly at the entrance of the path containing the trap, as it was not possible, under these settings, to introduce a large number of particles to observe a spontaneous trapping event.

Results

The results of the simulation are shown in Figure 3.10. When the bacterium was placed at the inlet of the channel, it moved to the location with the lower hydraulic resistance, therefore following the alternative path, as expected (Figure 3.10a). In the second set up, the bacterium aligned its longer axis to the velocity streamline, and approached the trap's channel in an horizontal position, helped by the funnel conformation of the trap site. By inspecting the real time simulations, it was observed that if the object was placed in the center of the channel, parallel to the flow streamlines, it showed only a traslational movement, while if it was placed even slightly off axis, it began to rotate.
This is because, according to the laminar flow velocity profile, the maximum velocity is found in the center and it decreases gradually until it becomes zero at the boundaries, due to the no slip conditions. As discussed in Section 2.2.3, this creates a gradient of the velocities,

such that when the particle travels in the flow with an angle, it is subjected to different drag forces acting along its profile which create a torque moment.

The simulation presented several limitations, as the use of the moving mesh significantly increased computational complexity. Each run required a long simulation time and once the object fully entered the trap, it failed due to difficulties in adapting the mesh in the narrow space between the particle and the channel walls. Moreover the use of 2D simulation, as explained in the previous section, does not take into account the threedimensionality of the bacteria and its effect on the flow profile in the z-axis, for this reason it is to be expected a different behaviour in the real case.

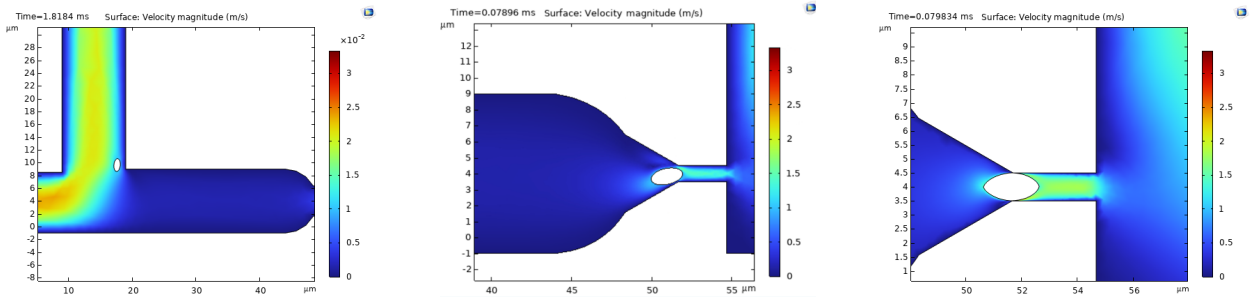

(a) Bacteria following the alternative path

(b) Bacteria approaching the trap

(c) Bacteria in the final position inside the trap

Figure 3.10: Pictures showing different position occupied by the particle during its real time-movment. a) Is the outcome of the first simulation, while b) and c) are two subsequent moments of the second.

3.2.3 Full impedance scan simulation

The characterization functionality of EIS electrodes combined with the trap was finally tested. To simulate full-scan impedance spectroscopy, a single geometry was again selected among those previously proposed.

The first step was to model the electrodes. In the work presented by the colleague Sara Pittelli, extensive optimizations were performed on the electrodes design to improve the results of IFC analyses. These optimizations showed that, for particles as small as bacteria and with a channel cross section of 10 µm × 10 µm, the electrode width should be 10 µm. With smaller widths, the signal recorded from the electrodes was proven to be lower. These results are included in Appendix A.

However, these important findings are not directly applicable in the region of the channel currently analyzed, since the space available around the location where the particle will be trapped is significantly more limited. On the other hand, this section of the channel is much narrower, therefore the design considerations may differ. To address the spatial constraints, electrodes with a 2.5 µm width and gap were tested.

The impedance characterization conducted in the simulation aimed to test the correct working of the electrodes in the chosen configuration as a proof of concept.

The particle used for the tests is modelled with two ellipses that represent the cytoplasm and the membrane. Details on the structure and the electrical parameter are showed in Table 3.7.

Table 3.7: Electrical properties of the medium, membrane, and cytoplasm.

	Medium	**Membrane**	**Cytoplasm**
Conductivity σ [S/m]	0.04	$1 \cdot 10^{-16}$	0.6
Dielectric permittivity ϵ_r	80	16	60

To perform this analysis on COMSOL the **Electric Currents** physics was selected, which is used to compute electric fields, currents and potential distributions in conducting media. After that, 3 V were associated to the first electrode, in accordance to IFC simulations conducted by the colleague Sara Pittelli, and 0 V to the second. Finally, frequency was swept between 10 kHz and 10 MHz.

Data were analyzed with a simple MATLAB script that reads the exported file from COMSOL and computes the magnitude of the current, starting from its real and imaginary parts, and converts it to impedance by applying the Ohm's Law.

Results

The first simulation was performed with the bacterium placed in the center of the channel. Here, it was possible to observe that the recorded signal deviated from expectations, because no impedance variation caused by the cytoplasm was recorded. For this reason two parameters were tuned: the height of the channel, while keeping the particle positioned at mid-height, and the distance of the particle from the electrodes, without changing the geometry.

By decreasing the height of the channel, the signal of the impedance got progressively better. This can be attributed to the more uniform distribution of the electric field along the z-axis, which makes the signal to be recorded from higher parts of the channel. Figure 3.11

By lowering the height of the particle and placing it at 1 µm distance from the electrodes, the simulation showed a clear variation in the impedance profile, as can be noticed by looking at the decrease around the frequency of 100 kHz in Figure 3.12. This is because a closer particle experiences stronger effects of the electric, giving an higher signal.

Once that this optimal position in the z-axis was found, it was inspected the role of the particle location in the trap along the x-axis. The object was initially placed in the middle

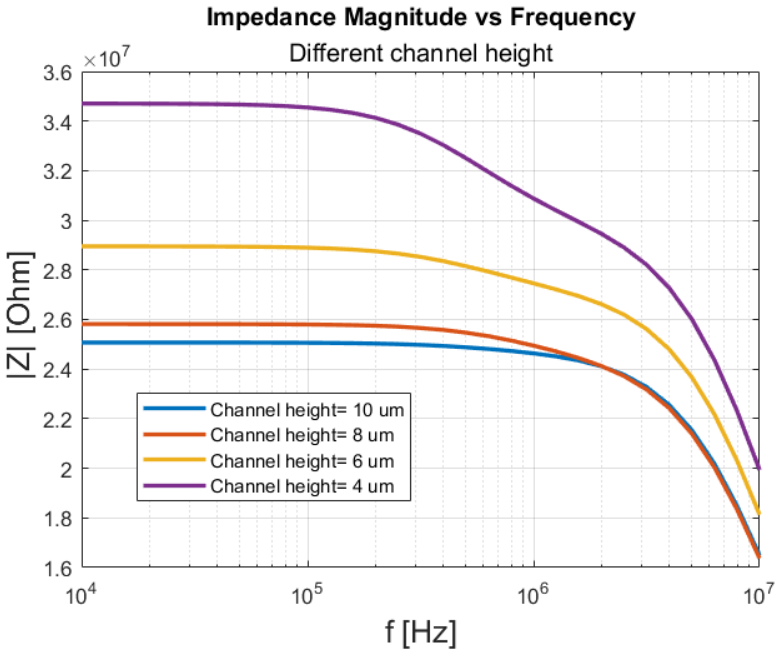

Figure 3.11: Impedance variation of a bacterium as a function of frequency when the height of the channel is reduced.

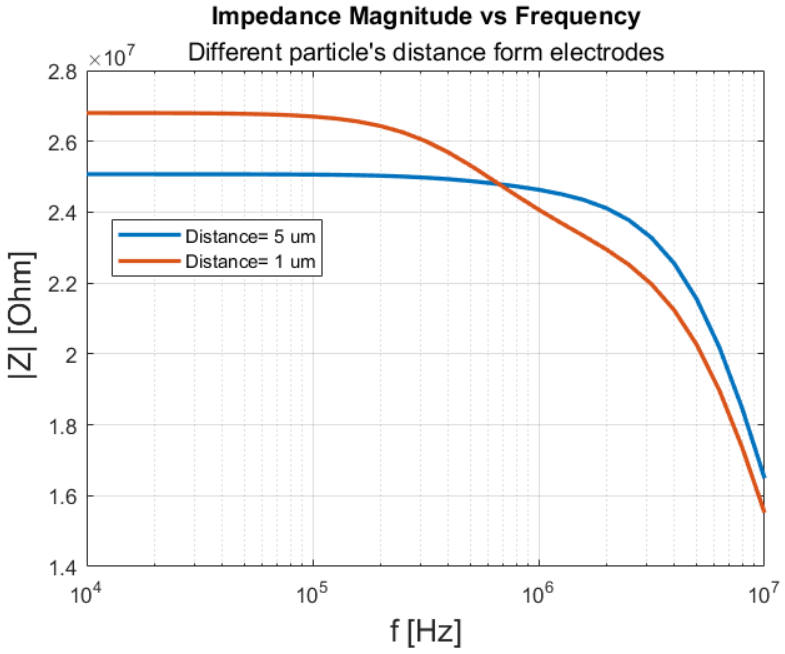

Figure 3.12: Impedance variation as a function of frequency when the height distance of the bacterium from the electrodes is reduced.

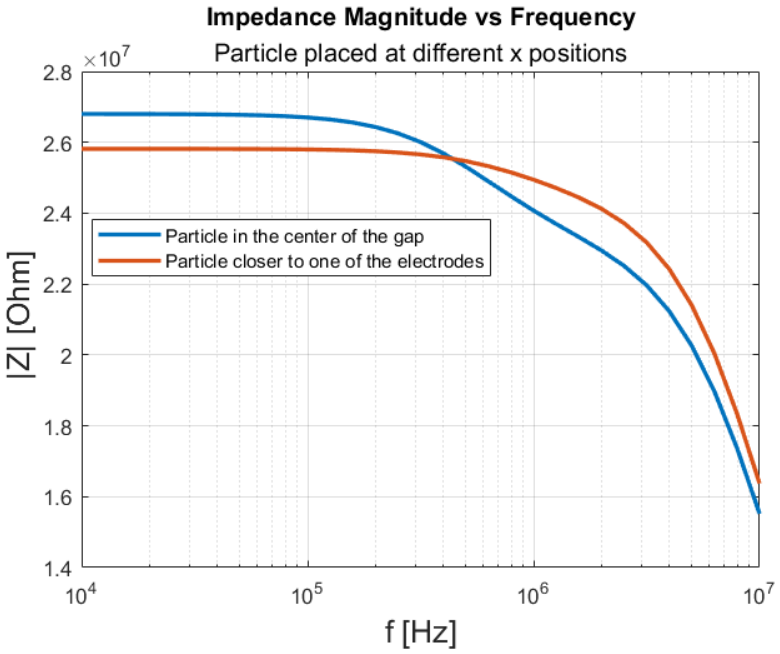

Figure 3.13: Impedance variation as a function of frequency when the bacterium is placed either at the center of the gap or in a different x position. The height distance from the electrodes is kept at 1 µm.

of the gap between electrodes, that is, as explained in the previous chapter, the position that maximizes the recorded signal.
The results were compared to those coming from the object placed slightly towards the right electrode, on top of which 3 V are applied. This analysis, the results of which are presented in Figure 3.13, confirmed the dependecy of the signal on the particle x-position and implies that, during device fabrication, the correct alignment of the structures plays a critical role in signal detection.

Moreover, the membrane thickness was increased, switching it from 10 nm to 100 nm. Using the latter thickness, it was noticeable that the impedance measured at different frequencies tends to resemble that of a fully insulating body, such as a bead, rather than that of a particle with an inner conductive region (Figure 3.14). This is due to the fact that a thicker membrane has an effect on the capacitance equivalents: the capacitance will decrease according to equation 3.4, which relates it to the membrane thickness, represented by the parameter d.

$$C = \epsilon_0 \epsilon_r \frac{A}{d} \tag{3.4}$$

If membrane's capacitance decreases, its capacitive impedance will consequently increase. This means that the membrane will become more difficult to charge or less "transparent" to the electric field at these frequencies.

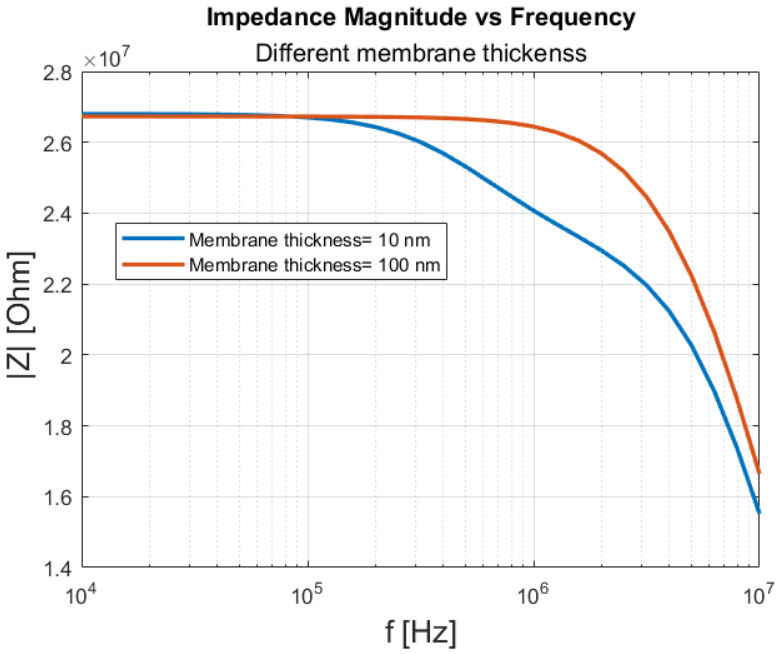

Figure 3.14: Impedance variation as a function of frequency when the membrane thickness of the bacterium is increased from 10 nm to 100 nm. The particle remains placed at an height distance of 1 µm from the electrodes and centered in the electrode's gap

3.3 Chapter summary

This chapter has presented the steps that led to the design of the microfluidic trap implemented in the device. COMSOL simulations highlighted how achieving single-particle trapping is challenging when an high aspect ratio structure is employed; however, the results may vary depending on the final positioning of the particles within the trap. Furthermore, through EIS characterization simulations, the limitations of using coplanar electrodes were demonstrated, showing how the recorded signal is strongly influenced by both the channel geometry and the particle's position inside the trap.

Chapter 4

Device micro-fabrication

In this chapter the micro-fabrication processes that were employed to obtain the final device will be presented and discussed. Cleanroom work was central to this project and a large portion of time was spent at DTU Nanolab facilities where device components were fabricated and characterized. In the following, the proposed process flows will be presented, analysing the choices made and the challenges encountered during fabrication will be discussed, explaining the several optimisation steps that were performed.

4.1 Fabrication objectives and constraints

The fabrication processes involved two main components of the device: the metallic electrodes for IFC and EIS characterization and the mold onto which PDMS would later be poured, in order to form the microfluidic channels containing the trap, once solidified.

The key aspects to consider during this stage of the project were the fabrication of electrodes with sufficient definition and robustness, as well as the achievement of a high resolution of the trap pattern. This latter goal is particularly critical, as effective trapping of bacteria requires the trap width to be smaller than the diameter of the bacterium. Achieving this means working with resolutions below 1 µm, approaching the nanometric scale.

This presented a significant challenge for the process, especially considering the additional constraint of using techniques and equipment that would keep the fabrication process as simple as possible. Indeed,not only certain machines require long processing times, but it is also mandatory to undergo training sessions in order to gain access to cleanroom tools, which are sometimes divided into multiple steps. Therefore, efforts were made to minimize the number of required trainings and the total process time needed, in order to prioritize the fabrication of the device within the planned project schedule, with the possibility to optimize the steps if required.

4.1.1 Process flows overview

The starting point of the the cleanroom work is the creation of a process flow. This contains all the steps that need to be performed and the useful informations regarding the fabrication techniques that are chosen, e.g. name of the recipes, deposition rates, thicknesses and typology of photoresist, etc.

Two separate process flows for the electrodes and for the mold were required. Figures 4.1-4.6 show a simplified schematic that represents the steps included in the process flows, which will be explained in detail in the following sections. The original process flow documents used in the cleanroom are instead contained in Appendix C.

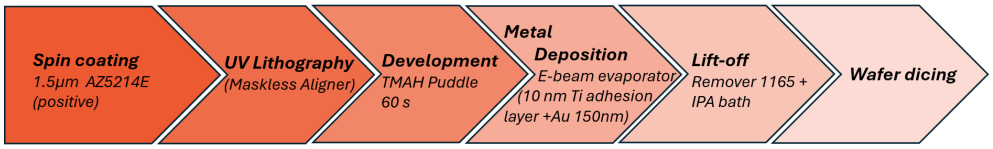

Figure 4.1: Schematic of Electrodes process flow

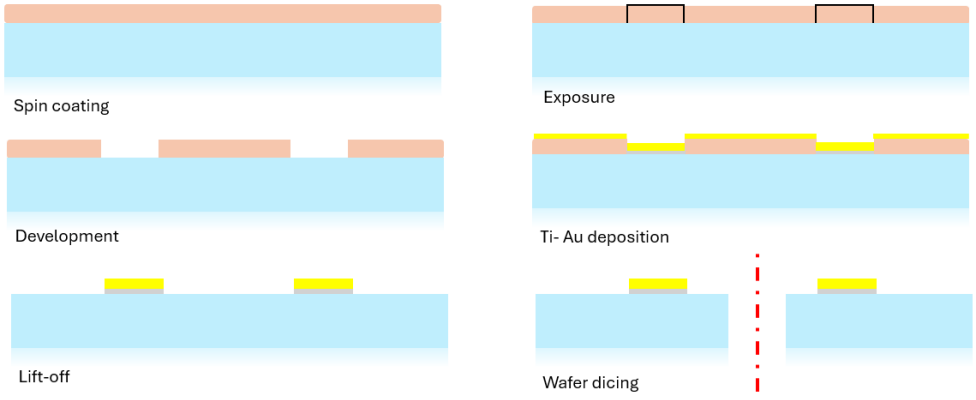

Figure 4.2: Graphical illustrations of the electrodes fabrication steps

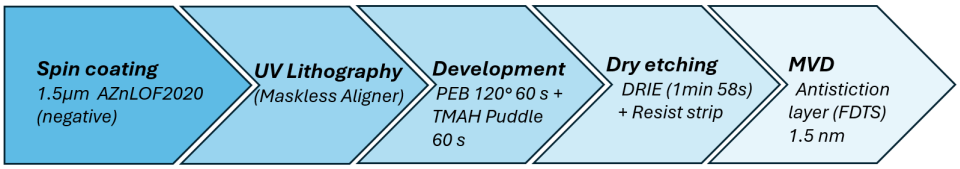

Figure 4.3: Schematic of the silicon mold process flow.

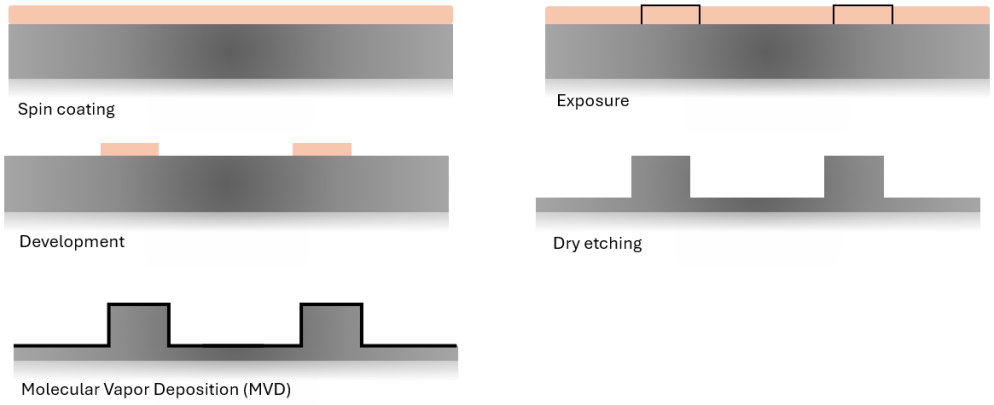

Figure 4.4: Graphical illustrations of mold's fabrication steps

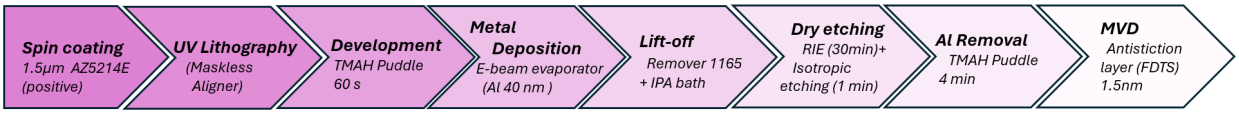

Figure 4.5: Schematic of an alternative process flow for the fabrication of the mold.

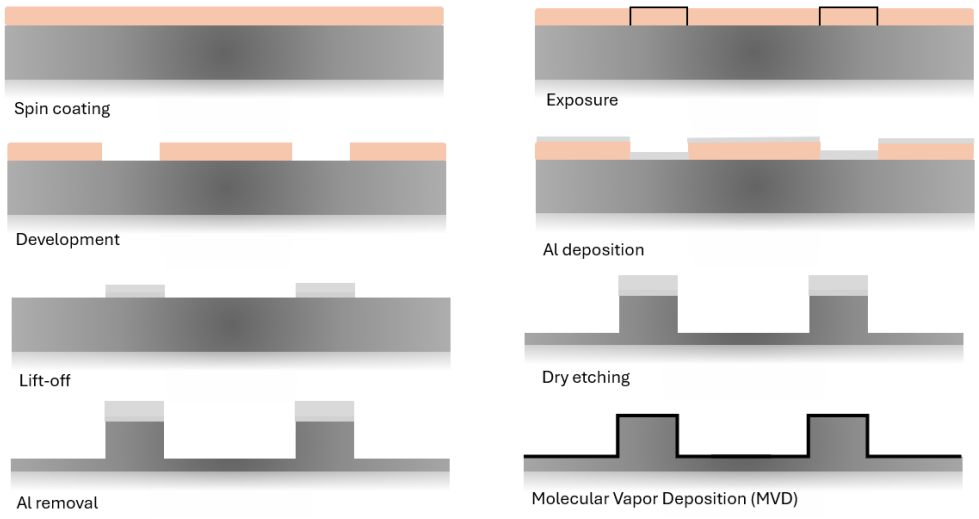

Figure 4.6: Graphical illustrations of the fabrication steps described in the mold's alternative process flow

4.2 Methods

As shown in the two proposed process flows, the cleanroom work involved several fabrication techniques. Before presenting the technical details and the results obtained, a brief theoretical overview of the working principles of these techniques is provided below.

4.2.1 UV-Photolithography

Photolithography is a microfabrication method used to pattern structures up to nanoscale on a substrate. With the aid of UV light, photolithography can transfer specific geometric features to a photosensitive polymer known as a photoresist, inducing chemical changes that allow it to cross-link or be removed later on [47].

The process begins by applying a thin layer of photoresist to the substrate, typically using a technique called *spin coating*. The wafer is spun at high speeds while the liquid photoresist is dispensed onto its center, spreading it across the surface. The wafer is then soft baked in order to evaporate the solvent.

A lithographic mask is then used to transfer the pattern after exposure to a light source. This can be a physical mask, often made of glass and chromium, or digital, if the lithography machine can acquire pattern information from a software. The light source, as well as the exposure parameters such as dose and defocus, are selected depending on the resolution desired for the pattern. UV light can give resolution below 1 µm , but there exist methods which exploit the Deep Ultra Violet (DUV) and the Extreme Ultra Violet (EUV) range which are the the cutting edge for advanced microchips, achieving resolution of tens of nanometers.

Depending on the type of photoresist used (positive or negative), the exposed or unexposed regions become soluble and are removed during development, where the wafer is immersed in a pool containing a developer solution -often Tetramethylammonium Hydroxide (TMAH)-, leaving on the substrate the patterned resist.

4.2.2 Metal deposition: E-beam evaporation

Electron beam evaporation is a Physical Vapor Deposition (PVD) technique used for depositing metals in form of thin films. In this method, an electron beam is directed onto a metal target, called source material, causing it to vaporize. The vaporized atoms then travel in vacuum and condense on top of the surface of the substrate, forming the thin layer with a programmed deposition rate.

An electron beam evaporator includes an high-vacuum chamber, where the wafers are placed, a crucible, which holds the source material and an electron gun that generates and focuses the beam vaporizing the target.

E-beam evaporation is often chosen because it provides control over the thickness, achieving

layers of few nanometers, and purity, thanks to the ultra high vacuum environment which reduces contamination.

4.2.3 Lift off

The lift-off process is a technique used to create metallic patterns on substrates. It is particularly useful when the metal to be patterned cannot be easily etched. In this process the substrate, entirely coated with metal, is immersed in a remover solution, where the resist layer patterned during lithography acts as a sacrificial layer and lifts off the metal that is on top of it. The final structure reveals the metal pattern that was deposited only on the regions without the resist.

It is important that the resist profile shows negative sidewalls or is sufficiently thick to ensure clean separation.

4.2.4 Dry etching

Dry etching is a technique that allows the removal of material by the use of reactive gases or plasma. Reactive Ion Etching (RIE), as opposed to wet etching, enables the formation of both isotropic and anisotropic structures, due to its high directionality, which is achieved through the presence of energetic ions. This technique allows the etching of high aspect-ratio trenches with vertical sidewalls. Moreover, the high tunability of process parameters, such as gas composition, pressure, RF power and etch time, provides precise control over the etching rate and profile.

The principle of operation relies on plasma generated by RF excitation of neutral gas species. Neutral radicals in the gas are responsible for isotropic etch and generate chemical reactions with the substrate, forming volatile byproducts. Meanwhile, the static electric field accelerates positively charged ions contained in the plasma towards the wafer surface. The combination of physical ion bombardment and chemical reactions enables efficient material removal and the formation of vertical profiles.

Bosch process

To obtain high aspect ratio trenches, the Deep Reactive Ion Etching (DRIE) technique is commonly employed. In particular, Bosch process is used, in which materials are cyclically etched, passivated and etched again, allowing for the formation of deep structures. This method involves the alternating use of different gases, one for etching (e.g. SF_6) and one for passivation (e.g., C_4F_8). Because SF_6 etches silicon isotropically, this alternating sequence results in scallops in the final structure's profile. The steps of this process are depicted in Figure 4.7

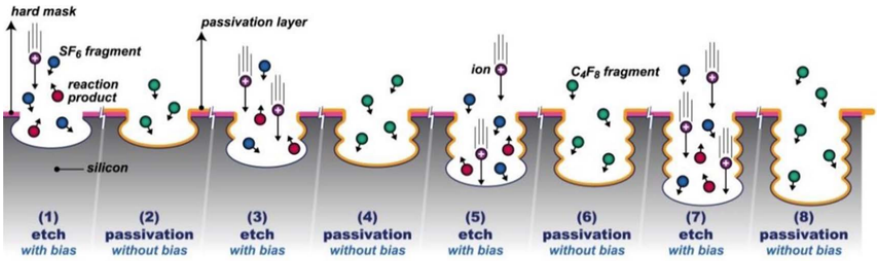

Figure 4.7: Conventional Bosch process steps for silicon etching. The first half-cycle is an ion-assisted isotropic etch step with SF6 plasma, then to minimize the lateral etching C_4F_8, a teflon-like polymer, passivates the structure. In the next step, the directional physical ion bombardment removes the polymer layer on the bottom and the etching is continued. The process is then repeated until the desired height is obtained [48]

4.2.5 Molecular Vapor Deposition

MVD is a process used to deposit ultra-thin conformal films, even on complex geometries. It consists of an hybrid coating with two different techniques, Atomic Layer Deposition (ALD) and Chemical Vapor Deposition (CVD), in combination.

This hybrid process uses multiple layers of ultra-thin coatings to build protective films across the substrate of the device. These serve a wide range of purposes such as antistiction coatings for easy de-molding.

4.2.6 Scanning Electron Microscopy (SEM)

Scanning electron microscopy (SEM) is an high-resolution technique employed to examine surface topography. In SEM, an electron beam with acceleration voltages of up to 30 kV is focused on the specimen. The interactions between the electron beam and the specimen emit signals collected by dedicated detectors and combined to form an image.

When the sample is radiated with an electron beam, elastic scattering results from the atomic nucleus or the outer shell electrons with similar energy. The incident electrons that are scattered without energy loss are the backscattered electrons (BSEs) and can provide both compositional and topographic information. When the incident electrons interact with electrons and atoms of the specimen, transfering energy, inelastic scattering occurs. This causes the excitation of the sample electrons and the release of secondary electrons (SEs), which can give accurate topographic information with good resolution. [49]

Since the wavelength of the electron beam is much smaller than that of visible light, the resolution of the electron microscope is much higher than that of an optical microscope. Moreover a SEM can magnify more than 10,000 times and ensure low contamination thanks to the the vacuum system in the instrument. [50]

4.3 Mask design

Before starting the lithography processes, common initial step in both process flows, a lithographic mask needed to be prepared. In the case of using a Maskless Aligner as the exposure tool, the mask is a digital file, rather than a physical photomask. This represents one of the key advantages of choosing a Maskless Aligner, as it allows for rapid and costless mask design, eliminating the waiting time and expenses associated with the fabrication of a physical masks. This is optimal in a prototyping context, such as the one required for this project, where the designs to be patterned could be changed several times.

The mask layout was designed using CleWin, a software fully compatible with all Maskless Aligner systems available in the cleanroom facility. A 4-inch wafer layout was selected, as it offers sufficient space to accommodate a good amount of chips and is compatible with all the equipment used in the process flow. Following this, the designs of the microfluidic channels and electrodes were created. These are illustrated in Figure 4.8

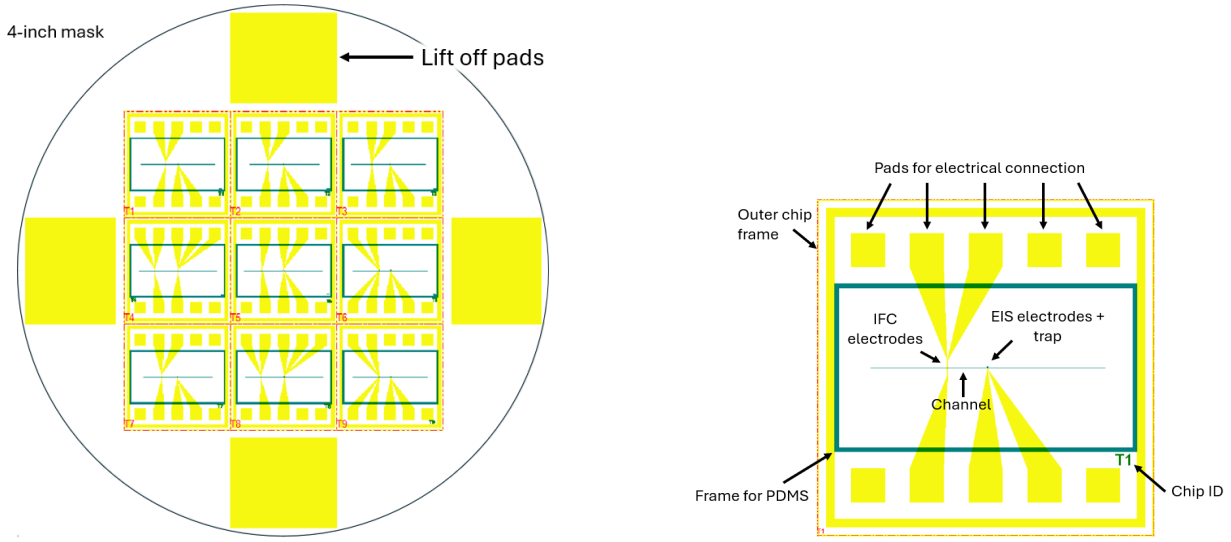

(a) Complete mask

(b) Single chip example

Figure 4.8: Overview of the lithography mask designed in CleWin. Yellow features are patterned with the electrodes process flow, blue features are patterned with mold process flow.

In figure 4.8a it can be notice a central region where nine chips are located. All the chips are squares of dimensions 2 cm × 2 cm. In the outer parts of the wafers, four wide squares were designed, these regions are meant to remain after the lift off process and help reducing the process time, as large unpatterned regions provide less access points for the remover to lift the resist. For this reason these are referred to as "lift off pads".

All chips present the same elements shown in Figure 4.8b, except for the electrodes and traps' shape that are different for each chip, in order to adapt to the proposed designs and test as

much configurations as possible. These are depicted in geometrical details in Appendix B.

Five pads of dimensions 2 cm × 2 cm were created in order to provide connection for both IFC and EIS electrodes in all the design.
The rectangular internal frame is used as a guideline for the subsequent cutting process of the PDMS, since the operation is executed manually and having a guideline helps with producing blocks of almost the same dimensions. It is patterned during the mold process, as it must also be replicated in the PDMS, and it is thick 250 µm to be seen clearly with naked eyes even in the transparent PDMS block.

4.4 Electrodes fabrication

The first step was the selection of the substrate. For this process 4-inch (100 mm) borosilicate glass wafers from were purchased by Siegert Wafer. Each wafer has a thickness of (500 ± 20) µm. Borosilicate glass provides high electrical insulation and transparency making it a good material for this project's application. After that, the fabrication processes were performed. In the following, each step is presented with technical information and outcomes.

- **Spin Coating**: During this step, a 1.5 µm layer of AZ5214E resist was deposited. AZ5214E is a positive resist that can also be used in image reversal mode, meaning it can switch from positive to negative tone after exposure if subjected to a *reversal bake* procedure. In the present process, it was used as a positive resist, although this is not the ideal choice for lift-off, in order to reduce the exposure time. Indeed, to expose a negative resist it is required a "dark field mask", where the mask design is inverted. As we can see in Figure 4.8a, if the yellow features were inverted the majority of the wafer area would be exposed, leading to a consistently slower process. The tool used for the spin coating is Süss MicroTec Gamma 2M spin coater

- **UV Lithography** Lithography was performed using Heidelberg instruments MLA100 Tabletop Maskless Aligner. This machine uses a laser light source of 365 nm. The dose used in this process is 110 mJ/cm^2 and the defocus is 0. Those parameters were chosen in accordance with the standard process proposed by DTU Nanolab staff.

- **Development**: The wafers were developed using 2.38% Tetramethylammonium Hydroxide (TMAH) AZ 726 MIF with the Süss MicroTec Gamma 2M developer. In this process, the TMAH solution is dispensed onto the surface of the wafer to form a puddle and left to act for 60 seconds - a technique known as "puddle development". After development, the wafer is rinsed and dried. Results from this step are showed in Figure 4.9

- **Metal Deposition** Metals for the electrodes were deposited with Temescal FC-2000 e-beam evaporator from Ferrotec. A 10 nm titanium layer was first deposited at a rate of 2 Å/s. Titanium is chosen as intermediate layer between glass and gold, because

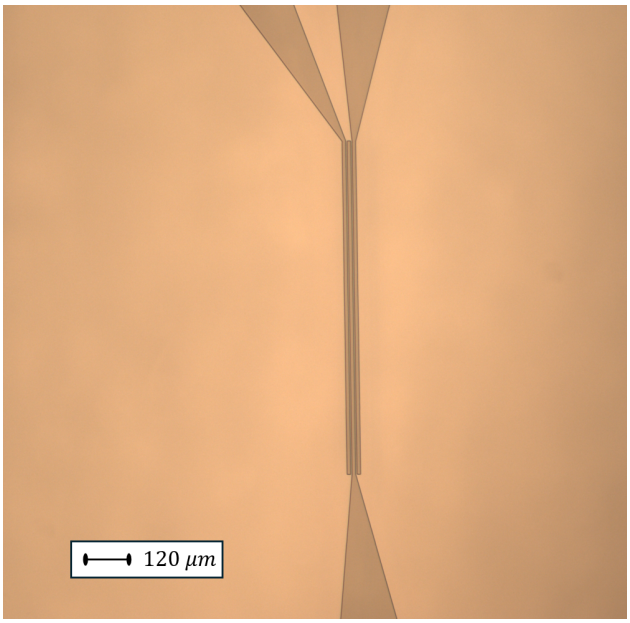

Figure 4.9: IFC electrode design after development in TMAH AZ 726 MIF. Image is taken with with optical microscope Nikon Eclipse L200N.

the latter shows optimal purity and electrical properties but poor adhesion to glass. The gold layer, thick 150 nm, is deposited with a deposition rate of 5 Å/s.

- **Lift off** During this process, the metal deposited on top of the resist still present in the wafer after development is removed, revealing the final electrodes pattern. Glass wafers are first immersed in Microposit™Remover 1165 bath, where they are left until all the resist carrying the metal is stripped. The process time is sped up with the use of ultrasounds and the overall duration is at least 25 minutes. After that, wafers are moved in an IPA bath to rinse Remover 1165, with ultrasounds activated for 5 minutes. Finally, wafers are rinsed in water and manually dried with a Nitrogen spray gun. Results after lift off are shown in Figure 4.10

- **Dicing Saw**: The fabrication process is concluded by cutting the wafer in order to obtain single chips. The instrument used is the DISCO, Automatic Dicing Saw, DAD 321. Here wafers are hold by a tape while a diamond blade cuts all the way through the glass. Final product is shown in Figure 4.11

4.5 Mold fabrication

To fabricate the mold for PDMS, it was selected a 4-inch Silicon wafer (Siegert Wafer), single side polished, with crystallographic orientation <100>. This choice is motivated by the high versatility of this substrate, together with its reduced cost, suitable for prototyping and testing.

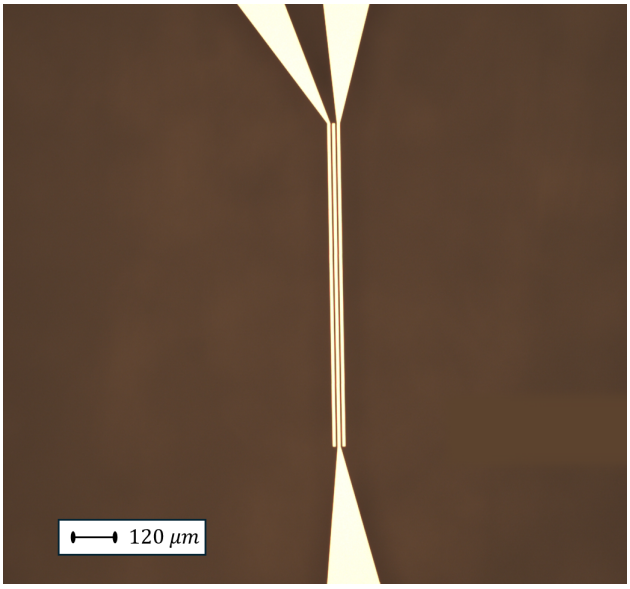

(a) IFC electrodes

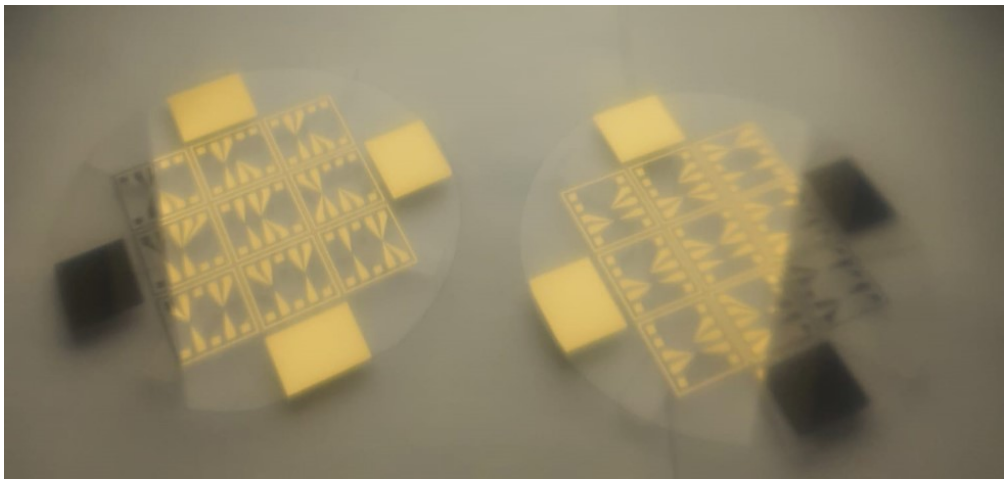

(b) Whole wafers

Figure 4.10: Gold pattern after lift off. a) Shows IFC electrodes observed with optical microscope Nikon Eclipse L200N. Features without resist of picture 4.9 are now coated with gold. b) Show wafers at the end of the process, with the gold pattern clearly visible.

Figure 4.11: Nine chips after dicing process.

Regarding the fabrication steps, two different approaches were proposed, as shown in Figures 4.3 4.5. The motivation that led to the creation of an alternative process flow is related to the dry etching technique that was initially chosen, which presented some complications and required the introduction of additional steps and the adjustment of parameters in other stages of the process.

Subsequently, a different dry etching recipe was tested. This new approach successfully addressed the limitations of the initial method, delivering improved results and allowing to define the final process flow.

In the next section, the optimization steps will be discussed in details.

4.5.1 Process optimization

Dry etching technique choice

After a lithographic process used to pattern the microfluidic channels, the dry etching technique was selected. This had to satisfy the following criteria:

- **Easily tunable height**, as a process that could etch 10 µm into the silicon wafer by fine-tuning the dry etching parameters was needed. Etching techniques characterized by excessively high etch rates were not suitable, as they offer limited control over precise depth targets.

- **Straight sidewalls**, as roughness on the sidewalls could improve adhesion to PDMS,

which represents a problem during the detachment from the mold. For this reason, DRIE techniques which presented large scallops were avoided.

- **Non damaging to features**, as the smallest structures, i.e. the channel restrictions within the traps, are more susceptible to non-ideal effects of dry etching techniques, such as ion bombardment or undercutting. Techniques involving the use of oxygen plasma, in addition to passivating and etching gases, were discouraged. The presence of oxygen in the plasma can partially oxidize or consume the exposed silicon surface, resulting in over-etching and loss of control over dimensions.

Examples of techniques that were tested are depicted in Figure 4.12.

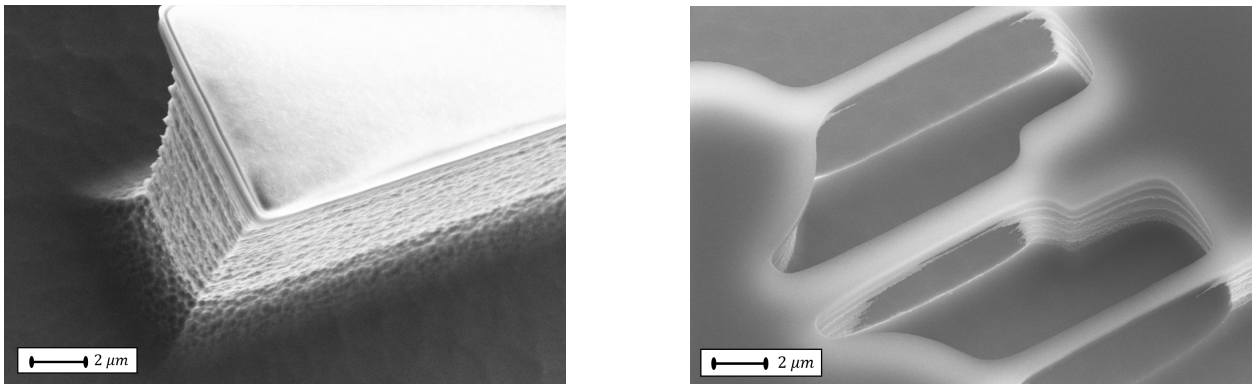

(a) Rough sidewall profile (b) Undercuts

Figure 4.12: SEM Zeiss Supra 40 VP (Supra 3) image of unwanted effects of dry etching recipes that have been discarded. a) Shows rough scallops and a under etch which ruins the vertical profile of the sidewall. b) Presents the situation at the traps, where the scallops are larger than the width of the channel therefore leaving a suspended layer of resist

The first recipe among the available options provided by DTU Nanolab which was considered a suitable candidate is "Nano142_gases". This is a continuos RIE process, meaning that the sidewalls do not show scallops. The etch rate is 400 nm/min, leading to a slow but highly controllable process. Details of this recipe are shown in Table 4.1

Table 4.1: Dry etch technical parameters of recipe Nano142_gases

Platen Power (W)	20
Flow rate SF_6	44
Flow rate C_4F_8	66
Coil Power (W)	1000
Temperature (°C)	-19
Chamber pressure (mTorr)	4

This recipe was initially tested etching the microstructure for a target height of 4 µm.

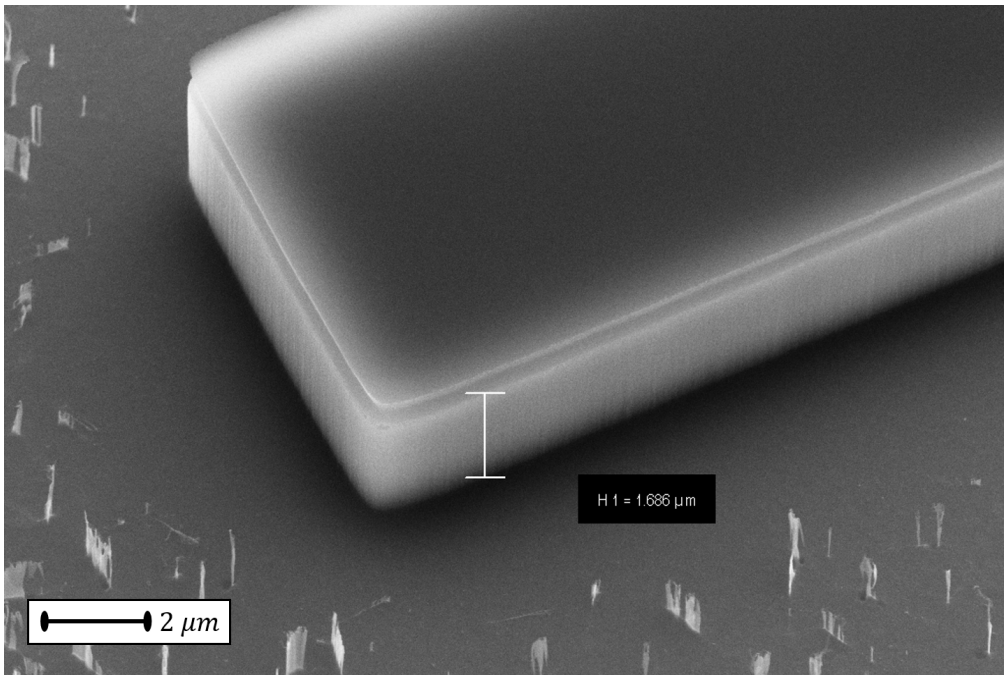

Figure 4.13: SEM (Supra 3) image of microstructure obtained after etching with recipe Nano142_gases. The wafer holder inside the SEM is tilted of 30° to appreciate the sidewall profile and measure height, which is computed as $h = 2H1$

From this initial experiment, presented in Figure 4.13, two disadvantages were noticed: the consumption of the photoresist and the formation of nanograss. Nanograss, also known as "black silicon", can form during dry etching, due to micro-masking caused by microscopic residues on the silicon surface. In particular, excessive passivation may not be completely removed during the etching step, leading to the formation of residual material that assumes the shape of a spike.

Al hard mask

To address the resist consumption, it was decided to use a thin layer of Aluminum as an hard mask, because it offers higher etch selectivity. The main drawback of this solution is the increased complexity of the process flow, as additional steps for metal deposition and lift-off are required. At this stage, the process flow becomes analogous to the one previously described for electrodes fabrication.

Dose-defocus test

The chosen resist was AZ 5214E, used again as a positive resist to shorten the exposure times. In this process, achieving high-resolution features is crucial, as the trap system can be effective if the critical dimensions are equal or smaller than 1 µm. Therefore, the exposure parameters for the chosen photoresist needed to be optimized.

To accomplish this, a dose-defocus test was performed. In this test, a set of test structures is patterned multiple times with a selected range of exposure doses and defocus. The goal is to identify the combination of values that yields the best resolution and pattern fidelity.

Heidelberg Instruments MLA150 WM I Maskless Aligner (MLA2) was selected as lithogrphy tool, because of the faster exposure times, useful in this stage where a lot of trials were done. This machine has a laser wavelength of 375 nm for which the standard values for dose and defocus associated to AZ5214E are 110 mJ/cm^2 and 0 respectively. The dose was swept among 80 mJ/cm^2 and 170 mJ/cm^2, with a step of 30 mJ/cm^2, and the defocus between -4 and 4 with a step of 2. Results were inspected with SEM (Supra 3) and depicted in Figure

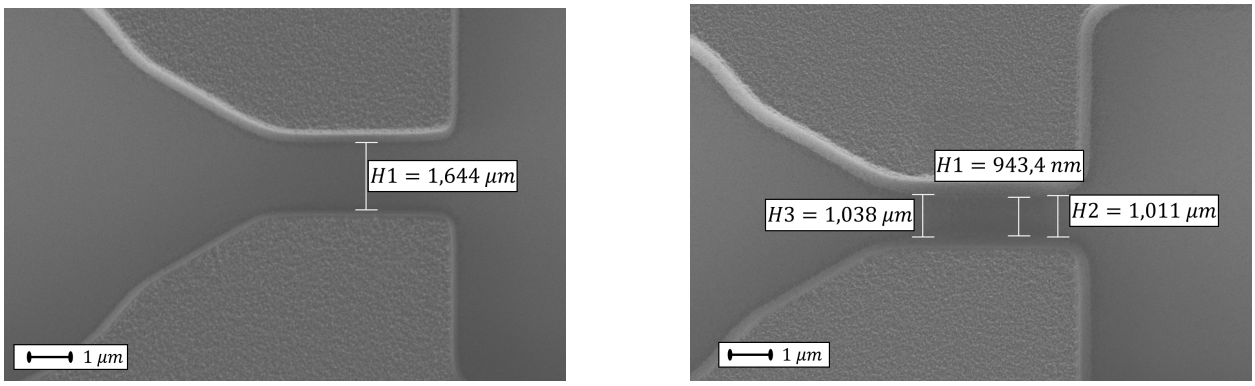

(a) Dose 140 mJ/cm^2 defocus 0

(b) Dose 80 mJ/cm^2 defocus 4

Figure 4.14: SEM (Supra 3) image of dose-defocus test results. Pictures shows the effects of a) overexposure and b) underesxposure

4.14. If a positive photoresist is underexposed, the exposed regions are less weakened by light, which can allow for the definition of narrower features. On the other hand, insufficient exposure may prevent the resist from being fully removed after development. Among the tested parameters, an exposure dose of 80 mJ/cm^2 and a defocus of 4 resulted in narrower sidewalls while still ensuring proper development of the resist.

Nanograss reduction

After resolving resist erosion by introducing the hard Al mask and optimising the lithography parameters, the structure was etched 10 µm. Wafers after process highlighted the presence of nanograss on the silicon surface. Nanograss constituted a later complication for the fabrication of the device, as it gets replicated in the PDMS block that is later bonded to the glass chip containing the electrodes. Due to the surface roughness induced by nanograss, the bonding process was inefficient, because PDSM was sealed too weakly and the fluid pressure was enough to detach the PDMS from the glass in every experiment.

To address this issue, the initial strategy was to tune the flow of SF_6 and C_4F_8 gases. In particular, it was hypothesized that increasing the amount of etching gas (SF_6) while

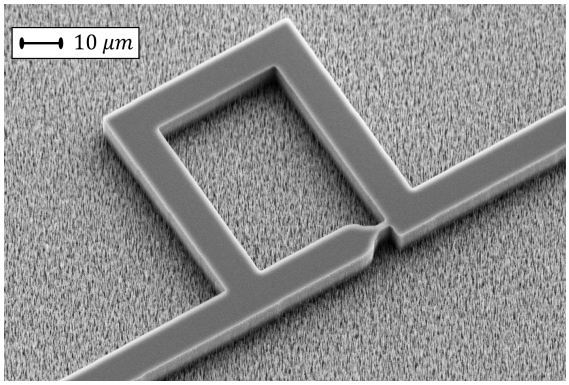

(a) SEM image of Si microstructure

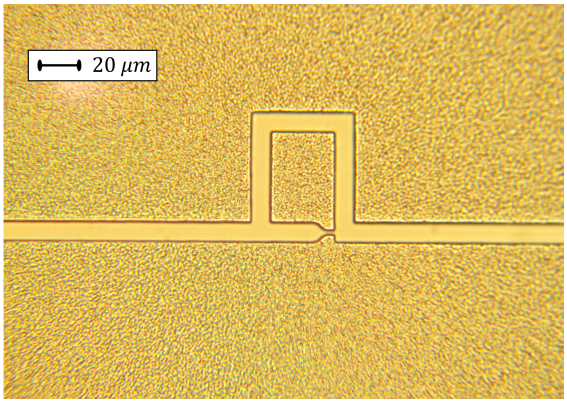

(b) Optical microscope image of PDMS

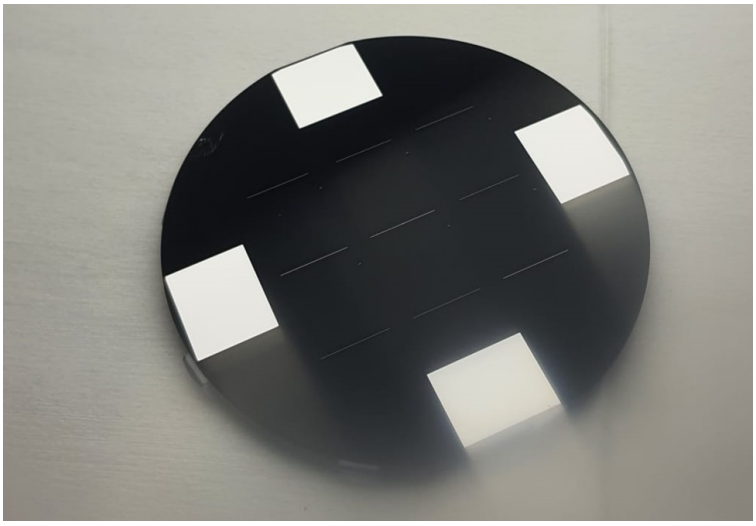

(c) Picture of wafer after etching

Figure 4.15: Visible effects of the presence of nanograss. a) shows a dense nanograss surrounding the channel structure, b) pattern replicated into PDMS, containing the nanograss, c) external appearence of the silicon wafer, characteristic black colour is given by the increased roughness

decreasing the passivating gas (C_4F_8) could help to reduce nanograss formation . This adjustment proved to be effective on small test samples (Figures 4.16), but inconclusive when applied to whole wafer.

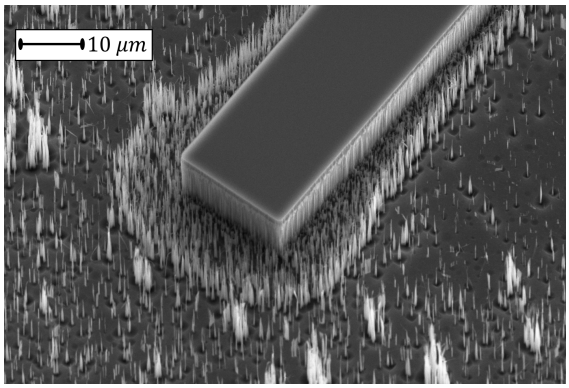

(a) Decreased C_4F_8 flow rate

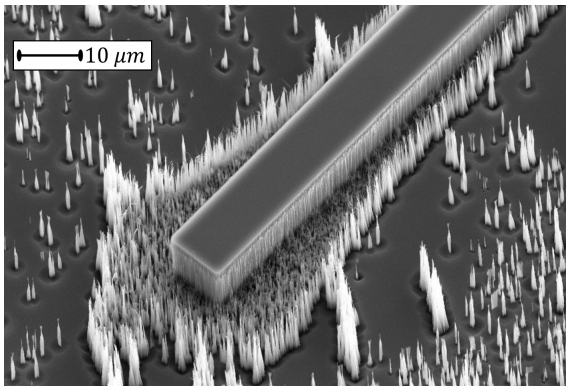

(b) Increased SF_8 flow rate

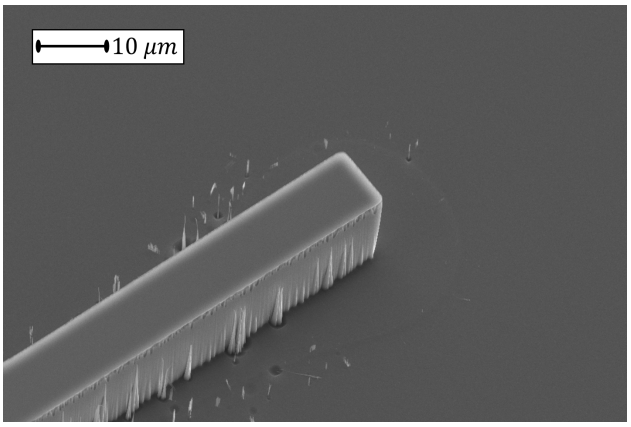

(c) Decreased C_4F_8 flow and increased SF_8 flow simultaneously

Figure 4.16: SEM (Supra 3) pictures of three methods utilized to reduce nanograss.a) C_4F_8 flow rate is set to 65 sccm, while SF_8 flow rate is fixed at 44 sccm, b)SF_8 flow rate is increased to 45 sccm, while C_4F_8 flow rate is kept 66 sccm, c)C_4F_8 flow rate 64 sccm, while SF_8 flow rate is at 46. This test were made on silicon wafer samples

The decisive contribution to the reduction of nanograss was finally achieved through the implementation of an additional isotropic etching step, meant to reduce the height of the silicon spikes. "Medium ISO 1" recipe was executed at the end of the Nano142_gasses process. Technical details are shown in table 4.2 As illustrated in Figure 4.17, this approach successfully reduced nanograss. However, the functionality of the device after the implementation of this method was never inspected, as in the meantime a different etching technique was tested, that improved drastically both the simplicity of the process and the outcomes.

Table 4.2: Dry etch technical parameters of recipe Medium ISO 1

Platen Power (W)	3
Flow rate SF_6	44
Flow rate C_4F_8	0
Coil Power (W)	600
Temperature (°C)	20
Chamber pressure (mTorr)	25

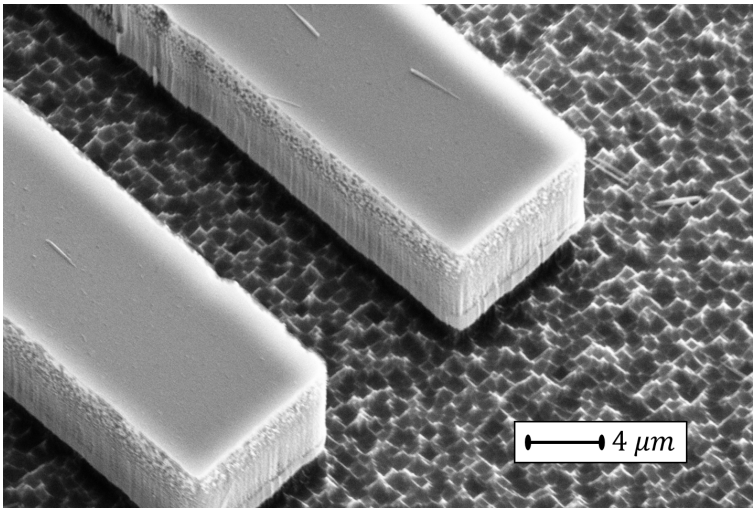

Figure 4.17: SEM image of Si strucures after the isotropic dry etch process. Features appears slightly damaged, but the nanograss is visibly reduced

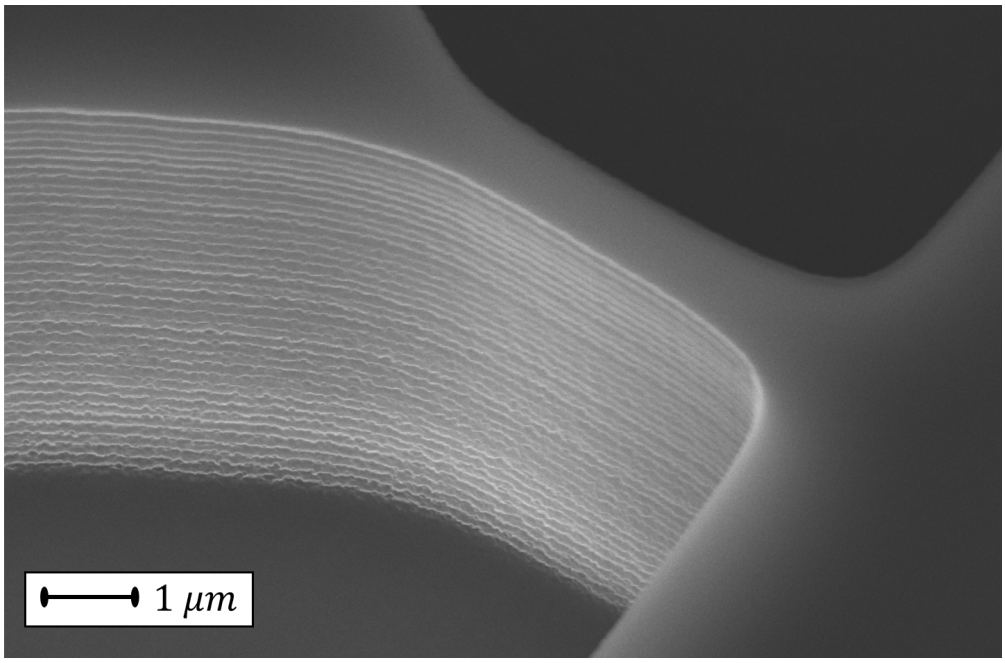

Figure 4.18: SEM image showing ultra-thin scallops on microstructure walls, obtained with "Process D4" dry etch recipe.

Process D4

"Process D4" is one of the standard recipes proposed by DTU Nanolab. It is based on the Bosch process and allows rapid etching while producing ultra-thin scallops (Figure 4.18). This method did not generate nanograss, allowing the desired structures to be etched with high precision while maintaining a smooth surface across the rest of the substrate. Technical parameters are shown in Table 4.3

Table 4.3: Dry etch technical parameters of recipe Process D4

	Deposition step	**Etch step**
Platen Power (W)	0	35
Flow rate SF_6	0	275
Flow rate C_4F_8	150	0
Flow rate O_2	0	5
Coil Power (W)	2000	2500
Temperature (°C)	20	20
Chamber pressure (mTorr)	20	26

Before the application of this technique the etch rate needed to be computed. Dektak XTA stylus profiler, was used to inspect the height of an etched test structure. Knowing the etch time, etch rate was computed following equation 4.1 and it was found to be ~5µm/min.

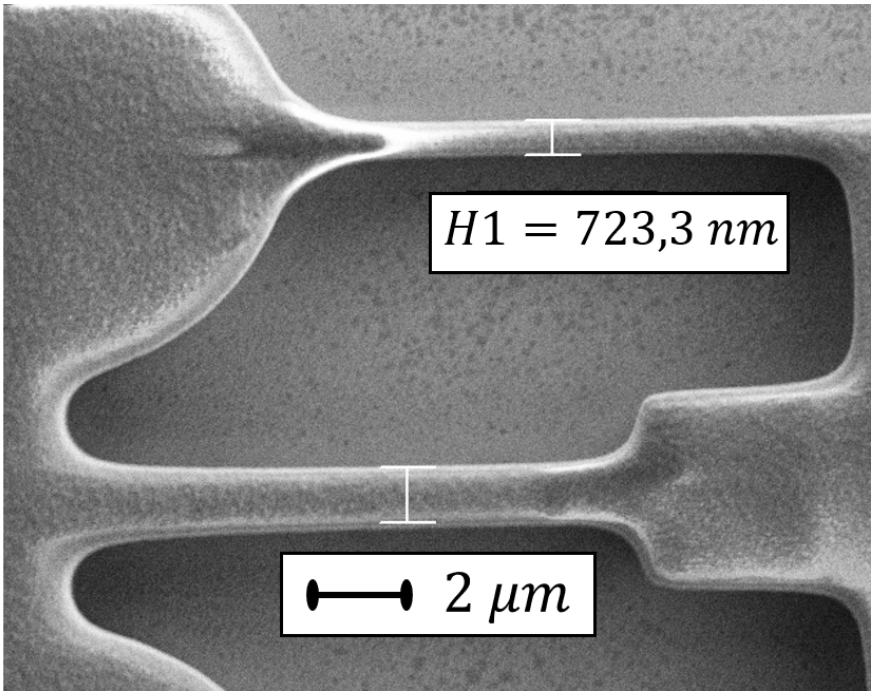

Figure 4.19: SEM image of a test structure after the lithography steps. The width obtained confirms that the choice of materials, tools and parameters can reach sub-micron resolution.

Results from the stylus profiler measurement are shown in Appendix A

$$Etch\ rate = \frac{Etched\ depth}{Etching\ time} \tag{4.1}$$

The enhanced selectivity to the resist of this technique made all the extra steps unnecessary, allowing to establish a final process flow, which is described in technical details in the next section.

4.5.2 Final process description

- **Spin Coating**: To begin the process, a 1.5 µm layer of AZnLOF2020 resist was deposited. AZnLOF2020 is a negative resist that shows high resolution and an optimal selectivity when used as mask for dry etching processes. The machine used for spin coating is Süss MicroTec Gamma 2M spin coater

- **UV Lithography** Lithography was performed using Heidelberg instruments MLA100 Tabletop Maskless Aligner. Despite being the slowest option, it was selected for its impressive results on the resolution, as can be noticed in Figure4.19. The exposure dose used in this process is 180 mJ/cm^2 and the defocus is 0. Those parameters were chosen in accordance with the standard procedures developed by DTU Nanolab staff.

- **Development**: For the development procedure, executed with Süss MicroTec Gamma 2M developer, it was first performed a Post Exposure Bake (PEB) at 120°C for 60 s. PEB is used to cross-link the exposed regions of the resist, making them insoluble. 2.38% TMAH AZ 726 MIF is then sprayed on silicon wafers and left for 60 s before drying.

- **Dry etching**: Advanced Deep Reactive Ion Etching (DRIE) Pegasus was used to perform dry etching. "Process D4" is selected among the list of recipes provided by DTU Nanolab. This process is run for 2 minutes, for a target height of 10 µm. Results after etching are shown in figure 4.20. After this procedure resist is stripped from the wafer surface with Oxygen Plasma .

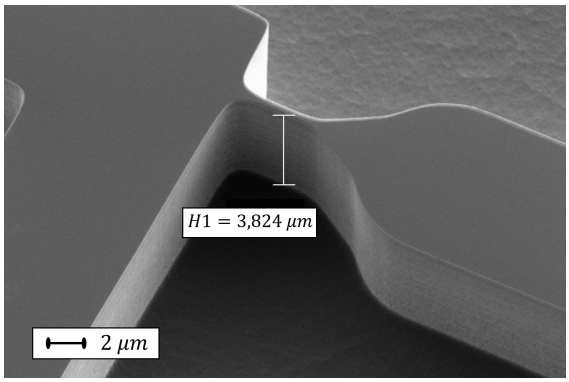

(a) Height of the structure

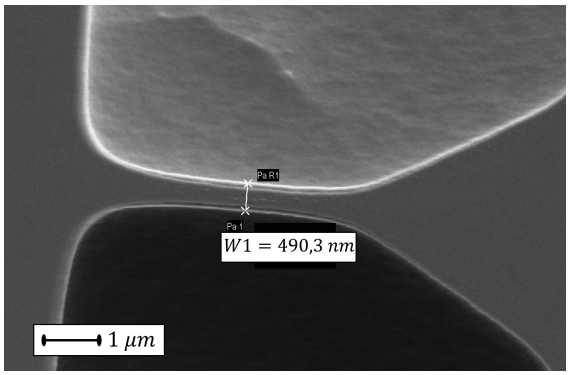

(b) Width of the trap's channel restriction.

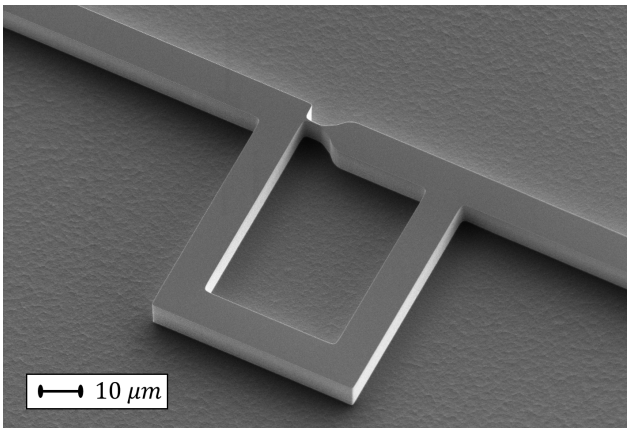

(c) Etched microstructure overview

Figure 4.20: SEM images illustrates different features of the silicon mold microstructure after etching with "Process D4". Picture a) was taken with the sample tilted 30°, total height is $2 \cdot H1 = 7.648$ µm. Picture b) shows an 490.3 nm width of the trap's channel restriction, overcoming the 1 µm goal. Picture c) presents the whole structure, where the smoothness of the background and the sharpness of the walls can be appreciated

- **Molecular Vapor Deposition**: During this step a 40 nm layer of FDTS (Perfluorodecyltrichlorosilane) is deposited on wafers surface. This thin polymer helps to avoid stiction of PDMS to the silicon structures. The process is performed on MVD 100 Molecular Vapor Deposition System.

4.6 Chapter summary

This chapter described the cleanroom processes for the fabrication of the electrodes and the silicon mold, to be used in the next steps that will finalize the device. The developed process flow for electrodes fabrication proved to be effective, achieving the desired outcomes without requiring additional optimization. In contrast, the mold fabrication process underwent several iterations before being optimized. With the dry etch recipe "*Nano142_142*" the onset of the nanograss was observed. Nanograss later on proved to be undesired in the PDMS to glass bonding and the fabrication process required modification, such as the use of and Al hard mask and the addition of a further isotropic etching. The selected dry etch recipe was eventually changed to "*Process D4*", that showed optimal pattern replication without the formation of nanograss or resist consumption. By combining a suitable selection of exposure parameters, it was possible to obtain features under the 1 µm resolution.

Chapter 5

Experimental Setup

After the microfabrication procedures, the device is assembled and tested in DTU Bioengineering facilities. Here, the chip is completed with the PDMS blocks containing the microchanels and then is connected to the electrical setup and the mechanical pump that pushes the samples inside the device. In this chapter the final experiment procedures are described in terms of materials and methods, in order to provide an overview of the device operation framework.

5.1 Device fabrication final steps

To obtain the complete device, the microfluidic channels must be combined with their corresponding electrodes, designed for IFC and EIS characterization. As previously mentioned, the microfluidic channel structure, fabricated on the silicon wafer, must first be replicated in PDMS and subsequently sealed to the glass chip. In addition to developing a PDMS preparation protocol and selecting a bonding technique, it was necessary to ensure proper alignment of the final device. In the following sections, these three steps are described, as they represent the final stages of the device's (macro)fabrication.

5.1.1 PDMS blocks

PDMS is an elastomeric polymer extensively used in biomedical applications as it offers several useful properties, such as biocompatiblity, transparency, chemical stability and resistance to degradation [51]. These, together with the simplicity of its preparation process and good adhesion to glass substrates are the characteristics that made PDMS the most suitable material for our project.

PDMS is obtained using SYLGARD 184 Silicone Elastomer kit, which contains a liquid polymer and a curing agent. These two precursors are mixed together in a defined proportion

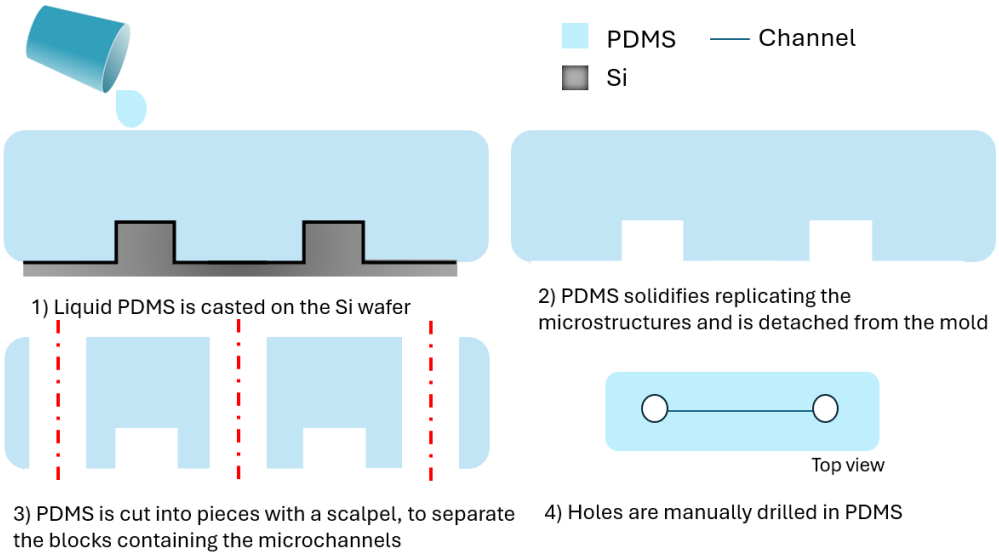

Figure 5.1: Simplified sketch of PDMS block fabrication with descriptions of the steps

which determines the final stiffness of the compound. The resulting liquid PDMS is then poured onto the entire silicon wafer and left to dessicate in order to release the air bubbles formed during mixing. Following that, the mixture is cured at high temperature to solidify. The protocol is described in details in Appendix C.

After this process, PDMS is detached carefully from the silicon mold and cut with a scalpel, following the visible guidelines patterned in the microfabrication process.

Subsequently, two holes for the tubings connection are punched at the extremities of the microfluidic channel. These have to cross the entire thickness of the block, to ensure that liquid containing the sample will reach and enter inside the channel. A sketch of these steps is depicted in Figure 5.1

5.1.2 Alignment

The alignment procedure is of critical importance for the proper functioning of the device. In order to achieve effective electrical characterization, it is essential that the microfluidic channel is precisely aligned to cross the underlying electrodes.

Concerning the IFC electrodes, alignment is relatively simple, first because the dimensions of the components involved are visible with naked eyes and second because it mainly requires ensuring that the channel crosses the electrodes perpendicularly. The electrodes design helps addressing this latter consideration, as their extended length provides a wide margin within which the channel can be positioned along the vertical axis.

In the case of EIS electrodes, not only the dimensions required the use of an optical micro-

scope to be seen, but the exact location of the electrodes with respect to the trapping site had an important effect on the signal detection. As demonstrated in Chapter 3, even slight misalignments can affect the accuracy and reliability of the measurements.

To deal with these challenges an alignment framework was designed and 3D printed by the colleague Sara Pittelli. The structure model and the final object are shown in Figure 5.2. This auxiliary tool is meant to be mounted on an optical microscope and keep the PDMS in a fixed position while the glass chip is moved by the stage of the microscope. The optical microscope is used in back focal mode and can show at the same time electrodes and PDMS block thanks to a custom made stage with an open slit. After the alignment position is found, the PDMS is carefully pushed down to touch the glass chip.

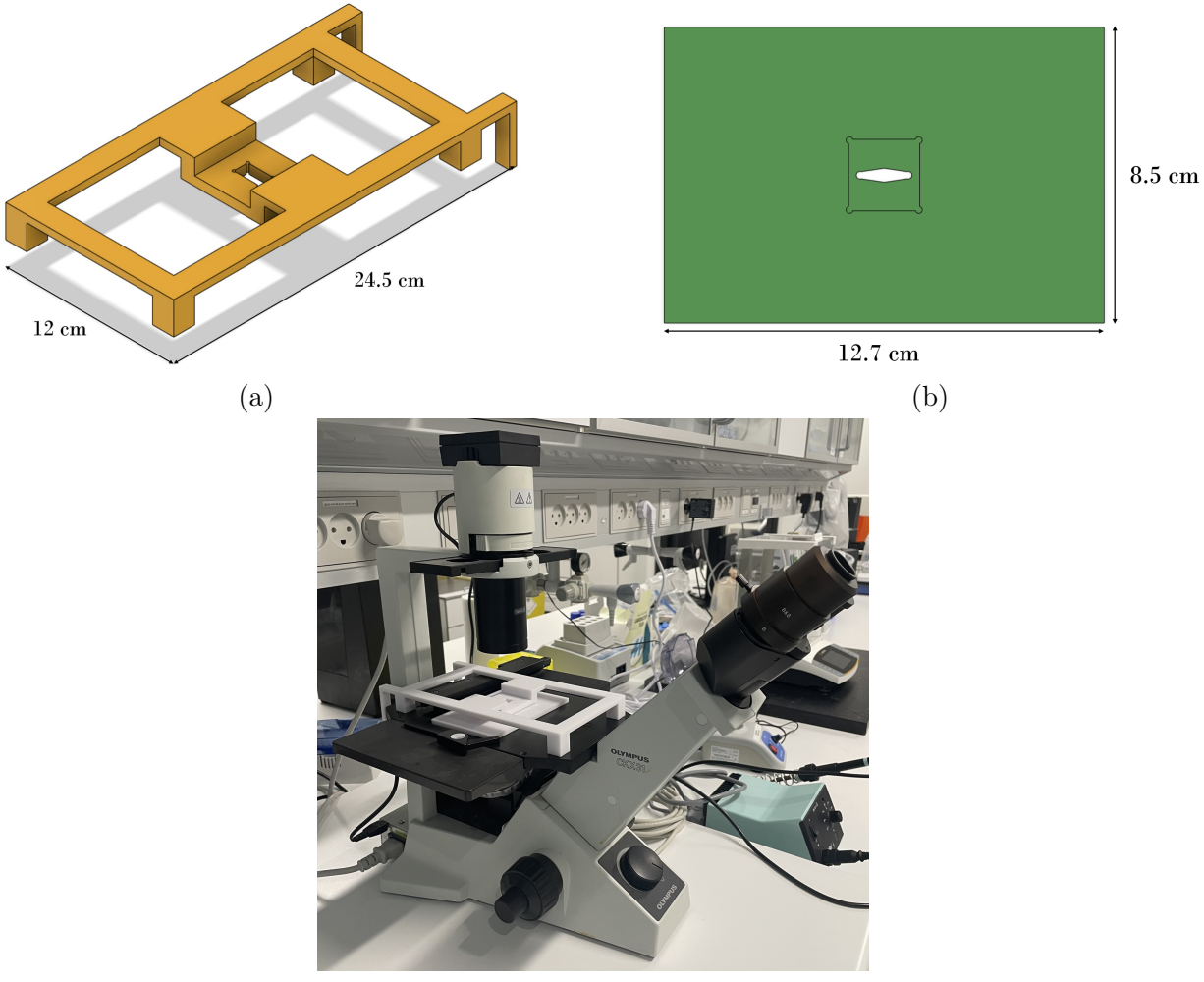

(a) (b)

(c)

Figure 5.2: Custom alignment setup showing a) the Autodesk Fusion model of the alignment frame, b) Autodesk Fusion the custom stage with the slit and c) the real tool obtained with 3D printing

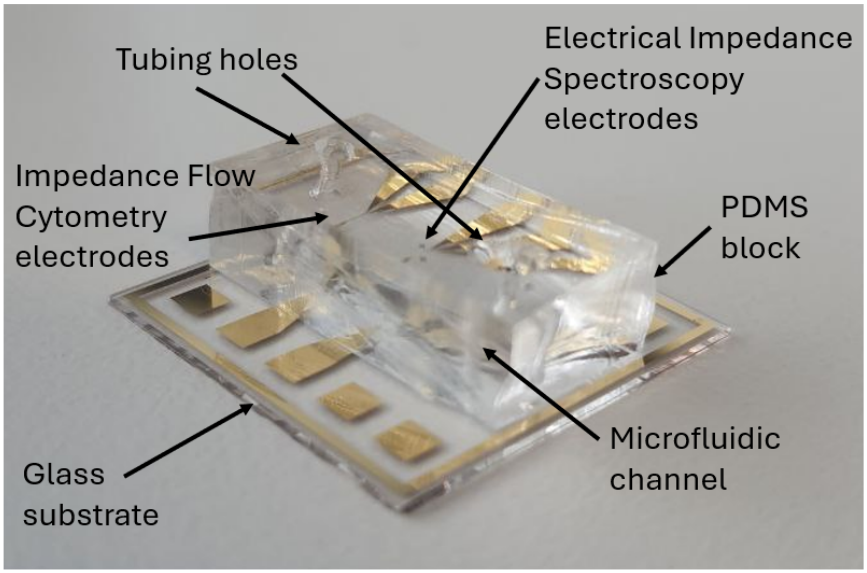

Figure 5.3: Picture of the final device

5.1.3 Device bonding

Bonding is necessary to seal the PDMS block to the glass chip, allowing fluid to flow through the channel without leakage. Since PDMS is a soft elastomer, it exhibits a certain degree of deformability, allowing it to adhere to the glass chip even under mechanical pressure. Based on this property, the initial bonding approach relied on an external frame designed to apply pressure on the external edges of the PDMS block. However, when the liquid was pumped during the experiment, the internal pressure generated by the fluid flow lifted the PDMS from the glass surface, resulting in leakage.

In order to obtain a stronger sealing it was decided to employ the oxygen plasma bonding. The surfaces of the objects to be bonded are placed in a chamber where vacuum is created. An RF signal is applied and plasma is ignited. Plasma has the effect of modifying the surfaces, activating some chemical species which can interact forming covalent bonds once the two object are put into contact. Therefore, after removing the components from the chamber, they are pressed against each other and annealead at 64° for 5 minutes, stabilizing the bond. 5.3 It is important to mention that surfaces have to be cleaned thoroughly before exposing them to the oxygen plasma to guarantee the effectiveness of the process. This is because dirt can disrupt the chemical activation of the surface or cause roughness. The latter is unwanted for the process as reduces the contact area of the surfaces, making the bond weaker. This is what happened when PDMS blocks were obtained from samples with nanograss, discussed in previous chapter.

One of the challenges of this process was to align efficiently but quickly enough the PDMS and the glass chip after functionalizing their surfaces with plasma bonding. This posed a compromise between effective sealing of the device and accuracy of the alignment, that was

often performed by naked eye.

A picture of the final device resulting from this process is presented in Figure 5.3.

5.2 Experiment description

Once the chip was correctly aligned and bonded, the device was ready for the experiment. In the following section, the components of the experimental setup will be presented and it will be explained how each was used in order to test the functionality of the device and acquire data.

5.2.1 Tools and instrumentation

In order to carry on the experiment, the following tools were used, all furnished by DTU Bioengineering lab:

- Optical microscope OLYMPUS CKX31
- Plastic tubing BOLA with inner diameter 0.8 mm and outer diameter 1.6 mm.
- Glass syringe (Hamilton GASTIGHT 1710) of volume 100 µL and plastic syringe KRUUSE of volume 1 ml.
- Needles 19G.
- Syringe pump HARVARD Apparatus PHD 2000.
- Impedance spectroscope HF2IS, Zurich Instruments.
- transimpedance current amplifier HF2TA, Zurich Instruments.

Moreover, a computer was used to collect pictures from microscopes and analyse data.

A picture showing the complete experimental setup is presented in Figure 5.4. In order to electrically connect the chip to the impedance spectroscope, it was necessary to design a holder and a printed circuit board (PCB). These components were designed by the colleague Sara Pittelli.

Chip Holder

The chip holder is fabricated by 3D printing in DTU Bioengineering lab. It presents a substrate where the chip is inserted and an upper part that encloses it, keeping it steady, but leaving room for tubings. The PCB was designed using the software KiCAD and ordered

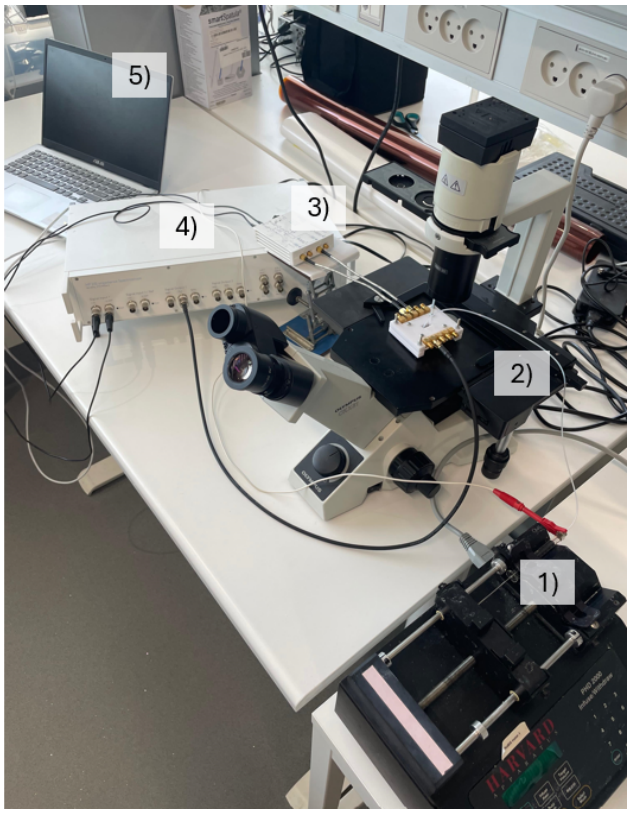

Figure 5.4: Picture describing the complete experimental setup: 1) syringe pump, 2) optical microscope, 3) the transimpedance amplifier, 4) impedance spectroscope, 5) computer for data analysis

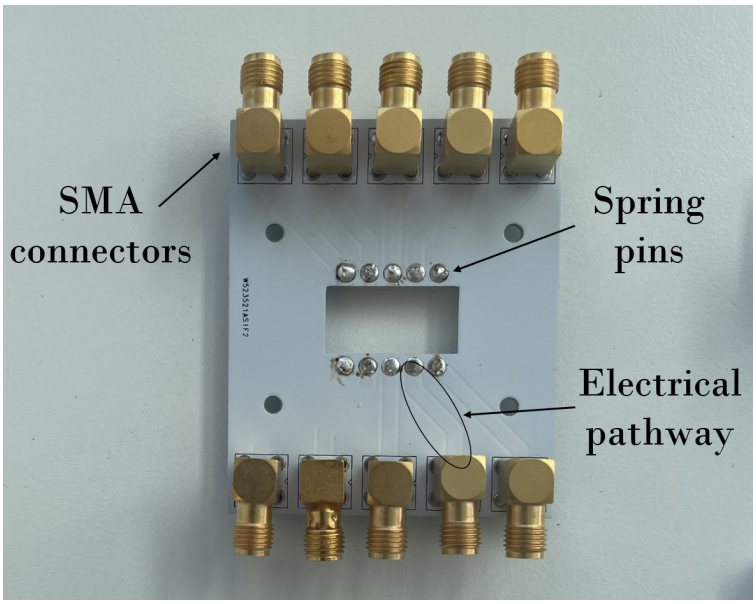

Figure 5.5: Printed circuit board where SMA connectors and spring pins have been soldered. The design includes circular holes for screws and a rectangular opening meant to accommodate the PDMS block

from the company PCBWay.
To furnish electrical connection to the specific design of our chips, five SMA (SubMiniature version A) connectors were soldered on two sides of the PCB to match the electric pads patterned on the chips, from which the electrodes for IFC and EIS start (Figure 5.5). The PCB is then mounted on the upper part of the holder with spring pins.

In the final configurations, the two parts of the holder are united together by screws, with the chip in between, as shown in Figure 5.6.

5.2.2 Methods

In order to begin the experiment, the following procedure is carried out:

- The chip is inserted into the holder and secured tightening the screws.
- The sample is drawn from a test tube using a syringe, to which one of the plastic tubes is attached right after. The tube is cut to a length sufficient to cover the distance from the syringe pump to the device.
- The syringe is mounted onto the syringe pump, which is then programmed with the syringe's internal diameter and desired flow rate (typically in the range of 0.01-1 µl/min).
- The holder containing the chip is positioned in the microscope, to allow the user to

(a) Bottom part of chip holder

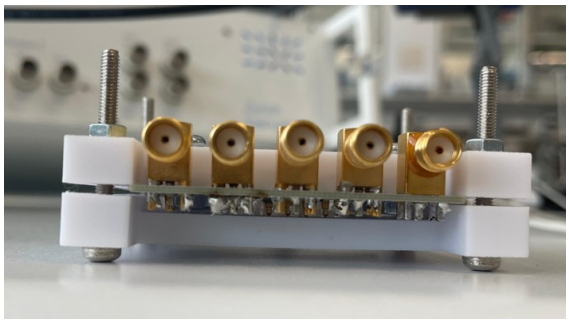

(b) Side view of closed chip holder

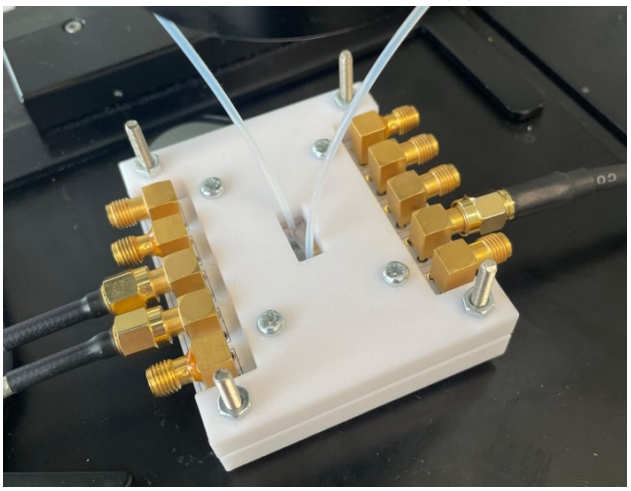

(c) Complete chip holder connected for the experiment

Figure 5.6: Chip holder assembling and resulting connection with the experimental setup.

check the progression of the experiment, then the inlet and outlet tubings are plugged in.

- The current amplifier is connected to the SMAs associated to the electrodes of the chip and a voltage is furnished from the impedance spectroscope.

- The experiment is started with the activation of the pump in infusion mode.

Two aspects to emphasize, before presenting the results, are the methods used to prepare the samples and to acquire measurements.

Samples preparation

Our experiments were conducted using polystyrene beads of various diameters and bacteria. The sample solution consisted of a mixture of Phosphate-Buffered Saline (PBS), used as the conductive medium and the selected analyte. PBS was employed both in its standard concentration and diluted 1:20 in Milli-Q water. The analyte concentration, was maintained at approximately $1 \cdot 10^6$ units/ml in both beads and bacteria case.

Beads are purchased from Polysciences Inc. Before using a sample containing beads it is necessary to mechanically agitate them, as they can clump risking to clog on the syringe needle before entering into the device.

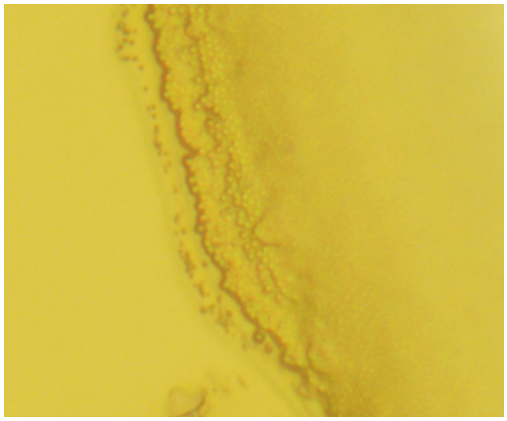

(a) 1 µm beads

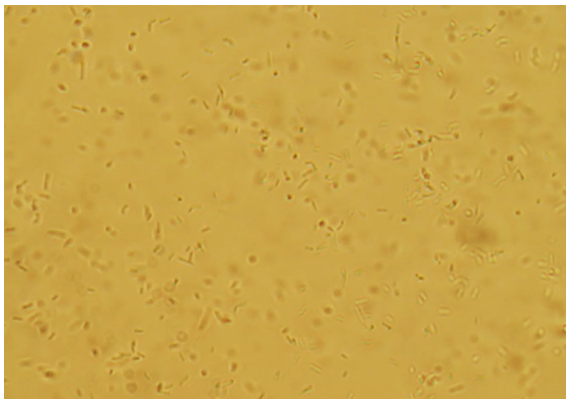

(b) Bacteria

Figure 5.7: Optical microscope picture of a droplet of sample containing a) 1 µm beads and b) bacteria *E.coli*. Beads are spherical while bacteria present a rod shape. Resolution is not optimal because of microscope limitation.

Bacteria (*E.Coli*) are grown by the researcher Beate Ramshøj Knudsen, member of NaBIS group in DTU Bioengineering. After being collected from the Petri dish, the bacteria are transferred into a nutrient solution known as "broth" and incubated for 24 hours before being diluted in a PBS solution.

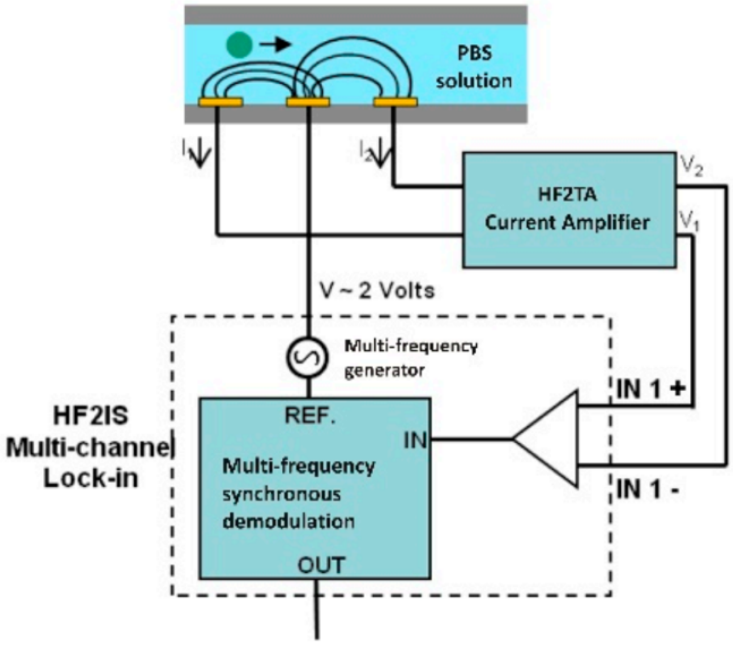

Figure 5.8: Schematic of the signal acquisition process using the transimpedance current amplifier HF2TA and the impedance spectroscope HF2IS. Picture is taken from [52]

Measurement acquisition

For reasons that will be explained better in the next chapter, we did not succeed in testing the EIS characterization, but we were able to measure signal from the IFC electrodes. The measurement setup for this analysis is illustrated in figure 5.8. The instruments involved in this process are the Impedance spectroscope HF21S and the trans impedance amplifier HF2CA by Zurich Instruments. An impedance spectroscope can generate signals and measure impedance over a range of frequencies. It incorporates components such as: a signal generator; a Digital to Analog Converter (DAC) and a Analog to Digital Converter (ADC), needed to furnish and read signals from the device; two differential measurement units; a lock-in amplifier and four demodulators used to enhance the SNR.

The advantage of using a lock-in amplifier relies in its ability to acquire signals at the same frequency of the input, suppressing noise and interference originating from the experimental setup and environment. This results in a signal with a high SNR.

Its operating principle is based on the combination of a mixer and a low-pass filter. When the output signal from the device reaches the lock-in amplifier, it is multiplied by a reference. The resulting signal is then passed through a low-pass filter, which removes high-frequency components. This extracted signal corresponds to the clean amplitude and phase information at the reference frequency, isolating it from noise.

The transimpedance amplifier converts the current to a voltage, which can be read by the

impedance spectroscope, and amplifies the signal.

During the experiment, a potential is applied to the excitation electrode and the currents measured on each of the two detection electrodes are subtracted to create the differential signal. The frequency used for the IFC characterization is 250 kHz following the standard of NaBIS research group, but the instrument can work simultaneously with eight different frequencies. That can be used to perform EIS.
The sampling rate is computed on the basis of the flow rate used in the experiment, from which considering the detection volume, the transition time of the particles can be extracted. Knowing the transition time, we decided to acquire 10 samples of the signal leading to a sampling rate of 833.33 samples/s.

Chapter 6

Experiment Results

During the final months of the project, efforts were focused on carrying on the experiment and testing the functionality of the device. Unfortunately, a series of events delayed the acquisition of results and finally only the IFC characterization could be performed.

Despite these challenges, it was possible to analyze the fluid flow within the microfluidic channels and observe the performance of the trapping structures, using both polystyrene beads and bacteria samples. The results do not provide a precise assessment of the system's behaviour, due to limitations in imaging resolution of instrumentation, but allow for a qualitative overview.

This chapter discusses the main complications encountered during testing and presents the experimental findings that were obtained.

6.1 Experiment issues and optimization

Several complications were found during the experiment. First, the functionality of some chips was compromised due to clogging of the microfluidic channels even before the particles containing fluid could be properly introduced. This problem can be associated to imperfections in the process used to create the tubing holes in the PDMS, which is made manually. In addition to that, contamination located on the chip during bonding or inside the tubing may have contributed to the obstruction. An example is depicted in Figure 6.1.

Another limitation was given by the microscope used in the experimental setup, which did not allow for magnification beyond a certain value. As a result, features below a specific size, -such as bacteria and some polystyrene beads- and even structural elements of the device as the trapping site (with dimensions on the order of 500 nm) were not clearly visible during experiment. This contributed to make real-time observation more difficult.

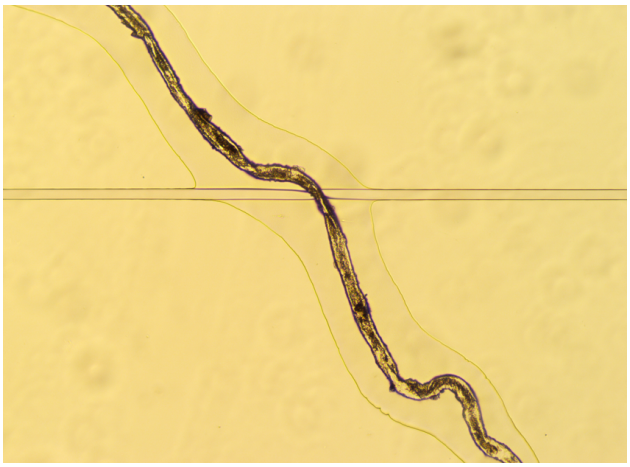

Figure 6.1: Optical microscope image showing channel integrity damaged by contamination.

In addition to these complications, which can be regarded as secondary, two other factors had a greater impact on the execution of the experiment: the alignment of the EIS electrodes with the trapping sites and the degradation of the electrodes.

6.1.1 Alignment of EIS electrodes

As explained in the previous section, a custom tool was 3D-printed to assist the alignment process. However, since during the procedure the PDMS layer is suspended a few millimeters above the surface of the glass chip, it was challenging to focus simultaneously the two components with the microscope. This complicates the alignment of the EIS electrodes with the microfluidic traps, especially considering that the microscope itself lacks the resolution necessary to clearly image the smaller features of the device. Additionally, since the PDMS is manually pressed onto the chip, there is no guarantee that the alignment remains precise once the final position is found.

To mitigate these challenges, simple alignment marks were introduced near the critical areas (Figure 6.2). These marks consist of a cross, patterned during the electrode fabrication process, and a square imprinted into the PDMS. The idea is that aligning these two larger and more easily visible symbols, also the finer features of the device can be properly aligned.

After the fabrication of the marks, three out of ten alignments gave optimal results, some examples can be seen in Figures 6.3. However, since this outcome was achieved during the final days scheduled for experimentation, it was not possible to proceed with the full-scan impedance spectroscopy test.

6.1.2 Electrodes damage

During the initial experiment attempts, it was observed that some electrodes presented visible damage, localized in regions near the microfluidic channel. This effect, illustrated in

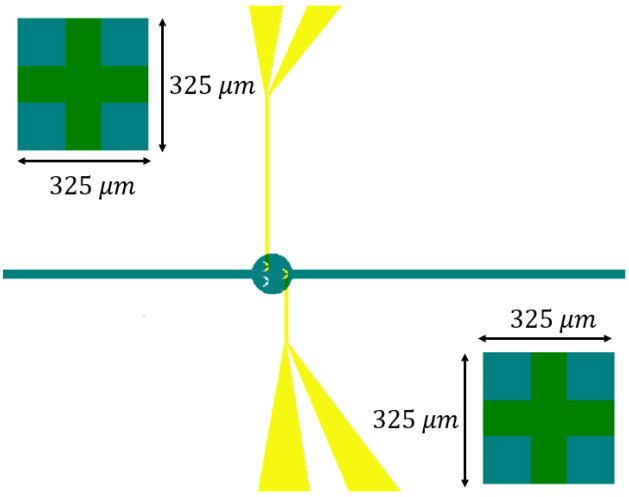

Figure 6.2: Lithography mask implementing alignment marks. Their dimensions and placement on the chip are based on the field of view of the optical microscope used for alignment, to ensure they are visible during the procedure

Figure 6.4, was found in every electrodes set that were connected to the electrical apparatus. The first approach to address the problem was to reduce the current flowing through the electrodes by lowering the voltage supplied by the impedance spectroscope. However, this method did not produce the desired results, and in subsequent experiments, the electrodes still showed signs of degradation.

For this reason, it was decided to test the impact of the conductive medium. PBS, initially employed at standard concentration, was diluted in Milli-Q water at 1:20 ratio, in order to decrease its conductivity. In addition to that, the sample was grounded by connecting the needle of the syringe, in contact with the fluid, with the grounding cable of the impedance spectroscope.

This problem was eventually solved allowing also to perform IFC characterizations, as shown in figure 6.5. However, the nature of this phenomenon is still not entirely clear and will be furthermore inspected in the next section.

6.2 Trapping tests

The behaviour of the fluid inside the traps was finally inspected. To optimize real-time visibility during the experiment, the AmScope microscope was employed, which presents better resolution. The chip was secured on the microscope stage using tape, without the 3D-printed holder, which was unnecessary for this type of analysis.

Not all available chips were suitable for the experiment, as in some cases traps appeared to be collapsed (Figure 6.6). In such situations, the proper functioning of the device is

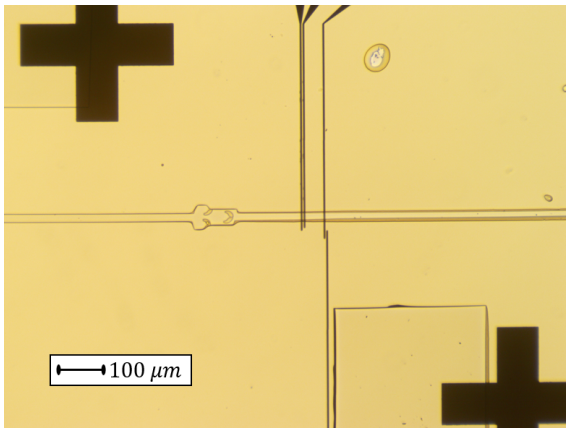

(a) Bad result

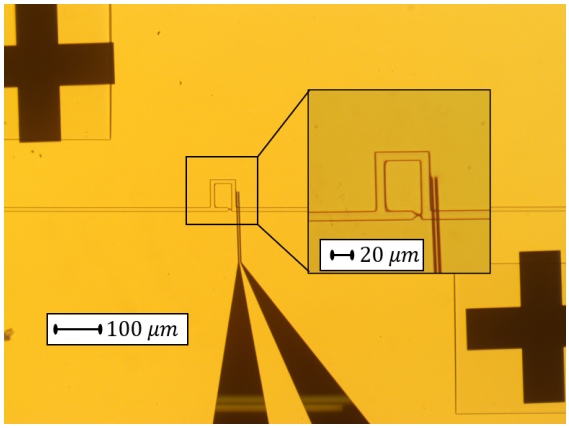

(b) Improved result

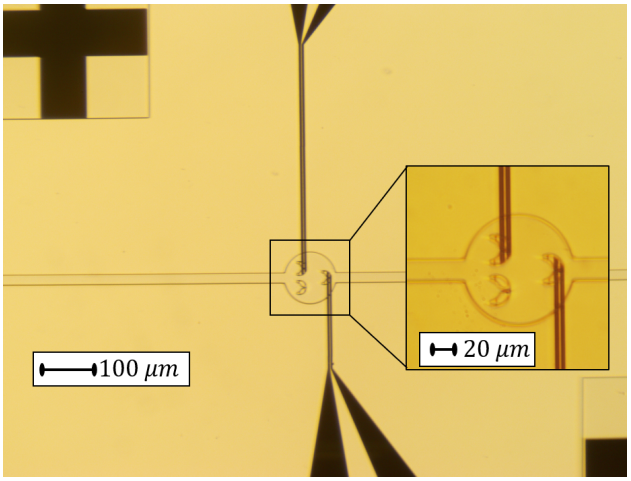

(c) Optimal result

Figure 6.3: Alignment results with the use of alignment marks

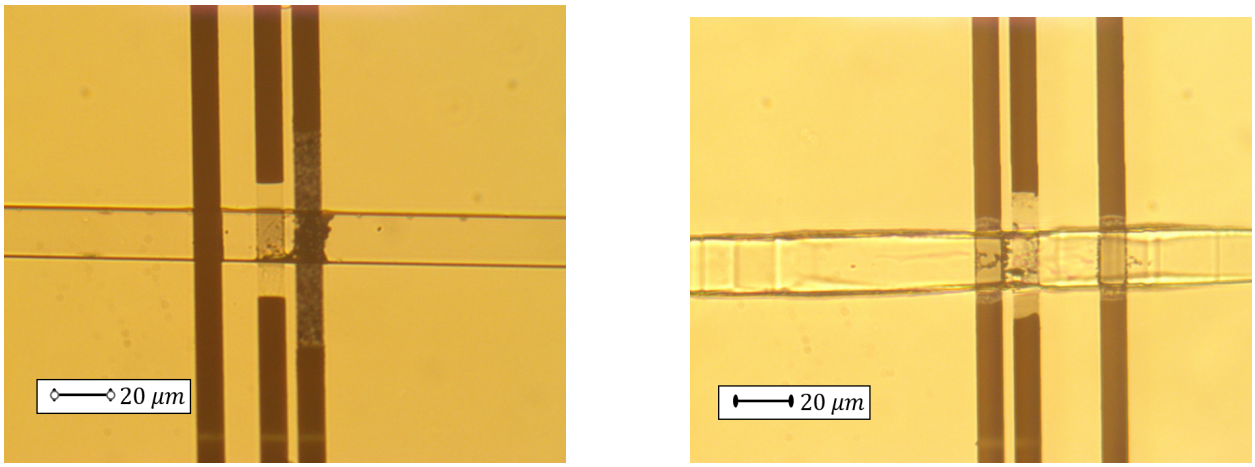

(a) Chip "E1" (b) Chip "T1"

Figure 6.4: Optical microscope images showing two examples of the observed electrodes degradation on different chips

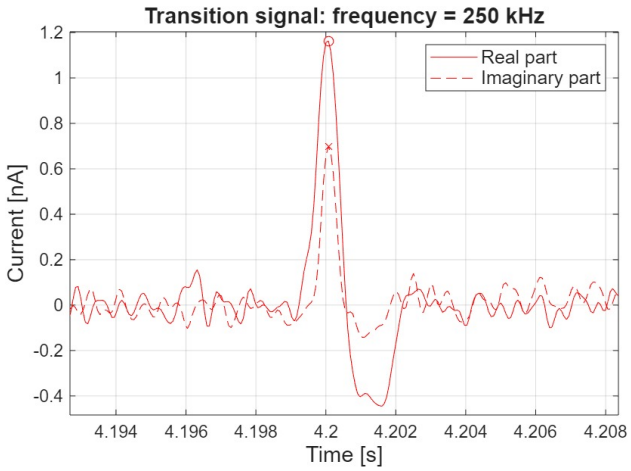

Figure 6.5: Signal recorded from an IFC characterization, showing the typical double-gaussian shape. A more detailed discussion of this result is object of the colleague Sara Pittelli's thesis

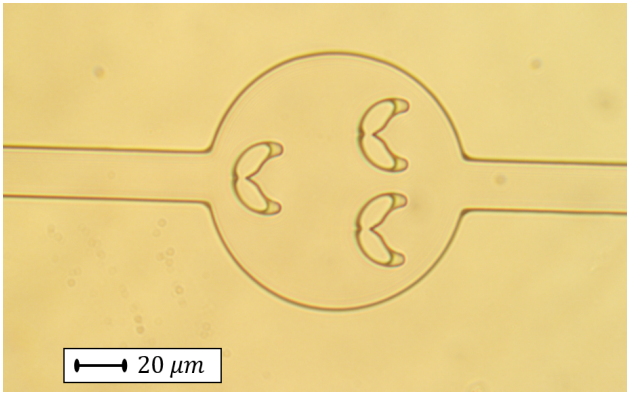

Figure 6.6: Optical microscope picture of the microfluidic channel containing traps.The channel restriction is not visible due to the pressure of the overlying PDMS, which compresses it and prevents fluid from passing through.

compromised and the resulting effects cannot be considered reliable.

For the chips that allowed to perform experiments, polystyrene beads with diameters of 1 µm as well as bacteria samples were selected. Flow rate in these tests was set to 10 µl/min.

6.2.1 Beads

Sample was composed of a mixture of 1:20 PBS and $1 \cdot 10^6$ units/ml polystyrene beads of 1 µm diameter. Experiment ran for 30 minutes and effects of the trapping are visible in Figure 6.7. The resolution of the image still does not allow to appreciate fine details, but two bead appeared to be trapped at the ending of the experiment. Despite of that, they were not in the beginning of the channel restriction, where they were expected to stop. This could be due to several reasons which will be better discussed in the next section.

From this experiment it was not possible to gain precise insights on the trapping mechanism, but in general the presence of only two beads in the trapping channel might be considered a positive result, suggesting that the functionality of single-bacterium trapping could potentially be achieved once the operational dynamics of the device are better understood.

6.2.2 Bacteria

Regarding the bacteria sample, a solution of $1 \cdot 10^6$ units/ml of *E. coli* in 1:20 PBS was used.

In this case, the trap used features a width of approximately 500 nm and a length of 7 µm.

At the end of the experiment, no trapped bacteria were noticed. A visual comparison of the trap before and after the experiment, lasted 90 minutes, did not reveal any significant changes. However, it is not possible to state that no actual trapping occurred. The limited

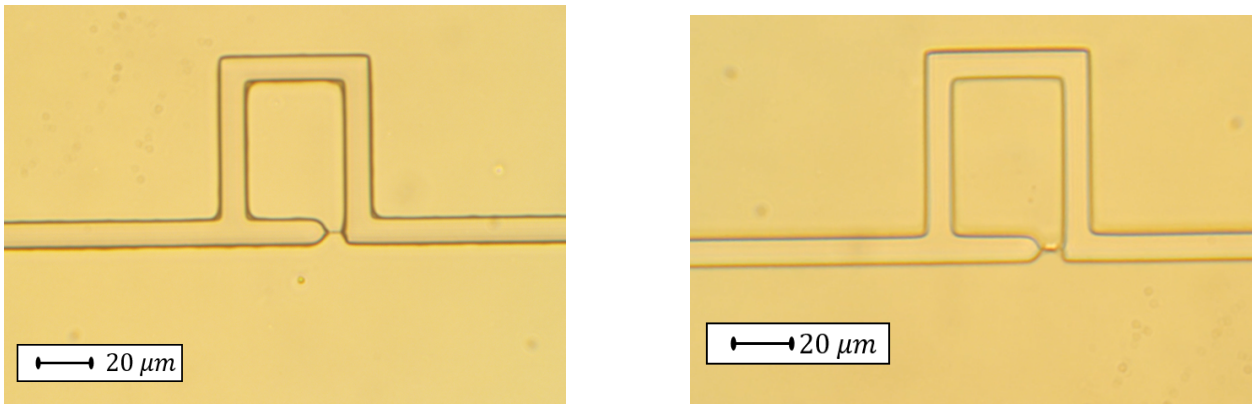

(a) No beads in trap

(b) 2 beads in the channel

Figure 6.7: Optical microscope images showing the trap situation before and after the experiment. a) is taken with the microscope camera at the beginning of the experiment b) is a screenshot of a video recording showing less resolution where the presence of beads can be noticed

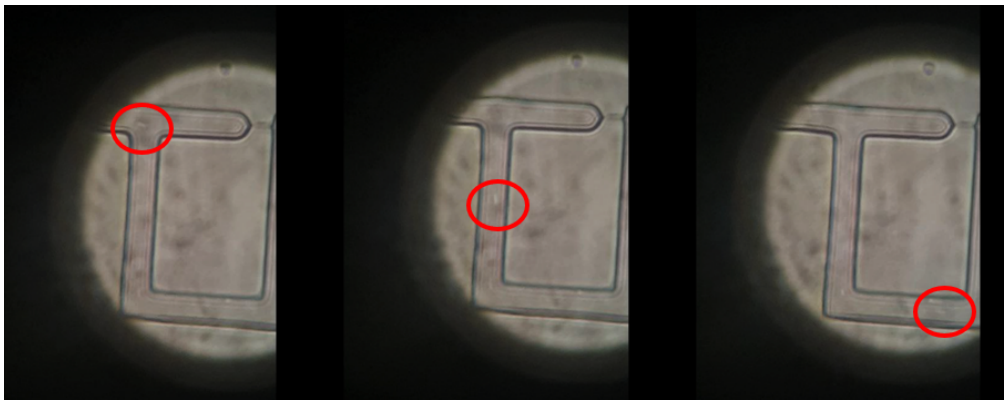

Figure 6.8: Screenshot of video recording showing the movement of the bacteria along the alternative path of the microfluidic channel.

image quality provided by the microscope camera used to record the experiment could have played a significant role by not showing the presence of small particles such as bacteria. Therefore, the lack of observable evidence may be attributed, at least in part, to technical limitations rather than the actual performance of the device.

However, the passage of bacteria continuing along the alternative channel was recorded, as shown in the Figures 6.8.

Chapter 7

Discussion

In this chapter, the previously presented results of the experiment will be analyzed, describing the challenges encountered during the execution and inspecting possible reasons behind the observed issues. Subsequently, suggestions to improve device performances will be proposed.

7.1 Analysis of the experiment results

7.1.1 Electrodes degradation

As described in Chapter6, Section 6.1.2, all the initial batch of electrodes used for the experiment underwent degradation.

A first qualitative observation is that this phenomenon looked particularly aggressive, because it was noticed after a few minutes from the beginning of the experiment and both Au and Ti seemed to be removed in the region underneath the channel.

Several hypotheses were considered to explain this behaviour. First, mechanical damage caused by fluid friction on the metals was excluded, as not every electrode in contact with fluid was degraded, but only those connected to the impedance spectroscope.

This suggested that the issue could have been related to the electrical behaviour of the device, supported by the observation that, in some cases, the central electrode, where the voltage is applied, began to degrade first. Based on this, the first strategy focused on reducing the input voltage. However, this approach did not yield any improvement and for this reason eventually the PBS was diluted and the liquid was grounded.

Based on the outcomes of the attempts, it remains reasonable to believe that the cause of this phenomenon is electrical. Nevertheless, since the PBS dilution and the grounding of

the fluid were implemented in the same experiment, a definitive identification of the decisive measure was not possible. Following the introduction of this solution, it was observed that, not only the electrodes stopped to degrade, but they could also withstand an higher voltage, which was proved to be crucial in enabling the detection of transitions during the IFC characterization.

7.1.2 Trapping experiment considerations

Traps collapsing

The first practical challenge encountered during the trap testing experiment was finding a chip suitable for performing the test, as many of the available ones exhibited collapsed traps. This may be related to the PDMS softness, which, while facilitating the bonding process, can also cause uneven deformation of design features. Such deformation depends on how well the geometry withstands the weight of the PDMS block and the pressure applied during manual bonding to the glass chip. Based on this, it is reasonable to think that some structures are more stable than other. However, more inspections should be done before establishing a correlation.

Beads position in the trap

By looking at Figure 6.7b it was observed that trapped beads were placed at the bottom of the trap microchannel. This phenomenon could be again attributed to the deformable nature of PDMS. Under mechanical stress, such as the pressure exerted by the push of the second bead, the PDMS structure can slightly deform, allowing the first bead to move and travel along the length of the channel.
In addition to that, the width of the restricted channel of the trap was not measured with high resolution techniques after it is imprinted on PDMS. Therefore it might be possible that the actual dimensions of the structures are larger then what was measured for the silicon mold, leading to a less efficient trapping.

To have a clearer overview of which mechanism is happening it would be required to do an accurate real time observation, to inspect the behaviour of the beads as soon as they approach the trap. This analysis is challenging not only because the extended duration of the experiment makes real-time observation difficult for a user, but also because recording a video of the experiment, with the current equipment, offers limited additional insights due to the low resolution and frame rate of the microscope camera used in the DTU Bioengineering laboratory.

Bacteria entrapment

During the experiment, it was not possible to establish whether the bacteria entrapment was successful or not. As already discussed, part of the uncertainty about the presence of bacteria inside the trap is due to the microscope's camera resolution and frame rate. An additional consideration is that the trap's channel dimension used in this experiment are:

w =∼500 nm, h =∼7.5 µm, L =∼7 µm. These dimensions give an hydraulic resistance of the trap equal to $R_{Hyd_{trap}} = 9.35 \cdot 10^{16}$ Pa · s/m^3, one order of magnitude higher than those computed in Chapter 3, contained in Table 3.2. This affects the flow reaching the trapping sites and might reduce it to a low amount such that no trapping events occur within the experiment's duration.

7.2 Device optimization ideas

7.2.1 Model and geometry improvements

Based on COMSOL simulations, in Chapter 3 it was possible to conclude that, given the current channel geometry, trapping a single particle is rather unlikely. To avoid this effect, an initial approach could be locally lowering the height of the trap channel. Depending on how much the channel is narrowed, this could allow space for only a single bacterium. This choice could be in principle effective in the entrapment, but presents some important limitations. First, in order to fabricate this kind of structure, double lithography and etching processes would be required. Moreover, shorter structure could be less able to withstand the PDMS bonding process and the internal fluid pressure, leading to a deterioration in the device performance such as the trap collapsing. In addition to that a further optimization of the design would be needed to avoid a too high hydraulic resistance.
Furthermore, considering that during experiments it was observed that few particles approached the traps, in order to characterize single bacteria a geometrical change in that sense could also be unnecessary.

Another idea for an improvement of the model is to calculate the arrival time of bacteria inside the trap, by studying their motion. This could help to have a more accurate understanding of their dynamics enhancing the predictability of the performance.

A geometrical modification that could potentially offer advantages involves widening the channel width near the inlet. This adjustment would facilitate the introduction of the sample into the device by allowing the liquid to be collected more effectively around the tubing hole, thereby mitigating the clogging issue.

7.2.2 Fabrication processes

Regarding the microfabrication process in the cleanroom, the obtained results were promising, as the optimization of parameters and techniques allowed us to achieve the desired design accuracy and resolution. However, if needed for a future application, the channel region of the trap could be further miniaturized using other fabrication methods such as electron beam lithography. As previously mentioned, this technique can reach nanometric resolutions, potentially extending the trapping function to microorganisms smaller than one micron. The main drawback is that this method is significantly slower, more complex and more expensive in terms of equipment.

On the other hand, the behaviour of PDMS suggests that it may not be the most suitable material for a reliable device. Its softness introduces instability in experimental outcomes, as traps may collapse during the bonding process. For this reason, less deformable polymers, such as SU-8, could be considered to improve the mechanical stability and overall reproducibility of the process. The disadvantage of choosing this material is that a completely new fabrication process where parameters and techniques should be tested and optimized again.

7.2.3 Experiment improvement

Some of the issues encountered during the experiment were related to contamination of the chip with debris. An aspect that could be considered for future work is performing the experiments in a contamination-controlled environment. A laminar flow hood or a glove box could decrease the presence of particles and dust in the device, but enhance significantly the total cost of the laboratory equipment.

Furthermore, we observed that the alignment procedure introduces a source of uncertainty on the correct device production and therefore needs to be improved. The alignment frame design could be optimized, reducing the distance between the PDMS and the glass chip, although, ideally, an automated procedure should be developed to make the process as accurate and reproducible as possible. A solution that would support this goal is to perform the alignment in a cleanroom. In this regard, the mentioned SU8, used in place of PDMS, could facilitate the implementation of such an approach.

7.3 Suggestions for future developments

Summarizing, the current stage of the project indicates that the device has not yet produced a sufficient amount of experimental data. This is undoubtedly due to several aspects that still require optimization, but it is to be remarked that the device was also not sufficiently tested . In the short term, the next steps could involve collecting more data from IFC characterizations, where the bacteria were not used, and performing EIS measurements on chips where optimal electrodes-trap alignment was achieved, in order to compare the experimental results with simulation outcomes.

For a longer-term development, a deeper investigation of the trapping mechanism itself could be pursued. Although hydrodynamic traps are relatively easy to implement, they may not represent the most effective approach for bacterial capture. Therefore, future developments of the device could explore the integration of alternative trapping techniques, such as vortex-based [46] or dielectrophoresis-based methods[53].

Chapter 8

Conclusion

This thesis purpose was to design and fabricate a microfluidic trap that allowed for full spectrum impedance scans of a single bacterium. In combination with the project of the fellow master student Sara Pittelli, it was aimed to obtain a device capable of characterize bacteria with techniques of impedance flow cytometry and electrical impedance spectroscopy. The starting point of the project was to design and simulate possible structures to implement an hydrodynamic trapping system. Subsequently a microfabrication process was developed to physically produce the components of the final device: glass chip containing the electrodes for the IFC and EIS characterization and a silicon mold to imprint and replicate the tested designs onto PDMS. In the final steps the device was obtained through demolding and plasma bonding and the experimental setup to test the electrical characterization and the trap functionalities was built.

The first goal of this project was to produce a microfluidic channel design that could potentially trap a single bacterium. Six different geometries were proposed, each of them presenting one or more trapping sites and an alternative path where the majority of the flow could be directed to prevent system's clogging. The length and width of the trapping feature were tuned to inspect the effects of the increasing hydraulic resistance, while keeping the height fixed at 10 µm, chosen in the first place to avoid stiction of the PDMS to the glass after bonding.
The simulations, performed on COMSOL and discussed in Chapter 2 explained the behaviour of the flow in relation to such changes and highlighted the challenges of the single bacterium trapping.
Successively, an electrical impedance spectroscopy characterization was simulated, where the effects of the channel dimensions along with position and properties of the particles were inspected as a proof of concept. Simulation showed that signal resulting from characterization when channel height was reduced was higher, as well as when particle occupied an optimal position in the channel, close to the electrodes and in the middle of their gap.

Subsequently, an effective microfabrication process flow for electrodes and silicon mold was established and presented in Chapter 4. For the electrodes fabrication, parameters and methods used led to the desired outcome without the need of further optimizations. Regarding the mold's process flow, detailed tests and improvements were required.

Among the inspected dry etching techniques, used to create the shape of the mold, it was initially chosen the continuous RIE recipe called "*Nano142_gases*". Despite showing appreciable vertical sidewalls, this recipe consumed the resist, used as mask, and created nanograss on the wafer. The former issue was dealt switching to an hard mask made of alluminium, that showed great performances. The latter phenomena was proven to be problematic during successive fabrication steps, which highlighted that the presence of nanograss prevented the correct sealing of the final components of the device. This moreover proved that roughness is an undesirable property for the adhesion of the PDMS block to the glass chip.

As a consequence, the process parameters were tuned but the results turned out to be inconclusive and the nanograss could be reduced only by the means of an additional isotropic etching.
Finally, the cyclic DRIE recipe called "*Process D4*" was found as the best option to etch the desired microstructures as it offered great pattern definition and the possibility to employ an simpler and efficient process flow, which led to obtain structures with sub micrometer resolution.

In the last steps of the project, the device was tested with an experimental setup that aimed to inspect the electrical characterization and the trap functionality. The impedance spectroscopy characterization of the device was prevented by difficulties in aligning the device components and the trapping capability was obstacled in some cases by the collapsing of the microstructures made of PDMS. This suggested the need for improvements on the macro fabrication techniques to enhance reproducibility.

The experiments conducted with polystyrene beads and *E. coli* bacteria, on the devices that presented traps in a good condition, provided partial insights into the functionality of the microfluidic trapping system. Polystyrene beads with a diameter of 1 µm showed signs of being trapped after 30 minutes of continuous flow. However, the observed trapping location was not at the expected point, suggesting secondary effects caused either by the deformability of the PDMS or the degradation of the device features after demolding.

In the case of *E. coli*, no clear trapping events were observed. This is attributed to a combination of factors, including the high hydraulic resistance of the chosen device, the size of the bacteria and the limited resolution and frame rate of the imaging equipment. Nonetheless, the bacteria were seen to flow through the bypass channel, indicating that the fluidic system was functioning.

Overall the device did not yield the aimed results in the five months time limit of this project, but it demonstrates potential that can be further inspected with more tests and improved

with optimizations in channel geometry combined with new fabrication techniques.

Acknowledgments

I would like to express my heartfelt gratitude to my supervisors for guiding me through this project. Your enthusiasm, immense competence and empathy constantly reminded me how grateful I am to have started this journey. I truly couldn't have asked for better and I will never forget this wonderful five months of growth, hard work, meaningful achievements and precious knowledge gained.

I would also like to thank the NaBIS group for making me feel like an integral part of the research team, giving me a wonderful first experience in a scientific environment.

A sincere thank you goes to my family and friends in Italy, especially to Niccolò, not only for teaching me everything I know about LaTeX, but most importantly, for always being there for me, even if just through a simple call, cheering me in every achievement and comforting me whenever I was feeling sad.

Last but definitely not least, I wish to thank Sara Pittelli, referred in this project as my "colleague", but to me, a dear friend with whom I shared every moment, both the highs and the lows, of this extraordinary experience.

List of Figures

List of Tables

Nomenclature

AC Alternating Current

ALD Atomic Layer Deposition

BSEs Backscattered Electrons

CFU Colony Forming Unity

CVD Chemical Vapor Deposition

DC Direct Current

DRIE Deep Reactive Ion Etching

DUV Deep Ultra Violet

ECM Equivalent Circuit Model

EIS Electrical Impedance Spectroscopy

EUV Extreme Ultra Violet

FDTS Perfluorodecyltrichlorosilane

IFC Impedence Flow Citometry

MLA Maskless Aligner

MVD Molecular Vapor Deposition

OHP Outer Helmoltz Plane

PBS Phosphate Buffer Saline

PCB Printed circuit board

PDMS Polydimethylsiloxane

PEB Post Exposure bake

PVD Physical Vapor Deposition

SCA Shallow Channel Approximation

SEM Scanning Electron Microscopy

SEs Secondary Electrons

SNR Signal to Noise Ratio

TMAH Tetramethylammonium Hydroxide

UV Ultra Violet

Appendix A

Further analysis and computations

A.1 Impact on signal of electrodes width

In the work conducted by colleague Sara Pittelli, significant research was carried out on the optimization of electrodes' design to improve the signal detection in IFC characterization. One of the aspects connecting her work to the project described in this thesis is the use of coplanar electrodes, which can lead to similar challenges in terms of signal reception.

In EIS characterization, only two electrodes are used and the measurement is performed when the particle is held at the center of the gap between them. Therefore, the signal is not obtained as the difference in impedance recorded by three separate electrodes, as performed in this IFC simulation. Nonetheless, in both cases, the electrodes geometry can play a crucial role in the intensity of the recorded signal. In one of the analyses conducted, the variation in current intensity was investigated as a function of the electrode width, showing how increasing the electrode surface area can influence the magnitude of the electrical signal.

In this simulation, carried on in COMSOL, the particle -modelled as a spherical bead of diameter 1 μm- was fixed between electrode 1 and 2, observable in Figure A.1, in the middle of the channel cross section, which has dimensions 10 μm × 10 μm.

Electrodes width was swept from 2.5 μm to 30 μm, while keeping the gap at 5 μm.

The results were fitted in the software Origin and can be seen in Figure A.2. As the electrode width increases, the signal becomes noisier, but higher, reaching its maximum around a width of 10 μm. After that the differential current (Idiff) begins to stabilize showing less sensitivity to further changes in width.

The conclusion of these simulation is that a reasonable width for coplanar elecrodes consid-

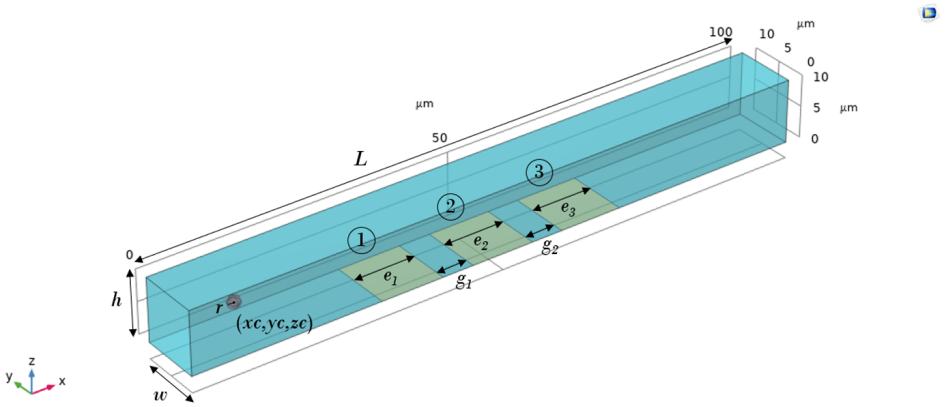

Figure A.1: COMSOL model used during simulations describing the geometrical asset and the components of the IFC characterization. This image belongs to Sara Pittelli

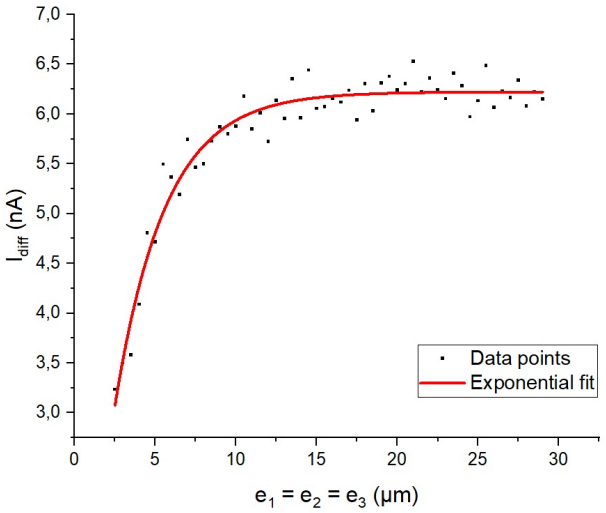

Figure A.2: I_{diff} as a function of electrodes width sweep.

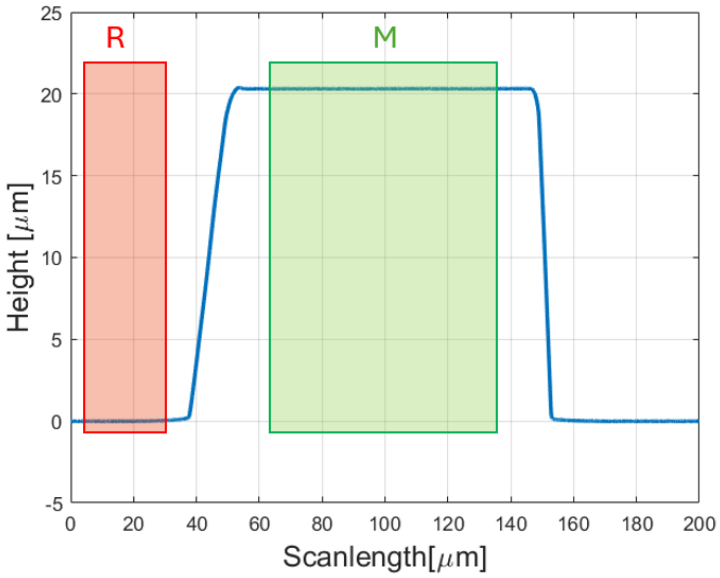

Figure A.3: Dektak XTA measurements on an etched feature. Measured height are displayed on the y- axis of this graph

ering the geometry of the channel and the particle size is 10 µm.

However this could not be implemented in our EIS electrodes, as the geometry did not allow for such dimensions. Moreover, because of the shape of the trap that changes locally in the cross section, different results for a similiar analysis could be expected. This would be an additional aspect to work for future implementations.

A.2 Etch rate computations

As explained in Section 4.5.1, before using the recipe "Process D4" to obtain the final structures, it was necessary to determine its etch rate. To achieve this, after performing a dry etching process with "*Process D4*" for 4 minutes, the feature height was measured using the Dektak XTA profilometer. The results of these measurements are shown in the graphs presented in FigureA.3. By the means of this instrument, features height is calculated by subtracting the height value corresponding to the red zone, labeled "R" (the reference), from the value corresponding to the green zone, labeled "M"

Using this results, the etch rate was computed as:

$$Etch\ rate = \frac{Etched\ depth}{Etching\ time} = \frac{20.3\ \mu m}{4\ min} = 5.075\ \mu m/min \tag{A.1}$$

Appendix B

Designs details

In this Appendix the designs used for traps and electrodes will be presented in geometrical details

B.1 Channel designs features

In the following images, the dimensions of remaining designs geometries will be presented. In each of them, the trap channel width is 1 µm.

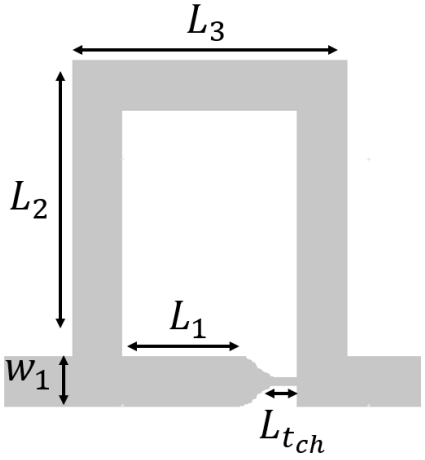

Figure B.1: *Design 2*

Table B.1: Dimensions of *Design 2*

Design 2				
w_1	L_1	L_2	L_3	$L_{t_{ch}}$
10 µm	25 µm	60 µm	56 µm	5µm

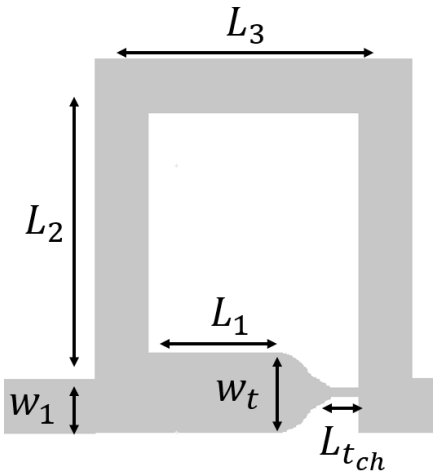

Figure B.2: *Design 3*

Table B.2: Dimensions of *Design 3*

Design 3					
w_1	L_1	L_2	L_3	w_t	$L_{t_{ch}}$
10 µm	25 µm	60 µm	56 µm	5µm	5µm

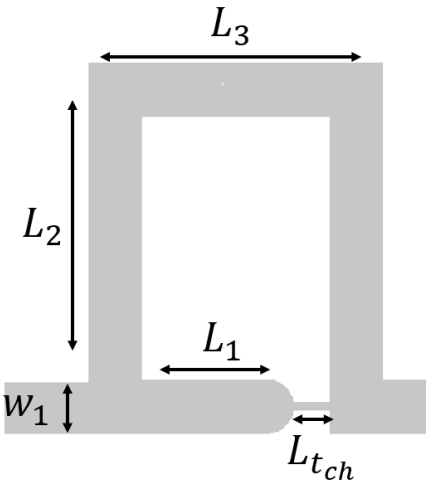

Figure B.3: *Design 4*

Table B.3: Dimensions of *Design 4*

Design 4				
w_1	L_1	L_2	L_3	$L_{t_{ch}}$
10 µm	25 µm	60 µm	56 µm	7µm

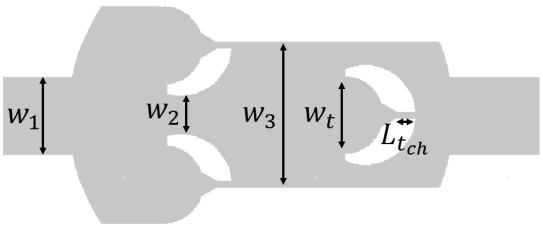

Figure B.4: *Design 5*

Table B.4: Dimensions of *Design 5*. w_t and $L_{t_{ch}}$ are equal in all the three traps

Design 5				
w_1	w_2	w_3	w_t	$L_{t_{ch}}$
20 µm	11 µm	37.5 µm	10 µm	3µm

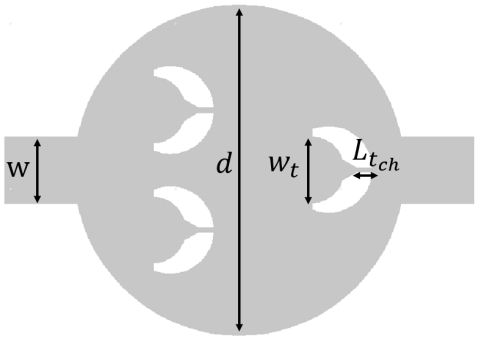

Figure B.5: *Design 6*

Table B.5: Dimensions of *Design 6*

Design 6			
w	d	w_t	$L_{t_{ch}}$
20 µm	100 µm	10 µm	5 µm

B.2 Chips features

As we discussed in Section4.3, the lithography mask includes nine chips. Each chip is labeled with the name "Tx," where x indicates its position on the mask, ordered from left to right and top to bottom. The resulting identifiers are therefore "T1," "T2," "T3," and so on. Among these, only the first six chips feature different electrode and microfluidic channel designs, while "T7," "T8," and "T9" replicate the layouts of "T2," "T4," and "T6," respectively. This choice was made to test the resolution achievable through the silicon mold fabrication process for the designs that appeared most interesting, by tuning in each run the width of the trap channel.

In the following Figures the design of the first six chips will be presented together with tables to show the dimensions of the electrodes and gaps for IFC and EIS

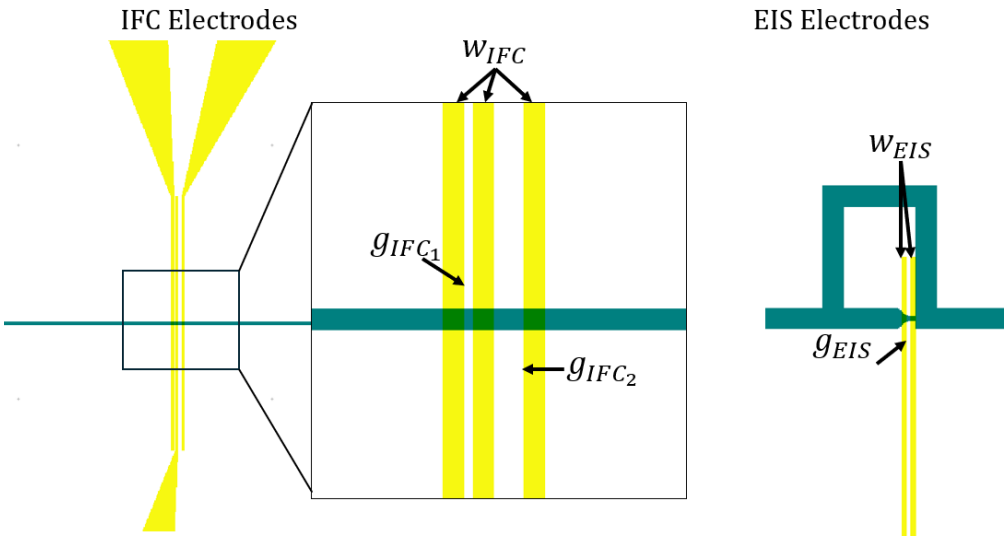

Figure B.6: Sketch of electrodes and channel features contained in chip "T1".

Table B.6: Table of electrodes dimensions for Chip "T1"

Chip "T1"

w_{IFC}	g_{IFC_1}	g_{IFC_2}	w_{EIS}	g_{EIS}
10 µm	5 µm	15 µm	2 µm	2.5 µm

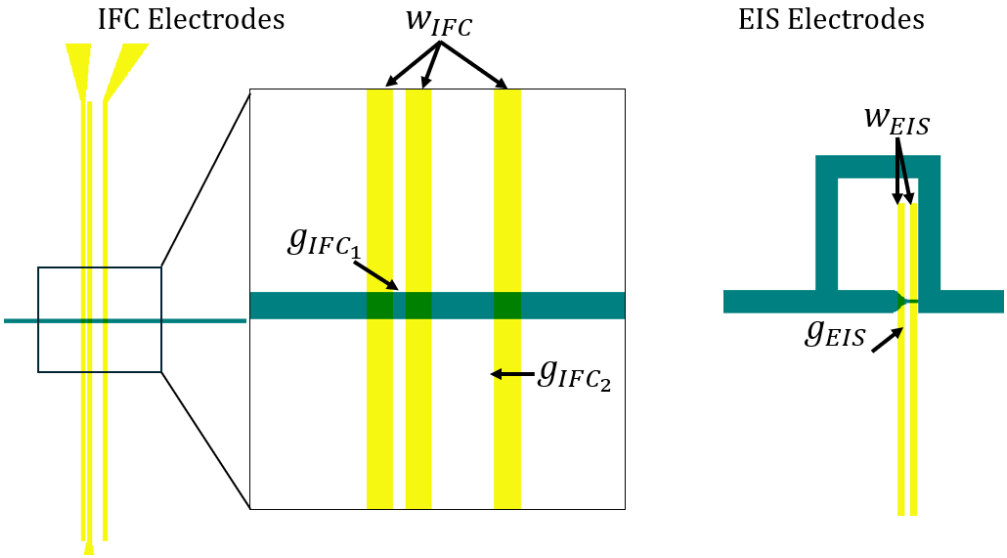

Figure B.7: Sketch of electrodes and channel features contained in chip "T2".

Table B.7: Table of electrodes dimensions for Chip "T2"

Chip "T2"

w_{IFC}	g_{IFC_1}	g_{IFC_2}	w_{EIS}	g_{EIS}
10 µm	5 µm	25 µm	3 µm	2.5 µm

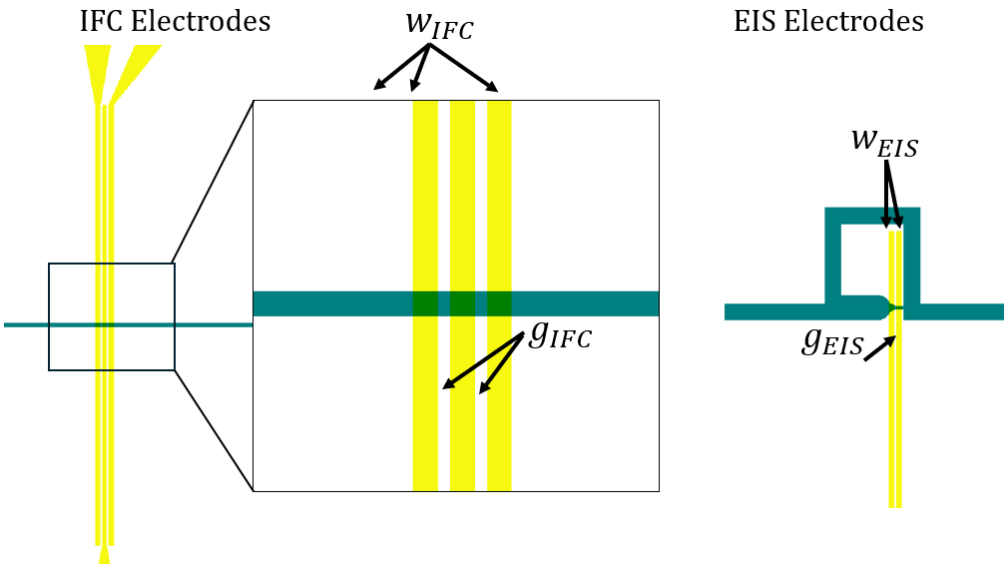

Figure B.8: Sketch of electrodes and channel features contained in chip "T3".

Table B.8: Table of electrodes dimensions for Chip "T3"

Chip "T3"			
w_{IFC}	g_{IFC}	w_{EIS}	g_{EIS}
10 µm	5 µm	3 µm	2 µm

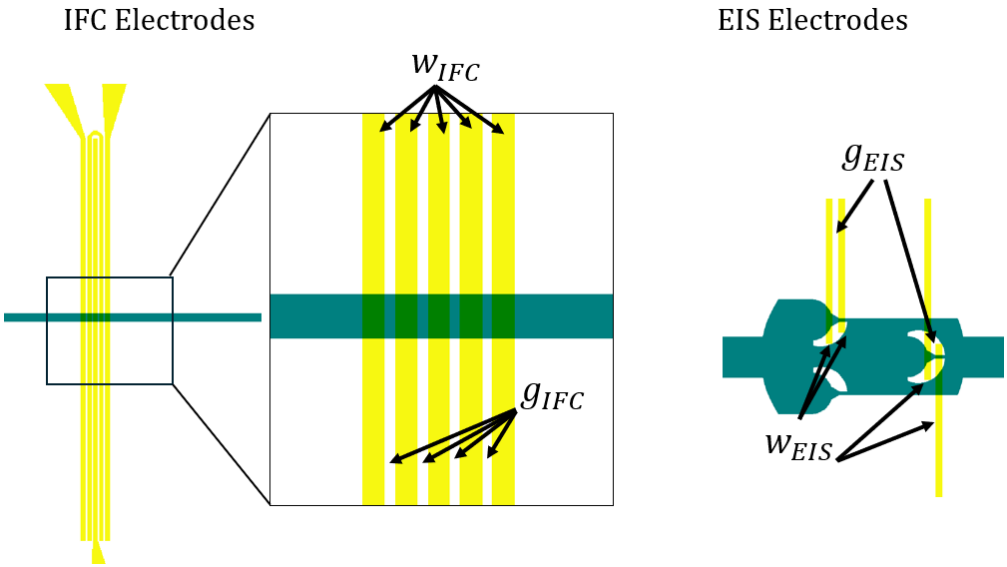

Figure B.9: Sketch of electrodes and channel features contained in chip "T4".

Table B.9: Table of electrodes dimensions for Chip "T4"

Chip "T4"			
w_{IFC}	g_{IFC}	w_{EIS}	g_{EIS}
10 µm	5 µm	3 µm	3 µm

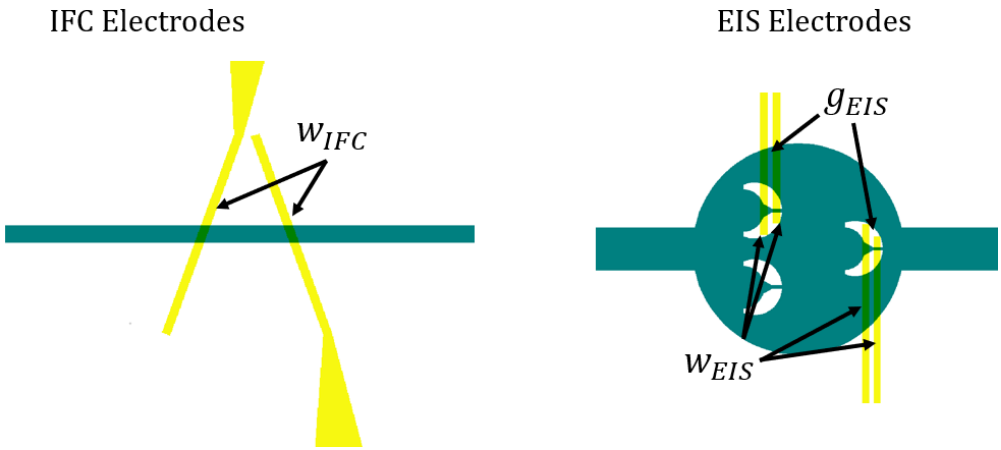

Figure B.10: Sketch of electrodes and channel features contained in chip "T5".

Table B.10: Table of electrodes dimensions for Chip "T5"

Chip "T5"		
w_{IFC}	w_{EIS}	g_{EIS}
10 µm	3 µm	2.5 µm

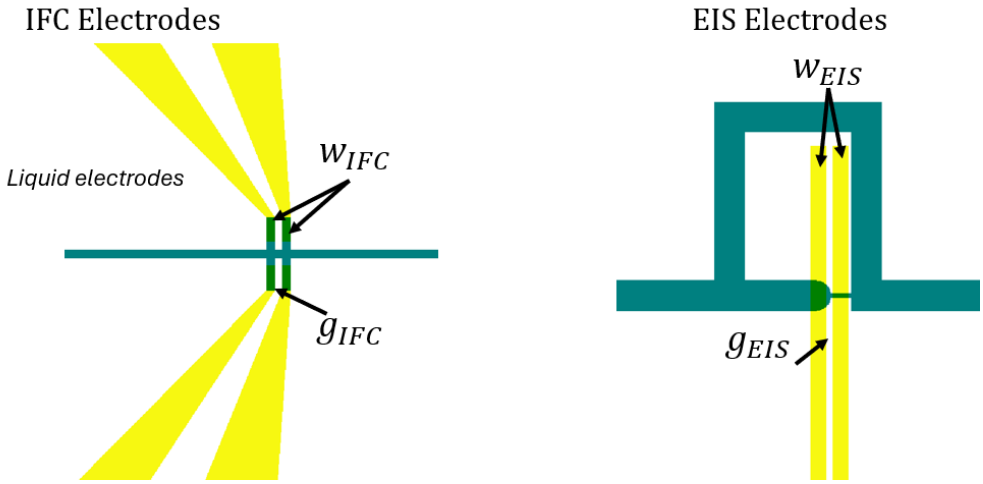

Figure B.11: Sketch of electrodes and channel features contained in chip "T6".

Table B.11: Table of electrodes dimensions for Chip "T6"

Chip "T6"			
w_{IFC}	g_{IFC}	w_{EIS}	g_{EIS}
10 µm	10 µm	5 µm	2.5 µm

Appendix C

Processes and protocols

This appendix includes the protocol used for the preparation of the PDMS at DTU Bioengineering and the fabrication process flow used to fabricate the electrodes and the silicon mold at DTU Nanolab.

C.1 PDMS preparation protocol

- **Mixing**: weigh liquid polymer and curing agent with ratio 10:1 on a scale inside a fume hood. The same disposable plastic container is used for the two components. Stir gently to limit incorporation of air.

- **Pouring**: the obtained mixture is poured onto the Si wafer mold. Place the wafer inside a custom 3D-printed circular holder and pour the mixture on top of it, possibly in the middle of the wafer for best homogeneity. To be performed in a fume hood.

- **Desiccation**: place the circular holder in a desiccator and open vacuum suction. Leave it there until bubbles have significantly reduced (at least 1 hour). Make sure to close vacuum suction when opening the desiccator and perform it under a ventilation tube. Detach the tubing from the desiccator slowly, to avoid sudden change in pressure inside the chamber by letting it vent.

- **Curing**: place the circular holder in an oven at 60 °C for 3 hours. Remove it from the oven and let it cool down before cutting the solidified PDMS with a scalpel.

C.2 Cleanroom process flows

C.2.1 Electrodes process flow

Step	Heading	Equipment	Procedure	Comments
1	**Preparation**			
1.1	Wafer selection	Wafer box	Boron glass - Labmanager: SB616	
2	**Exposure**			
2.1	Photoresist deposition	Spin coater: Gamma UV	AZ 5214E (positive) Thickness=1.5µm	3411 - DCH 100mm 5214E 1,5um HDMS
2.2	UV Exposure	Aligner: Maskless 01	λ=365nm; Dose=110mJ/cm^2; Defocus=0	Design: SDP_maskrunX.cif Mode: Fast
3	**Development**			
3.1	TMAH development	Developer: TMAH UV-lithography	Develop: SP TMAH for 60s	Recipe 1002 DCH 100mm SP60s
4	**Metal dep & Lift-off**			
4.1	Metallization	E-beam evaporator (Temescal)	Ti: 10nm at 2Å/s Au: 150nm at 5Å/s	
4.2	Lift-off	Lift-off	Remover 1165 Δt = 30-55 min at rough 9	After lift-off: 5min in IPA at rough 9 + water rinse + dry
5	**Cut**			
5.1	Cut	DAD 321 Dicing Saw	Cuts in CH1: 4 x 20 mm Cuts in CH2: 4 x 20 mm	Blade height 0.15 mm

Figure C.1: Electrodes fabrication process flow

C.2.2 Mold process flow

Step	Heading	Equipment	Procedure	Comments
1	**Preparation**			
1.1	Wafer selection	Wafer box	Silicon 4" wafers SSP SN629	Orientation<100> Expected thickness: 525 ±20 µm
2	**Exposure**			
2.1	Photoresist deposition	Spin coater: Gamma UV	AZ nLOF 2020 (negative) Thickness=1.5µm	2411 – DCH 100mm nLOF 2020 1.5µm HMDS
2.2	UV Exposure	Aligner: Maskless 01	λ=365nm; Dose=180mJ/cm^2; Defocus=0	Design: SDP_maskrunX.cif Mode: Quality
3	**Development**			
3.1	PEB+TMAH development	Developer: TMAH UV-lithography	Post exp bake 60s @110°C Develop: TMAH for 60s	Recipe 3001 DCH 100mm PEB60s@110C SP60s
4	**Dry etching and resist strip**			
4.1	Dry etching	PEG-1	Process D4 2 min	
4.2	Resist strip	Plasma Asher		
5	**Molecular vapor deposition**			
5.1	FDTS deposition	MVD	Stamp2NP	Multi layer

Figure C.2: Final silicon mold fabrication process flow

Appendix D

Project plan

30 ECTS
start date: 03/03/2025
end date: 03/07/2025
Sara Di Paolo s242164
February 2025

D.1 Introduction and Project description

In this Master's Thesis project will be designed and fabricated a device able to trap and characterize bacteria with a full spectrum impedence scan. The main focus will be put on methods and geometries that will allow to trap a single bacteria.

The idea behind this project arises from the fact that, although research has successfully developed microfluidic traps capable of analyzing bodies such as cells, typically measuring tens of microns in size, it is demonstrably much more challenging to handle significantly smaller bodies with more complex shapes, such as bacteria. The latter tend to evade entrapment even in microscale traps due to intrinsic properties that make them elusive. As a direct consequence, techniques such as impedance flow cytometry (IFC) can capture only a fraction of the impedance spectrum, thereby losing the detailed insights that a full spectral scan could provide if performed on a single immobilized bacteria. This is where our work aims to make its contribution, exploring various possibilities for immobilizing a single bacteria using an hydrodinamic trapping method and performing precise electrical impedance spectroscopy. This approach, when combined with an improved and optimized fixed-frequency impedance flow cytometry analysis, object of a parallel master thesis project of the colleague Sara Pittelli, could provide valuable information about the electrical properties of the bacteria.

Due to the challenges associated with working with bacteria, this thesis has the potential to

yield interesting research findings. In the future, once the techniques are further optimized and expanded, ensuring the reproducibility of experiments and the reliability of results, these studies could be employed to develop innovative Point of Care systems.

D.2 Applied techniques

In order to carry on this project a combination of several activities will be necessary.

- **Finite Element Modelling analysis** performed on COMSOL: this will be crucial to prototype the the trapping system, finding its optimized shape and location on the final device.

- **Lithography mask design** using the software CleWin6.

- **Clean Room fabrication process**: Will include the fabrication of a set of electrodes on a boron glass wafer, with techniques such as lithography and e-beam evaporation, and of a mold that will be used to create the shape of the microfluidic channels from the casting of Polydimethylsiloxane (PDMS), obtained after a new lithography process and a dry etching, performed on a silicon wafer. Here several option will be taken into account to reach the desired resolution, for example employing two-steps lithography or Electron Beam Lithography.

- **Laboratory testing**: The experimental setup for the finished device functionality inspection, including a microscope, a current amplifier, an impedance spectroscope, a syringe pump and a computer, will be assembled in DTU laboratory. The samples will be put in a 3D printed holder designed and fabricated by the colleague Sara Pittelli.

- **Data analysis**: The software Matlab and OriginPro will be used to help with numerical calculations and data fitting.

D.3 Project risks

In this project we'll face different sources of risk, associated with the limitation of the tools and disposable time.

- Some preliminary studies suggest that to effectively trap bacteria the device should reach nanoscale dimension: this is challenging because our current chosen tools struggle in reaching such resolution, if we consider the trade off with the required time and costs. This means that the process flow will be subjected to changes over time and in the worst case will eventually not work with real bacteria.

- The final devices, if the desired dimensions will be reached, will be fragile. The mi-

crofluidic channel creation with PDMS could rise issues during the detaching process, after the polymer solidification. Even in a system with multiple trapping sites, if a single trap is destroyed and the PDMS is pinched, the entire chip will not be suitable to give results.

- The behaviour of the bacteria inside the channel is unpredictable before going to the real experiment: they could be broken by the trap, or start to grow and clog the device.

- COMSOL modelling and simulations take time, therefore it could be necessary a trade of between accuracy of the model and the need to proceed with the fabrication. Final result may not be fully optimized.

- The use of tools is subject to a reservation and availability system, as well as the proper functioning of the machines. This may result in extended working timeframes or the adoption of alternative techniques during the course of the work.

D.4 Time plan

- **Literature study** week 1-2 : Preliminary reading of existing literature work will be useful in order to gather ideas and put some basis for the next steps. This will be focused on the trapping systems dealing with bacteria, cells and particles as well as the bacteria dynamics inside flows.

- **Design** week 3-5 : On COMSOL the shape of the trap will be simulated together with the position of such trap inside the device. Once a first design idea will be decided, on the software Clewin the lithography mask will be produced for the electrodes and the mold for the creation of the PDMS channels.

- **Lab work** week 6-18 : This includes Clean room fabrication process and laboratory final testing. This timeframe will be mostly a trial and error period, so the processes will be iterated as many time as possible to solve issues. It could be necessary to re-design parts.

- **Mid-term discussion**: It will be organized an internal presentation with the research group to discuss the first results approximately in the middle of the semester

- **Writing** week 19-21 : In the final three weeks period the Thesis will be completed. Any incomplete work will be resolved during this time where possible, otherwise the writing work will be prioritized.

- **Supervisor meeting**: every Wednesday (Maria, Christian, Rahul). At least once a month (Winnie).

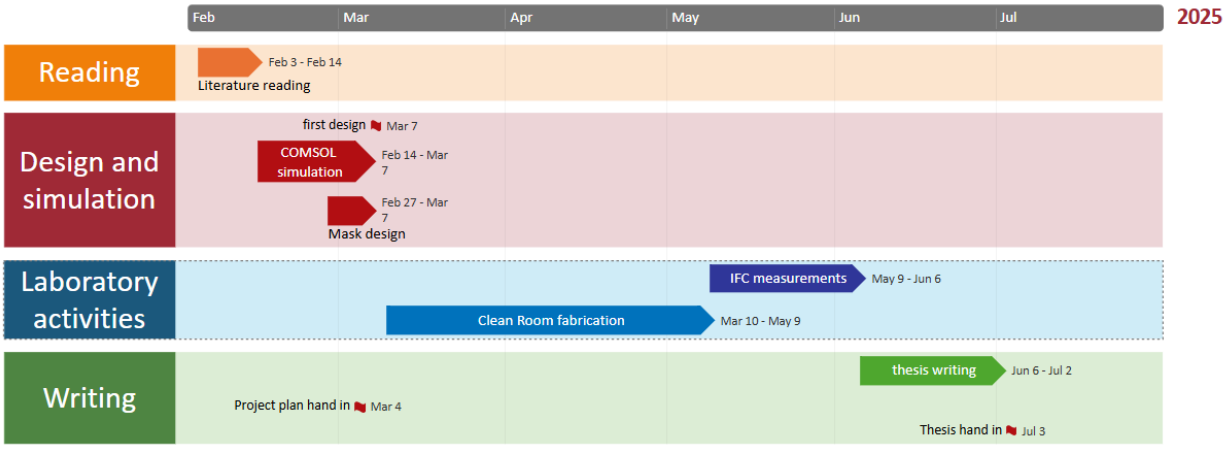

D.5 Final considerations about the project plan

The schedule proposed at the beginning of this project was respected in the first months of the project. However, issues attributed to the improvement of the cleanroom fabrication techniques and the optimization of the experiment procedure led to delays that determined the lack of relevant further analysis.

References

[1] P. Gupta, D. Skiba, and B. Sawicka, "The indispensable role of bacteria in human life and environmental health," *Preprints*, June 2024.

[2] WHO, "Escherichia coli," Feb. 2018, https://www.who.int/news-room/fact-sheets/detail/e-coli.

[3] M. Eryılmaz, E. Yıldırım, and U. Tamer, "Chapter 7 - lab on a chip: A versatile integration with spectroscopic techniques," in *Handbook on Miniaturization in Analytical Chemistry* (C. M. Hussain, ed.), pp. 139–152, Elsevier, 2020.

[4] J. Bahnemann and A. Grünberger, eds., *Microfluidics in Biotechnology*, vol. 179 of *Advances in Biochemical Engineering/Biotechnology*. Cham: Springer International Publishing, 2022.

[5] C. Karen, M. Di Berardino, G. Schade, M. Hebeisen, A. Pierzchalski, J. Bocsi, A. Mittag, and A. Tárnok, "Microfluidic impedance-based flow cytometry," *Cytometry. Part A : the journal of the International Society for Analytical Cytology*, vol. 77, pp. 648–66, 07 2010.

[6] C. H. Clausen, M. Dimaki, C. V. Bertelsen, G. E. Skands, R. Rodriguez-Trujillo, J. D. Thomsen, and W. E. Svendsen, "Bacteria detection and differentiation using impedance flow cytometry," *Sensors*, vol. 18, no. 10, 2018.

[7] "Basic Biology of Oral Microbes," in *Atlas of Oral Microbiology*, pp. 1–14, Elsevier, 2015.

[8] J. W. Costerton, J. M. Ingram, and K. J. Cheng, "Structure and function of the cell envelope of gram-negative bacteria," *Bacteriological Reviews*, vol. 38, pp. 87–110, Mar. 1974.

[9] Y. Feng, L. Huang, P. Zhao, F. Liang, and W. Wang, "A microfluidic device integrating impedance flow cytometry and electric impedance spectroscopy for high-efficiency single-

cell electrical property measurement," *Analytical Chemistry*, vol. 91, no. 23, pp. 15204–15212, 2019. PMID: 31702127.

[10] C. V. Bertelsen, G. E. Skands, M. González Díaz, M. Dimaki, and W. E. Svendsen, "Using Impedance Flow Cytometry for Rapid Viability Classification of Heat-Treated Bacteria," *ACS Omega*, vol. 8, pp. 7714–7721, Feb. 2023.

[11] D. C. Spencer, T. F. Paton, K. T. Mulroney, T. J. J. Inglis, J. M. Sutton, and H. Morgan, "A fast impedance-based antimicrobial susceptibility test," *Nature Communications*, vol. 11, p. 5328, Oct. 2020.

[12] L. Yang, "Electrical impedance spectroscopy for detection of bacterial cells in suspensions using interdigitated microelectrodes," *Talanta*, vol. 74, pp. 1621–1629, Feb. 2008.

[13] M.-C. Kim, B. C. Isenberg, J. Sutin, A. Meller, J. Y. Wong, and C. M. Klapperich, "Programmed trapping of individual bacteria using micrometre-size sieves," *Lab on a Chip*, vol. 11, no. 6, p. 1089, 2011.

[14] D. Kwon, J. Kim, S. Chung, and I. Park, "A nanowire-integrated microfluidic device for hydrodynamic trapping and anchoring of bacterial cells," in *2014 IEEE 27th International Conference on Micro Electro Mechanical Systems (MEMS)*, (San Francisco, CA, USA), pp. 246–249, IEEE, Jan. 2014.

[15] K. Asami, "Characterization of heterogeneous systems by dielectric spectroscopy," *Progress in Polymer Science*, vol. 27, no. 8, pp. 1617–1659, 2002.

[16] K. Asami, T. Yonezawa, H. Wakamatsu, and N. Koyanagi, "Dielectric spectroscopy of biological cells," *Bioelectrochemistry and Bioenergetics*, vol. 40, no. 2, pp. 141–145, 1996.

[17] G. Schade-Kampmann, A. Huwiler, M. Hebeisen, T. Hessler, and M. Di Berardino, "On-chip non-invasive and label-free cell discrimination by impedance spectroscopy," *Cell Proliferation*, vol. 41, no. 5, pp. 830–840, 2008.

[18] C. Honrado, P. Bisegna, N. S. Swami, and F. Caselli, "Single-cell microfluidic impedance cytometry: from raw signals to cell phenotypes using data analytics," *Lab on a Chip*, vol. 21, no. 1, pp. 22–54, 2021.

[19] F. Caselli, A. de ninno, R. Reale, L. Businaro, and P. Bisegna, "A novel wiring scheme for standard chips enabling high-accuracy impedance cytometry," *Sensors and Actuators B Chemical*, vol. 256, 10 2017.

[20] C. H. Clausen, G. E. Skands, C. V. Bertelsen, and W. E. Svendsen, "Coplanar electrode layout optimized for increased sensitivity for electrical impedance spectroscopy," *Micromachines*, vol. 6, no. 1, pp. 110–120, 2015.

[21] D. S. De Bruijn, K. F. Jorissen, W. Olthuis, and A. Van Den Berg, "Particle Size Determination in Impedance Flow Cytometry Using Measured Opacity," in *2021 21st International Conference on Solid-State Sensors, Actuators and Microsystems (Transducers)*, (Orlando, FL, USA), pp. 1036–1039, IEEE, June 2021.

[22] A. D. Shaw, M. K. Winson, A. M. Woodward, A. C. McGovern, H. M. Davey, N. Kaderbhai, D. Broadhurst, R. J. Gilbert, J. Taylor, E. M. Timmins, R. Goodacre, D. B. Kell, B. K. Alsberg, and J. J. Rowland, "Rapid Analysis of High-Dimensional Bioprocesses Using Multivariate Spectroscopies and Advanced Chemometrics," in *Bioanalysis and Biosensors for Bioprocess Monitoring*, vol. 66, pp. 83–113, Berlin, Heidelberg: Springer Berlin Heidelberg, 1999. Series Title: Advances in Biochemical Engineering/Biotechnology.

[23] T. Tang, X. Liu, Y. Yuan, T. Zhang, R. Kiya, Y. Yang, K. Suzuki, Y. Tanaka, M. Li, Y. Hosokawa, and Y. Yalikun, "Assessment of the electrical penetration of cell membranes using four-frequency impedance cytometry," *Microsystems & Nanoengineering*, vol. 8, p. 68, June 2022.

[24] H. Morgan, T. Sun, D. Holmes, S. Gawad, and N. G. Green, "Single cell dielectric spectroscopy," *Journal of Physics D: Applied Physics*, vol. 40, pp. 61–70, Jan. 2007.

[25] T. Sun and H. Morgan, "Single-cell microfluidic impedance cytometry: a review," *Microfluidics and Nanofluidics*, vol. 8, pp. 423–443, Apr. 2010.

[26] O. G. Martinsen and A. Heiskanen, "Electrodes," in *Bioimpedance and Bioelectricity Basics*, pp. 175–248, Elsevier, 2023.

[27] U. of Cambridge Department of Chemical Engineering and Biotecnology, "Electrical double layer," https://www.ceb.cam.ac.uk/research/groups/rg-eme/Edu/the-electrical-double-layer.

[28] K. Aoki, Y. Hou, J. Chen, and T. Nishiumi, "Resistance associated with measurements of capacitance in electric double layers," *Journal of Electroanalytical Chemistry*, vol. 689, pp. 124–129, Jan. 2013.

[29] D. Borkholder, "Cell based biosensors using microelectrodes," Jan. 1998.

[30] C. Bertelsen, "Using impedance spectroscopy for antibiotic susceptibility testing," Mar. 2014.

[31] F. Gökçe, P. S. Ravaynia, M. M. Modena, and A. Hierlemann, "What is the future of electrical impedance spectroscopy in flow cytometry?," *Biomicrofluidics*, vol. 15, p. 061302, Dec. 2021.

[32] J. Kirkegaard, C. H. Clausen, R. Rodriguez-Trujillo, and W. E. Svendsen, "Study of paclitaxel-treated hela cells by differential electrical impedance flow cytometry," *Biosensors*, vol. 4, no. 3, pp. 257–272, 2014.

[33] D. Holmes, D. Pettigrew, C. H. Reccius, J. D. Gwyer, C. van Berkel, J. Holloway, D. E. Davies, and H. Morgan, "Leukocyte analysis and differentiation using high speed microfluidic single cell impedance cytometry," *Lab on a Chip*, vol. 9, no. 20, pp. 2881–2889, 2009.

[34] Britannica, "Reynold's Number," https://www.britannica.com/science/Reynolds-number.

[35] D. Di Carlo, D. Irimia, R. G. Tompkins, and M. Toner, "Continuous inertial focusing, ordering, and separation of particles in microchannels," *Proceedings of the National Academy of Sciences*, vol. 104, no. 48, pp. 18892–18897, 2007.

[36] N. Rousset, C. Lohasz, J. Boos, P. Misun, F. Cardes, and A. Hierlemann, "Circuit-based design of microfluidic drop networks," *Micromachines*, vol. 13, p. 1124, 07 2022.

[37] H. Bruus, *Theoretical microfluidics*, vol. 18. Oxford University Press, 2007.

[38] R. M. Johann, "Cell trapping in microfluidic chips," *Analytical and Bioanalytical Chemistry*, vol. 385, pp. 408–412, June 2006.

[39] V. Narayanamurthy, S. Nagarajan, A. Y. Firus Khan, F. Samsuri, and T. M. Sridhar, "Microfluidic hydrodynamic trapping for single cell analysis: mechanisms, methods and applications," *Analytical Methods*, vol. 9, no. 25, pp. 3751–3772, 2017.

[40] J. Katuri, W. E. Uspal, J. Simmchen, A. Miguel-López, and S. Sánchez, "Cross-stream migration of active particles," *Science Advances*, vol. 4, no. 1, p. eaao1755, 2018.

[41] R. Burger and J. Ducrée, "Handling and analysis of cells and bioparticles on centrifugal microfluidic platforms," *Expert Review of Molecular Diagnostics*, vol. 12, pp. 407–421, May 2012.

[42] J. R. Rettig and A. Folch, "Large-scale single-cell trapping and imaging using microwell arrays," *Analytical Chemistry*, vol. 77, no. 17, pp. 5628–5634, 2005. PMID: 16131075.

[43] T. Arakawa, M. Noguchi, K. Sumitomo, Y. Yamaguchi, and S. Shoji, "High-throughput single-cell manipulation system for a large number of target cells," *Biomicrofluidics*, vol. 5, no. 1, 2011.

[44] J. R. Rettig and A. Folch, "Large-scale single-cell trapping and imaging using microwell arrays," *Analytical chemistry*, vol. 77, no. 17, pp. 5628–5634, 2005.

[45] M. Tanyeri, M. Ranka, N. Sittipolkul, and C. M. Schroeder, "A microfluidic-based hydrodynamic trap: design and implementation," *Lab on a Chip*, vol. 11, no. 10, pp. 1786–1794, 2011.

[46] B. R. Lutz, J. Chen, and D. T. Schwartz, "Hydrodynamic tweezers: 1. noncontact trapping of single cells using steady streaming microeddies," *Analytical chemistry*, vol. 78, no. 15, pp. 5429–5435, 2006.

[47] I. M. Handrea-Dragan, I. Botiz, A.-S. Tatar, and S. Boca, "Patterning at the micro/nano-scale: Polymeric scaffolds for medical diagnostic and cell-surface interaction applications," *Colloids and Surfaces B: Biointerfaces*, vol. 218, p. 112730, Oct. 2022.

[48] F. Roozeboom, F. Bruele, Y. Creyghton, P. Poodt, and W. Kessels, "Cyclic etch/passivation-deposition as an all-spatial concept toward high-rate room temperature atomic layer etching," *ECS Journal of Solid State Science and Technology*, vol. 4, pp. N5067–N5076, 04 2015.

[49] Y. R. Herrero, K. L. Camas, and A. Ullah, "Chapter 4 - characterization of biobased materials," in *Advanced Applications of Biobased Materials* (S. Ahmed and Annu, eds.), pp. 111–143, Elsevier, 2023.

[50] K. Xiao, Y. Xu, X. Cao, H. Xu, and Y. Li, "Chapter 18 - advanced characterization of membrane surface fouling," in *60 Years of the Loeb-Sourirajan Membrane* (H.-H. Tseng, W. J. Lau, M. A. Al-Ghouti, and L. An, eds.), pp. 499–532, Elsevier, 2022.

[51] I. Miranda, A. Souza, P. Sousa, J. Ribeiro, E. M. S. Castanheira, R. Lima, and G. Minas, "Properties and Applications of PDMS for Biomedical Engineering: A Review," *Journal of Functional Biomaterials*, vol. 13, p. 2, Dec. 2021.

[52] C. V. Bertelsen, "Screening of Bacteria using Impedance Flow Cytometry," May 2021.

[53] A. Rosenthal and J. Voldman, "Dielectrophoretic traps for single-particle patterning," *Biophysical Journal*, vol. 88, no. 3, pp. 2193–2205, 2005.